NANODIAMOND-SUPPORTED COMPOSITE MATERIALS FOR CATALYSIS

by

Arthur Daniel Quast

A dissertation submitted to the faculty of
The University of Utah
in partial fulfillment of the requirements for the degree of

Doctor of Philosophy

Department of Chemistry

The University of Utah

August 2017

The University of Utah Graduate School

STATEMENT OF DISSERTATION APPROVAL

The dissertation of **Arthur Daniel Quast**

has been approved by the following supervisory committee members:

Jennifer S. Shumaker-Parry	, Chair	**June 1, 2017** Date Approved
Ilya Zharov	, Member	**June 1, 2017** Date Approved
John C. Conboy	, Member	**June 1, 2017** Date Approved
Janis Louie	, Member	**June 1, 2017** Date Approved
Sivaraman Guruswamy	, Member	**June 1, 2017** Date Approved

and by **Cynthia J. Burrows**, Chair/Dean of

the Department/College/School of **Chemistry**

and by David B. Kieda, Dean of The Graduate School.

ABSTRACT

Nanomaterials are the focus of intense research efforts in a variety of fields because of dramatic differences in properties when compared to the corresponding bulk materials. Catalysis is one material property that can become more pronounced at the nanoscale. By lowering energy requirements for chemical reactions, catalysts reduce production costs in diverse sectors of the economy, including medicine, transportation, environmental protection, oil and gas, food, and synthetic materials. Transition metals are an important class of catalysts capable of facilitating reduction and oxidation of molecular species. Since the discovery of transition metal catalysts nearly 200 years ago, certain metals were considered more active as catalysts (i.e., Pt, Pd, and Ru), while others (Au) appeared to have negligible catalytic activity as bulk materials. In recent years, gold nanoparticles (AuNPs) have become a fast-growing field of research owing to their unexpected catalytic properties not present in the bulk material. However, unsupported AuNPs are highly prone to flocculation and subsequent reduced catalytic activity. The choice of an appropriate aggregation-resistant stabilizing ligand for these nanoparticles is an important part of maintaining nanoscale catalytic properties. Additional stability is provided by anchoring AuNPs to support materials, allowing for dramatic improvements in catalyst lifetimes. This work discusses the development of novel diamond support materials for improving the stability of catalytically active AuNPs. Synthetic nanodiamond is a widely available, inexpensive, and robust material that has found

applications in a wide range of commercial abrasives, lubricants, and composite materials. By exploiting the rich surface chemistry of nanodiamond, we have developed versatile catalyst support materials that offer unrivaled chemical and mechanical stability. Various nanodiamond surface modifications are readily prepared using a combination of chemical vapor deposition, photo-active polymer chemistry, and synthetic organic chemistry techniques. Control over the surface chemistry and properties of the resulting nanodiamond allow for increased stability of AuNPs via surface anchored thiol and amine moieties. The use of diamond as a support material should allow a wide variety of noble and nonprecious metal composite materials to be used as catalysts in harsh chemical environments not suitable for existing support materials.

TABLE OF CONTENTS

LIST OF FIGURES

Figures

LIST OF TABLES

Tables

ACKNOWLEDGEMENTS

I am grateful for the help and support that my advisor, Dr. Jennifer Shumaker-Parry, has provided throughout the past several years. The freedom I was given to pursue research that interested me was the catalyst for the success I experienced. Her leadership has often given me the chance to pause and consider what type of mentor/leader I would like to be in my professional career. I hope that I am able to foster a similar environment of independence and collaboration with my colleagues and future groups.

I would also like to thank the many friends and colleagues within the Department of Chemistry and across campus who have been available to help with research and classes, as well as simply being good friends.

I wish my mother could have seen me graduate, and despite her passing during my first semester of this program, I feel that the best parts of who I am today are because of her. I miss her and hope that my pursuit of this degree is something that would make her proud. I'm grateful for the love and support of Ted, Linnea, and Paul throughout my life; at one time or another, each has offered and given help whenever it was needed. I'm lucky to have been born into such a wonderful family.

Above all, I want to thank my wife, Stacie, for her unwavering support and commitment to me and our family. Her love and encouragement have not only helped me through some of the most difficult times in my life, they have also been the source of the greatest happiness I have enjoyed. Her example to me and our daughter, Annie, has been

a constant source of strength and peace. Pursuing a PhD while juggling being a husband and father has added a depth and richness that would have been impossible without such a loving family.

CHAPTER 1

INTRODUCTION

1.1 Catalysis

Catalysts are materials that participate in chemical reactions by reducing the activation energy while not being consumed in the reaction. The reduction in activation energy is made possible by offering an alternative and more efficient reaction pathway.[1] Figure 1.1 illustrates this principle for a given hypothetical reaction scheme where the potential energy of catalyzed and uncatalyzed reaction pathways is plotted as a function of the reaction progress. For catalytic processes, ΔG remains constant, and as Equation 1.1 shows, the equilibrium constant, K_{eq}, also remains unchanged,

$$\Delta G = -RT \ln K_{eq} \tag{1.1}$$

where ΔG is the change in reaction free energy, R is the gas constant, and T is the temperature. However, even though K_{eq} is unchanged for a catalyzed process, the activation energy is lowered and the reaction rate, the rate of conversion from reactants to products, can increase by several orders of magnitude when aided by a suitable catalyst.

1.2 Heterogeneous Catalysis

There are generally two types of catalysts: homogeneous and heterogeneous. As the name suggests, homogeneous catalysts are those materials that are used under

conditions in which the reactants are in the same phase as the catalyst. Heterogeneous catalysts are by definition materials present in a different phase than the reactants. Successful reaction pathways are dependent on proper molecular orientation in order for reaction intermediates, transition states, and eventually products to be formed. Molecular orientation is therefore essential to the chemical function of both homogeneous and heterogeneous catalysts.

Heterogeneous catalysis depends on species adsorption at specific surface locations known as active sites. While some reactions require only adsorption to any surface site (i.e., structure-insensitive reaction), a large number of catalytic reactions are more favored by specific types of surface sites with particular atomic arrangements (i.e., structure-sensitive reaction).[2-3] Much like mechanisms for enzymes in biological systems, the reactive species must not only adsorb to the catalyst at an active site, but it must also adsorb in the correct orientation for catalysis to occur. Some catalysts, like zeolites, are readily produced with ordered structures, resulting in a high number of well-defined active sites. Other heterogeneous catalysts, like metallic nanoparticles, are more prone to a high degree of surface inhomogeneity, with much less control of the final structures, including the type and distribution of specific active sites.[4-5] One way to overcome this challenge is to simply produce heterogeneous catalysts with high surface areas to increase the population of active sites, thereby increasing the probability that reactants will adsorb at those sites.

The structural requirements inherent in heterogeneous catalysts result in a high degree of dependence on catalyst physical features such as surface area, morphology, and active site access. Transition metal nanoparticles exhibit catalytic activity with a high

dependence on structure. The specific surface area for these nanoparticle materials can be several hundred m^2/g. This high surface area is important because it increases the ratio of reactant to active site access. Somorjai and others have pointed out that these active sites occur at special surface features known as defect sites.[6-9] Figure 1.2 illustrates these surface defect sites as interruptions to a flat, close-packed surface of metal atoms. These sites can be locations where single atoms are added (adatoms) or missing (vacancies), or edges in planes of atoms in an otherwise uniform surface. These defect sites are regions of relatively high surface energies because there are fewer stabilizing coordination atoms than neighbor surface atoms compared to atoms in a bulk material or even at the core of a nanoparticle. For metal nanoparticles, the number of these defect sites increases as the specific surface area increases.

1.3 Mechanisms: Langmuir-Hinshelwood vs. Eley-Rideal

For heterogeneous catalysts at surfaces, there are two generally accepted processes for reaction mechanisms: Langmuir-Hinshelwood (LH) and Eley-Rideal (ER). As illustrated in Figure 1.3, when a reaction is classified as LH, this means that both reactant species must first adsorb onto the surface of the catalyst, followed by surface diffusion and then reaction to produce product. An ER mechanism is characterized by adsorption of only one reactant species, followed by generation of product once the second reactant diffuses to the site of the adsorbed reactant. Inherent to these two mechanistic models is the idea that catalyst surfaces contribute to product formation in a way that is specific to the adsorbate–surface material interaction; for catalysts, this contribution is the enablement of electron movement. Understanding how certain catalysts facilitate the movement of electrons in reactant molecules when adsorbed to

catalytically active surface sites is essential to improving the efficiency of chemical reactions. Model catalytic reactions allow studies of the various parameters important to catalysis by monitoring the efficiency with which products are generated from substrate molecules at active sites. One of these model catalytic reactions that follows an LH mechanism at catalyst surfaces is the reduction of nitroarenes.

1.4 Catalytic Reduction of Nitroarenes

Nitroarenes are an important class of compounds because of their industrial utility and environmental toxicity.[10] In particular, one nitroarene, 4-nitrophenol, has become the molecule of choice for investigating catalytic activity for noble metal nanoparticles using UV-Vis monitoring.[11-12] The reduction of 4-NP to 4-aminophenol (4-AP) can be carried out with a strong reducing agent like $LiAlH_4$; however, a weaker reducing agent such as $NaBH_4$ is not strong enough to reduce the nitro group to an amine. When a suitable catalyst is added to an aqueous mixture of 4-NP and $NaBH_4$, the reduction to 4-AP readily occurs. The change in color from a bright yellow solution to a colorless one makes this reaction easily observable for kinetic studies. By monitoring the characteristic absorbance of 4-NP at 400 nm with UV-Vis spectrophotometry, the activity of various catalysts can be determined.

The reduction of 4-NP proceeds through a multistep mechanism that occurs only after both BH_4^- (the source of H_2) and 4-NP have adsorbed onto the surface of the catalyst.[13] Initially, 4-NP is deprotonated to yield the species 4-nitrophenolate, because under aqueous conditions at neutral pH, the reducing agent $NaBH_4$ is unstable, leading to its spontaneous decomposition and production of a basic environment.[14] The rapid decomposition of $NaBH_4$, as shown in Equations 1.2 and 1.3, can be prevented by

running

$$NaBH_4 + 2H_2O \rightarrow NaBO_2 + 4H_2 \quad (1.2)$$

$$NaBO_2 + H_2O \rightarrow NaOH + H_3BO_3 \quad (1.3)$$

the reaction in 1M NaOH.[15] Nevertheless, the presence of basic conditions always leads to the formation of 4-nitrophenolate, as shown in the first step of Figure 1.4. The reduction of 4-nitrophenolate to 4-nitrosophenolate and subsequent reduction to 4-hydroxylaminophenolate (4-HP) are both rapid, as 4-HP is a stable intermediate species. The rate-determining step is the final reduction from the stable intermediate 4-HP to 4-aminophenolate. Because this reaction is governed by the LH mechanism, all species must be adsorbed to the surface of the catalytically active sites for 4-AP to be formed and, as a result, the adsorption/desorption equilibrium for all species plays a critical role in the final reaction rate. Therefore, any changes to the surface environment around these active sites should have a dramatic effect on reaction kinetics.

The kinetic analysis of the reduction of 4-NP to 4-AP is often simplified by using a large excess of $NaBH_4$, so that the rate can be approximated as pseudo-first order with respect to 4-NP.[13] Menumerov and coworkers discovered that reaction conditions rarely controlled by others in the literature are extremely important.[12] Dissolved oxygen content, temperature, and relative reagent concentrations are all critical to proper kinetic analysis; however, many researchers are content to ignore these complications in the interest of a general comparison, using turnover frequencies (TOF; defined as the number of molecules of 4-AP produced divided by the number of catalytically active surface sites per unit of time).

1.5 Unusual Catalytic Activity of Gold Nanoparticles

Transition metals are unique elements for chemical catalysis because they readily facilitate the transfer of electrons. Many reactions require the oxidation or reduction of molecules as a part of the transformation of reactants to products. Elements in the d-block are able to accept or donate electrons located in the valence shell because d-band mixing with s and p electrons results in a high density of low-energy and vacant electronic states that readily allow electrons to exchange with adsorbed molecules.[6] Clusters of transition metal atoms promote electron transfer by temporarily spreading deficient or excess charge over many atoms, effectively serving as "electron reservoirs" during red-ox reactions.[16] As bulk materials, many d-block elements such as Ni, Pd, and Pt are potent catalysts, yet most early work with Au indicated negligible catalytic activity.[17]

As a bulk material, gold is generally considered to be chemically inert; however, when the size is reduced to the nanoscale. this metal starts to display unusual properties. Color, melting point, and catalytic activity are among several properties that change dramatically when gold is reduced to nanometer size ranges.[17] Gold clusters of tens of millions of atoms exhibit a red color owing to plasmonic effects from electron confinement when electromagnetic radiation interacts with the clusters. When the size is reduced even further to the single digit nanometer scale, the clusters no longer support plasmonic effects while becoming unusually active catalysts.[18]

The catalytic properties of gold nanoclusters were first recognized only in the 1980s by Haruta and others.[19] This surprising discovery has led to an explosion of research into potential reactions catalyzed by AuNPs.[17, 20] The large difference in efficiency between bulk Au and nanoscale Au catalytic activity is related to the ratio of

surface atoms accessible to reactant molecules and interior bulk atoms unavailable for direct interaction in heterogeneous catalysis. Catalysts such as AuNPs are an example of a structure-sensitive catalyst exhibiting negligible catalytic activity as a bulk material because the surface remains effectively inactive until nanoscale structural defects dominate.[2, 5, 21-24]

As shown in Figure 1.5, with cluster diameters of 2–5 nm, AuNPs are composed of several thousand atoms, and the ratio of surface atoms to total atoms in NPs begins to be appreciable.[22, 25-26] The ratio of surface atoms to total atoms in a metal cluster is the metal size dispersion,

$$D_M = \frac{6 n_s M_w}{\rho N d_p} \tag{1.4}$$

where n_s is equal to the number of metal atoms on the particle surface per unit area, M_w is the molecular weight of the metal, ρ is the bulk metal density, N is Avagadro's number, and d_p is the diameter of the metal clusters as determined by TEM.[22, 25] This size-related factor takes into account the fact that as the NP diameter decreases, the effective total surface area increases, leading to a greater number of defect sites important to catalysis. Exploration of the catalytic activity of these active sites is crucial to developing next-generation catalysts. At these higher dispersion values, the activity of AuNPs as heterogeneous catalysts is significant owing to the increase in the number of sufficiently energetic surface atoms at defect sites, edges, and corners. Heterogeneous catalysis of small molecules at AuNPs is especially favored for molecules that can reversibly adsorb at these defect sites.[27-28]

1.6 Supported vs. Unsupported Gold Nanoparticle Catalysts

Clearly the accessibility of active surface sites is critical to AuNP catalysis; however, the high catalytic activity of colloidal AuNPs is short-lived due to a tendency toward aggregation.[29] High-energy surface sites are conducive to catalysis but high-energy-states surfaces are also thermodynamically unstable. Although surface ligands can help improve colloid stability, the use of highly stabilizing ligands might also have the effect of reducing reactant molecule access to surface sites.

One approach commonly employed to stabilize AuNPs for catalysis and simultaneously hinder aggregation is to attach NPs to solid support materials.[30] Numerous materials have been used to support AuNPs with and without adhesion-promoting layers. Many studies of supported AuNP systems as catalysts for the reduction of 4-NP rely on silica spheres or silica films with silanes as adhesion promoters.[31-36] The silica/silane system is advantageous because silica is easily prepared as spheres, using the Stöber method, or as a coating, and there are a wide variety of commercially available silanes with chemical moieties conducive to metal NP attachment.[35, 37-38]

The abundance of literature precedent for using the silica/silane system for AuNP catalysts is a compelling reason for future use of this system in research; however, the 4-NP reduction reaction using $NaBH_4$ creates a basic reaction environment that is detrimental to silica/silane-based interfaces. Unfortunately, despite the obvious need for catalyst stability, the condition of the silica/silane support materials postreaction is an often overlooked problem in current studies. When this stability issue is investigated, the problems become readily apparent.[39] Silica/silane materials are unstable in even mildly basic or acidic conditions, and great care must be taken to avoid these environments. This

instability would seem to indicate that a different, more robust system would be advantageous, especially for the $NaBH_4$ reduction of nitrophenols.

Ideally, further development of support materials used to anchor catalytically active AuNPs would be targeted toward materials that are resistant to acids, bases, elevated temperatures, and polar/nonpolar solvents, while also maintaining catalyst–support material adhesion and stability. Polymers, graphene oxide, as well as some metal oxides (TiO_2, MgO, Al_2O_3, zirconia, and CeO_2), may be suitable for some of these conditions, but surface modification of these materials presents challenges due to limited surface chemistries.[20, 40-43] Apart from adhesion and surface stability, there is evidence of synergistic catalyst–support material interactions, increasing the overall catalytic activity of otherwise unsupported catalysts.[2, 21, 23-24] However, some catalysts, such as AuNPs, may benefit dramatically from increased surface stability afforded by surfaces tailored toward both adhesion and favorable chemical environments. Synthetic diamond has already shown promise as a highly modifiable interface while simultaneously displaying excellent chemical and mechanical stability.

1.7 Diamond Nanoparticles as Catalyst Support Materials

Since its first development in the 1950s by scientists at General Electric, synthetic diamond created using the belt or high pressure high temperature (HPHT) method has played a major role in the abrasives, additives, coatings, and jewelry industries.[44-46] Besides HPHT diamond, other types of synthetic diamond are commercially available in several forms, including natural, chemical vapor deposition (CVD), and detonation (DND). Natural diamond is often of variable purity and expensive due to the cost of earth mining and some artificial market pressures. CVD diamond is currently used to produce

films or low-surface-area materials, limiting its use as a catalyst support. DND might be an ideal support material because of high surface areas (200–400 m^2/g) with primary particle sizes that are 5 nm; however, such small sizes make it more difficult to recollect and purify.[47] HPHT diamond is produced in large quantities, making it inexpensive and readily available. Conveniently, the high density of diamond (~3.5 g/cm^3) combined with the larger HPHT particle sizes (typically ranging from tens of nm to several mm) makes recollection in solutions simple compared to DND. HPHT diamond's primary use as a consumable abrasive material allows it to be widely available with material costs similar to commercially produced silica particles.

The chemical equivalency of HPHT diamond to CVD and DND also means that surface functionalization methods are well established. Much of the work with diamond materials in the past 30 years has been carried out using CVD and DND. The differences between HPHT and CVD or DND primarily lie in impurities and, as a result, HPHT diamond surfaces are readily functionalized through similar procedures. Researchers have developed methods for functionalizing diamond surfaces with a wide variety of chemical groups: hydrogen termination, alkyls, hydroxyls, carboxyls, amines, amides, thiols, fluorides, chlorides, and many others. The rich literature precedent for diamond functionalization is a convenient starting point for creating a suitable substrate with excellent chemical stability while still allowing for robust adhesion of transition metal nanoparticle catalysts such as AuNPs. In fact, the combination of surface functionalized diamond and catalytically active surface species is a nearly unexplored area of surface chemistry.

1.8 Dissertation Outline

The materials discussed here were fabricated with the intent of better understanding what role diamond-based support materials play in facilitating the catalytic activity of transition metal NPs. The final goal is to produce stable platforms for AuNP catalysts embedded in polymer brush environments. Future studies will investigate modulation of the chemical environment surrounding the diamond-supported AuNP catalysts and the impact on catalysis.

1.8.1 Exploiting Intrinsic Impurities of HPHT Diamond for Catalysis

The diamond chosen for this work was confined to HPHT material. An understanding of the synthetic method used to produce HPHT diamond revealed that these materials might include metal impurities leftover from production. A foundational study of the role that these metal impurities might play in 4-NP reduction was deemed necessary in order to differentiate catalysis by attached AuNPs vs. that of the trace metal impurities. As a result of these experiments, we now understand that trace amounts of Fe, Ni, Co, and other unidentified metals do catalyze the reduction of 4-NP by $NaBH_4$.

1.8.2 Direct Modification of Nanodiamond Powders

The uses and applications for modified diamond surfaces are an underdeveloped area of research, while literature on diamond surface functionalization is plentiful. Instead of isolated observations noting the successful uses of surface modifications, reactions were linked in a step-wise fashion to yield procedures that can be used to prepare aminated HPHT diamond surfaces with subsequent attachment of polymer brush coatings. The expectation is that these materials will be the foundation of future efforts

toward embedding catalytically active metal NPs in diverse polymer brush environments in order to study the role that local environments play in facilitating catalysis.

1.8.3 Thiol-Ene Polymer-Coated Nanodiamond-Supported NP Catalysts

Direct attachment of thiol-ene polymer films to ND supports is shown to be possible using UV-initiated radical polymerization facilitated by the incorporation of noble metal salts. The polymer/ND composites can be readily decorated with catalytically active noble metal NPs. The activity of these catalysts can be evaluated using the reduction of 4-NP by $NaBH_4$. The enhanced stability of these composites is compared to other supported catalyst materials and shown to be a robust alternative to existing systems.

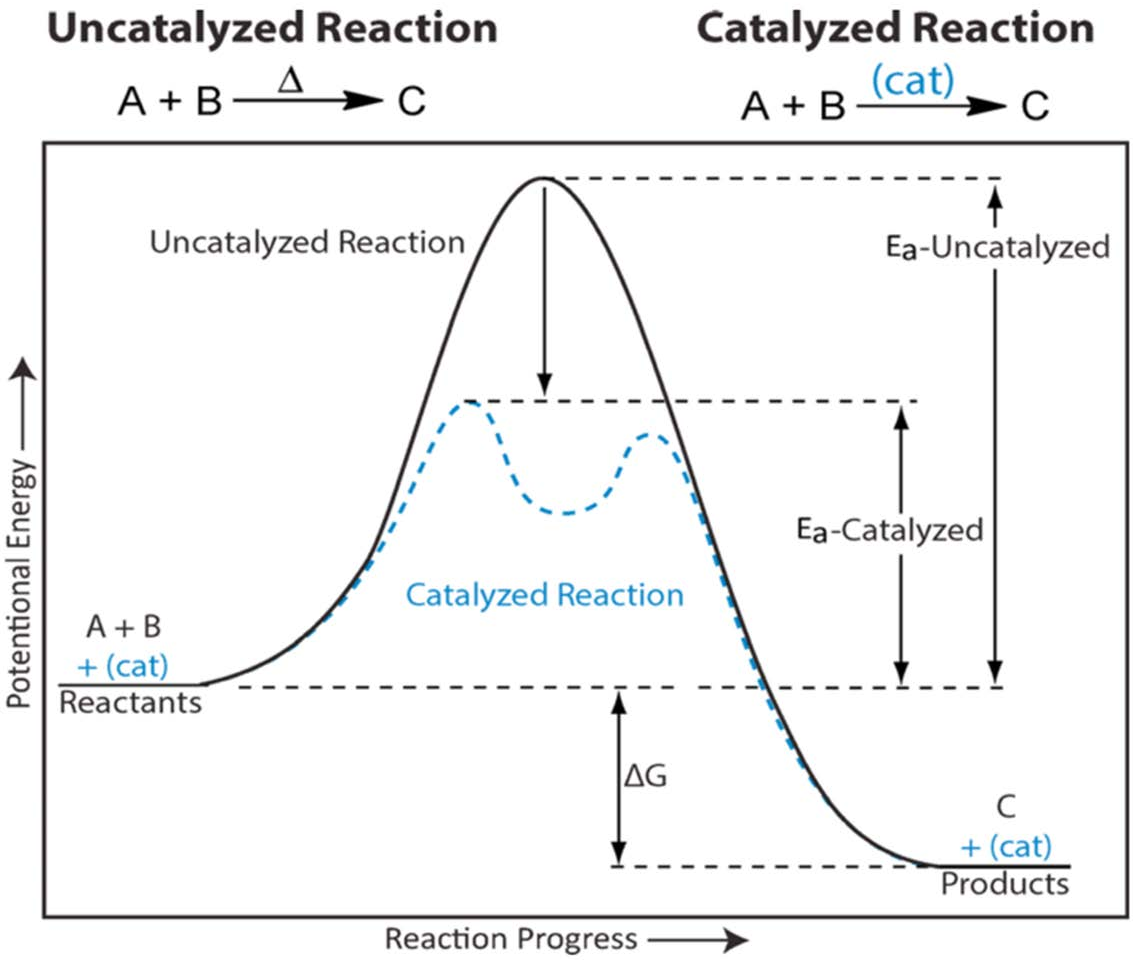

Figure 1.1 Reaction energy diagram for uncatalyzed vs. catalyzed reaction pathways.

Note. Reprinted with permission from Stowe, R. L.; Bischof, S. M.; Konnick, M. M.; Hövelmann, C. H.; Leach-Scampavia, D.; Periana, R. A.; Hashiguchi, B. G. *J. Chem. Educ.* **2014**, 91(4), 550–553, Figure 1. Copyright 2014 American Chemical Society.

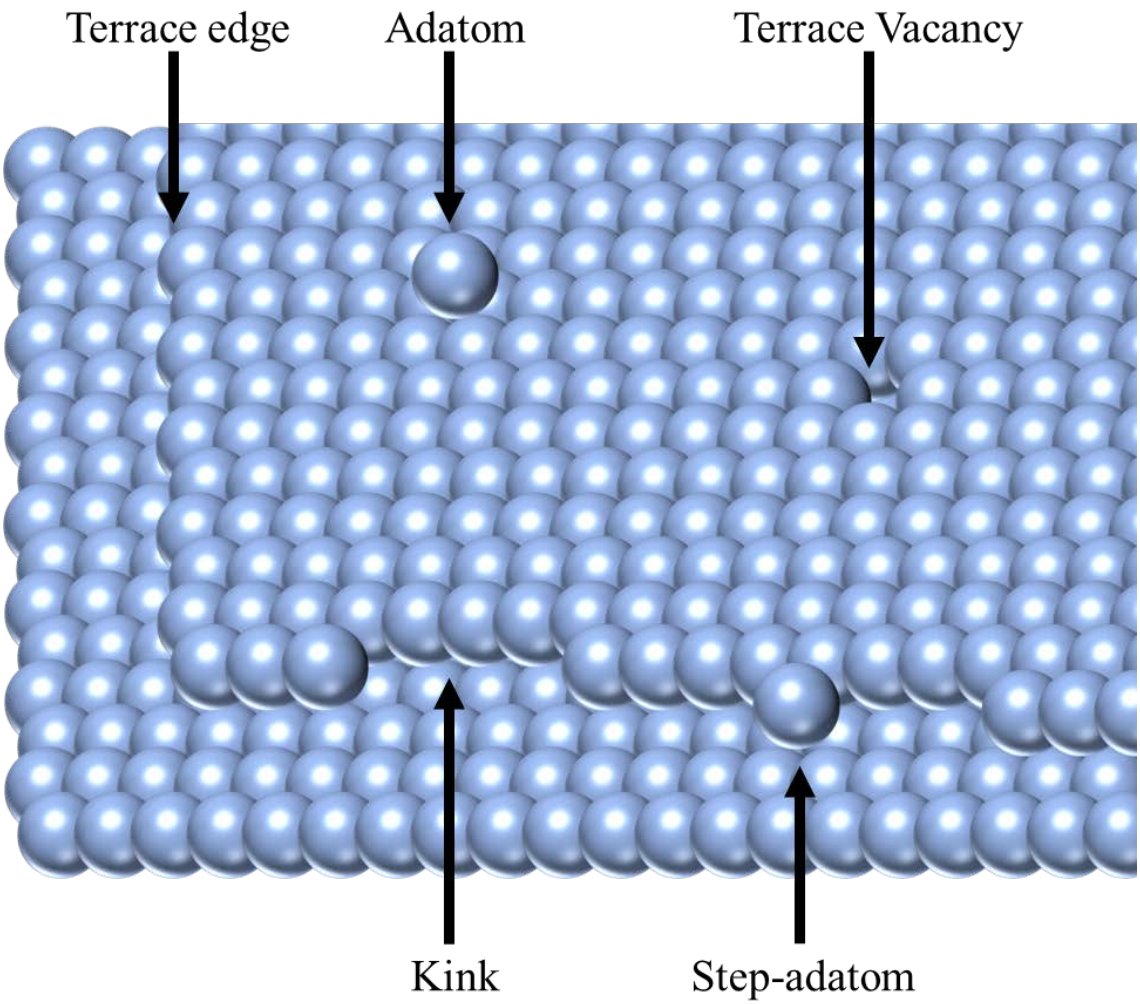

Figure 1.2 Depiction of atom arrangements, with possible active sites identified, on the surface of a solid catalyst.

Note. When compared with bulk materials, the high specific surface area of nanoparticle catalysts gives rise to a high number of catalytically active surface sites known as defect sites.

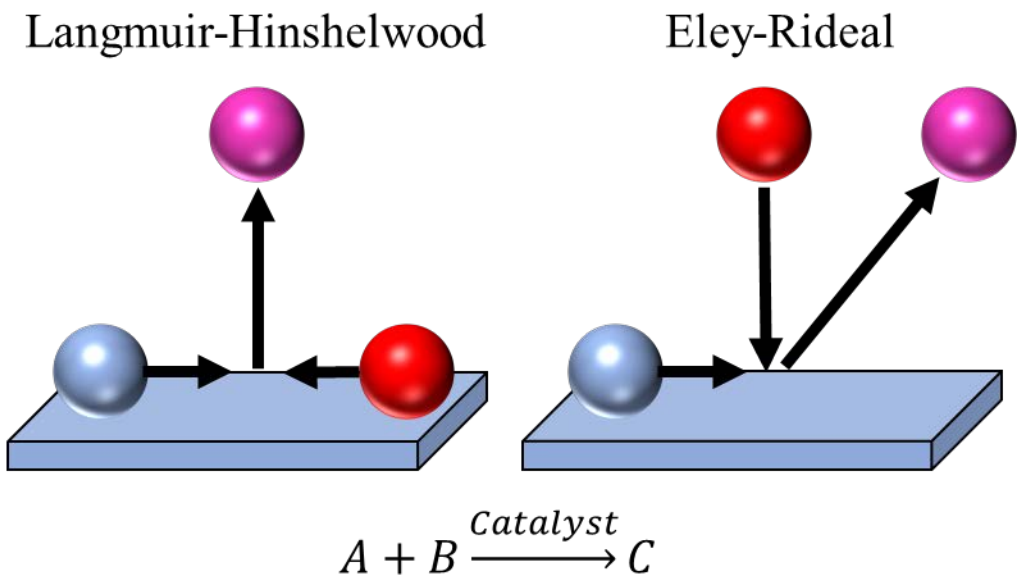

Figure 1.3 Illustration of Langmuir-Hinshelwood and Eley-Rideal catalysis mechanisms.

Note. Catalysis at reactive surfaces is understood to proceed via one of two mechanisms: Langmuir-Hinshelwood or Eley-Rideal.

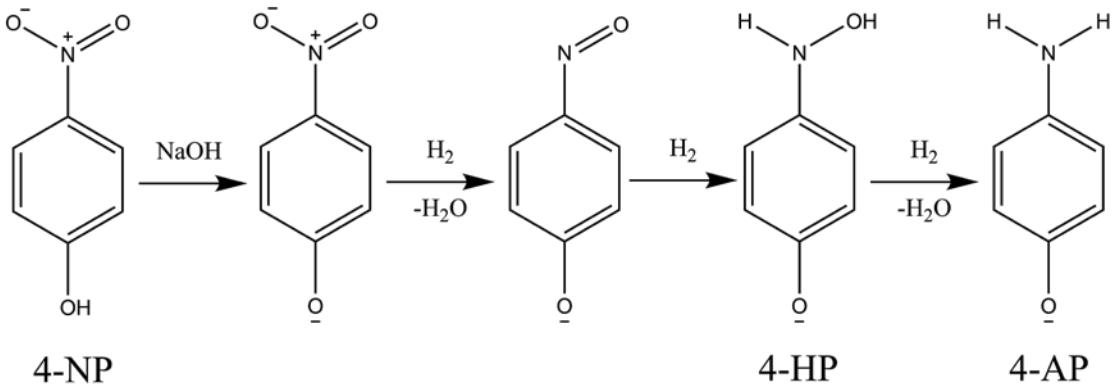

Figure 1.4 Reduction of 4-nitrophenol to 4-aminophenol in a highly basic aqueous environment.

Note. Reduction of 4-NP to 4-AP is a multistep process with the final step, reduction of 4-HP to 4-AP, being the slow, or rate-limiting, step.

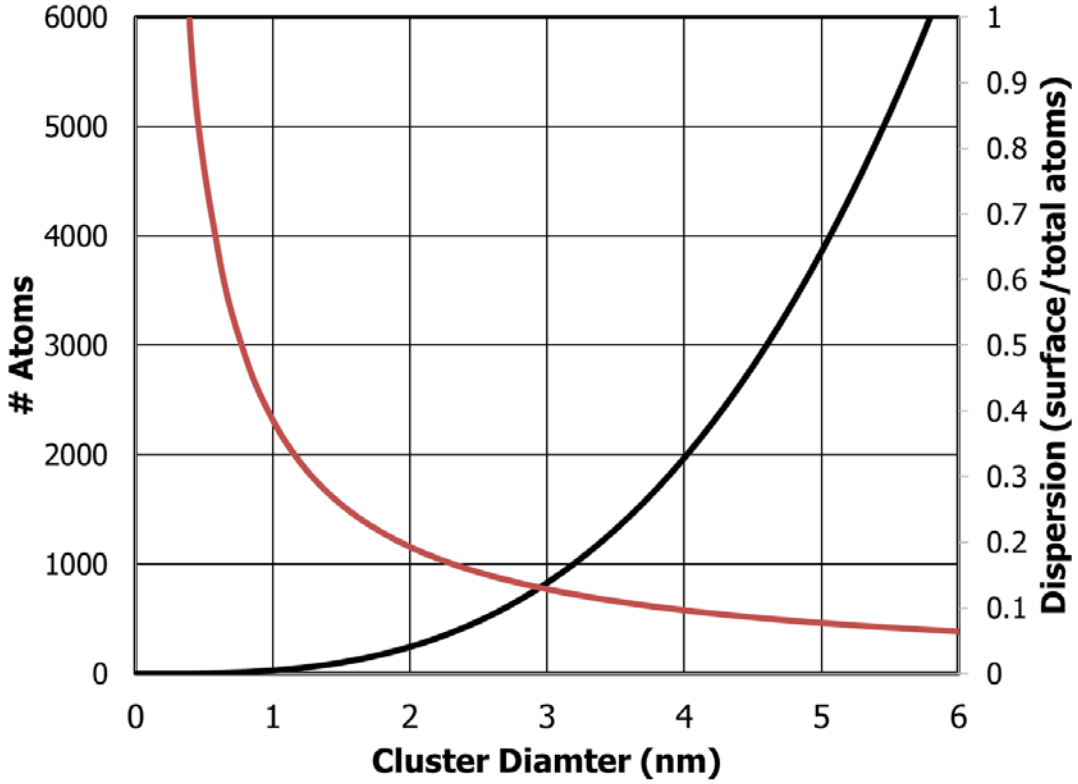

Figure 1.5 Number of atoms in gold clusters
and the associated dispersion factors.

Note. Ultra-small clusters of transition metals, such as gold, contain hundreds to a few thousand atoms when cluster sizes are limited to those less than 5–10 nm. (Figure produced using equations in Zhu[25]).

1.9 References

1. Stowe, R. L.; Bischof, S. M.; Konnick, M. M.; Hövelmann, C. H.; Leach-Scampavia, D.; Periana, R. A.; Hashiguchi, B. G. Making Water the Exciting Way: A Classroom Demonstration of Catalysis. *J. Chem. Educ.* **2014,** *91* (4), 550-553.

2. Crampton, A. S.; Rötzer, M. D.; Ridge, C. J.; Schweinberger, F. F.; Heiz, U.; Yoon, B.; Landman, U. Structure Sensitivity in the Nonscalable Regime Explored via Catalysed Ethylene Hydrogenation on Supported Platinum Nanoclusters. *Nat. Commun.* **2016,** *7*, 10389.

3. Crampton, A. S.; Rötzer, M. D.; Ridge, C. J.; Yoon, B.; Schweinberger, F. F.; Landman, U.; Heiz, U. Assessing the concept of structure sensitivity or insensitivity for sub-nanometer catalyst materials. *Surf. Sci.* **2016,** *652*, 7-19.

4. Petushkov, A.; Ndiege, N.; Salem, A. K.; Larsen, S. C. Chapter 7—Toxicity of Silica Nanomaterials: Zeolites, Mesoporous Silica, and Amorphous Silica Nanoparticles. In *Advances in Molecular Toxicology*, James, C. F., Ed.; Elsevier: Amsterdam, The Netherlands, 2010; Vol. 4, pp 223-266.

5. Schauermann, S.; Nilius, N.; Shaikhutdinov, S.; Freund, H.-J. Nanoparticles for Heterogeneous Catalysis: New Mechanistic Insights. *Acc. Chem. Res.* **2013,** *46* (8), 1673-1681.

6. Somorjai, G. A.; Li, Y. Introduction to Surface Chemistry and Catalysis. 2nd ed.; John Wiley & Sons: Hoboken, New Jersey, 2010; pp 580–584.

7. Somorjai, G. A.; Contreras, A. M.; Montano, M.; Rioux, R. M. Clusters, surfaces, and catalysis. *Proc. Natl. Acad. Sci. U.S.A.* **2006,** *103* (28), 10577-10583.

8. Somorjai, G. A.; Park, J. Y. Molecular Surface Chemistry by Metal Single Crystals and Nanoparticles from Vacuum to High Pressure. *Chem. Soc. Rev.* **2008,** *37* (10), 2155-2162.

9. Li, Y.; Somorjai, G. A. Nanoscale Advances in Catalysis and Energy Applications. *Nano Lett.* **2010,** *10* (7), 2289-2295.

10. Keith, L.; Telliard, W. ES&T Special Report: Priority Pollutants: Ia Perspective View. *Environ. Sci, Technol.* **1979,** *13* (4), 416-423.

11. Li, M.; Chen, G. Revisiting Catalytic Model Reaction *p*-Nitrophenol/$NaBH_4$ Using Metallic Nanoparticles Coated on Polymeric Spheres. *Nanoscale* **2013,** *5* (23), 11919-11927.

12. Menumerov, E.; Hughes, R. A.; Neretina, S., Catalytic Reduction of 4-Nitrophenol: A Quantitative Assessment of the Role of Dissolved Oxygen in Determining the Induction Time. *Nano Lett.* **2016,** *16* (12), 7791-7797.

13. Gu, S.; Wunder, S.; Lu, Y.; Ballauff, M.; Fenger, R.; Rademann, K.; Jaquet, B.; Zaccone, A. Kinetic Analysis of the Catalytic Reduction of 4-Nitrophenol by Metallic Nanoparticles. *J. Phys. Chem. C* **2014,** *118* (32), 18618-18625.

14. Minkina, V. G.; Shabunya, S. I.; Kalinin, V. I.; Martynenko, V. V.; Smirnova, A. L. Stability of Alkaline Aqueous Solutions of Sodium Borohydride. *Int. J. Hydrogen Energy* **2012,** *37* (4), 3313-3318.

15. Yu, L.; Matthews, M. A. Hydrolysis of Sodium Borohydride in Concentrated Aqueous Solution. *Int. J. Hydrogen Energy* **2011,** *36* (13), 7416-7422.

16. Ciganda, R.; Li, N.; Deraedt, C.; Gatard, S.; Zhao, P.; Salmon, L.; Hernández, R.; Ruiz, J.; Astruc, D. Gold Nanoparticles as Electron Reservoir Redox Catalysts for 4-Nitrophenol Reduction: A Strong Stereoelectronic Ligand Influence. *Chem. Commun.* **2014,** *50* (70), 10126-10129.

17. Cortie, M. B.; Van der Lingen, E. *Catalytic Gold Nano-Particles*. Materials Forum. Institute of Materials Engineering Australasia Ltd, 2002.

18. Vines, F.; Gomes, J. R. B.; Illas, F. Understanding the Reactivity of Metallic Nanoparticles: Beyond the Extended Surface Model for Catalysis. *Chem. Soc. Rev.* **2014,** *43* (14), 4922-4939.

19. Haruta, M.; Kobayashi, T.; Sano, H.; Yamada, N. Novel Gold Catalysts for the Oxidation of Carbon Monoxide at a Temperature Far Below 0 ^{o}C. *Chem. Lett.* **1987,** *16* (2), 405-408.

20. Corma, A.; Garcia, H. Supported Gold Nanoparticles as Catalysts for Organic Reactions. *Chem. Soc. Rev.* **2008,** *37* (9), 2096-2126.

21. Gao, F.; Goodman, D. W. Model Catalysts: Simulating the Complexities of Heterogeneous Catalysts. *Annu. Rev. Phys. Chem.* **2012,** *63* (1), 265-286.

22. Boudart, M. Turnover Rates in Heterogeneous Catalysis. *Chem. Rev.* **1995,** *95* (3), 661-666.

23. Roldan Cuenya, B. Metal Nanoparticle Catalysts Beginning to Shape-Up. *Acc. Chem. Res.* **2012,** *46* (8), 1682-1691.

24. Roldan Cuenya, B.; Behafarid, F. Nanocatalysis: Size- and Shape-Dependent Chemisorption and Catalytic Reactivity. *Surf. Sci. Rep.* **2015,** *70* (2), 135-187.

25. Zhu, Q.-L.; Zhong, D.-C.; Demirci, U. B.; Xu, Q. Controlled Synthesis of Ultrafine Surfactant-Free NiPt Nanocatalysts toward Efficient and Complete Hydrogen Generation from Hydrazine Borane at Room Temperature. *ACS Catal.* **2014,** *4* (12), 4261-4268.

26. Boudart, M.; Djéga-Mariadassou, G. *Kinetics of Heterogeneous Catalytic Reactions*.

Princeton University Press, 2014.

27. Pozun, Z. D.; Rodenbusch, S. E.; Keller, E.; Tran, K.; Tang, W.; Stevenson, K. J.; Henkelman, G. A Systematic Investigation of *p*-Nitrophenol Reduction by Bimetallic Dendrimer Encapsulated Nanoparticles. *J. Phys. Chem. C* **2013,** *117* (15), 7598-7604.

28. Wunder, S.; Polzer, F.; Lu, Y.; Mei, Y.; Ballauff, M. Kinetic Analysis of Catalytic Reduction of 4-Nitrophenol by Metallic Nanoparticles Immobilized in Spherical Polyelectrolyte Brushes. *J. Phys. Chem. C* **2010,** *114* (19), 8814-8820.

29. Kim, T.; Lee, C.-H.; Joo, S.-W.; Lee, K. Kinetics of Gold Nanoparticle Aggregation: Experiments and Modeling. *J. Colloid Interface Sci.* **2008,** *318* (2), 238-243.

30. Campbell, C. T.; Sellers, J. R. Anchored Metal Nanoparticles: Effects of Support and Size on Their Energy, Sintering Resistance and Reactivity. *Faraday Discuss.* **2013,** *162*, 9-30.

31. Wang, W.; Meng, Z.; Zhang, Q.; Jia, X.; Xi, K. Synthesis of Stable Au–SiO_2 Composite Nanospheres with Good Catalytic Activity and SERS Effect. *J. Colloid Interface Sci.* **2014,** *418* (0), 1-7.

32. Chen, J.; Xue, Z.; Feng, S.; Tu, B.; Zhao, D. Synthesis of Mesoporous Silica Hollow Nanospheres with Multiple Gold Cores and Catalytic Activity. *J. Colloid Interface Sci.* **2014,** *429* (0), 62-67.

33. El-Sheikh, S. M.; Ismail, A. A.; Al-Sharab, J. F. Catalytic Reduction of p-Nitrophenol Over Precious Metals/Highly Ordered Mesoporous Silica. *New J. Chem.* **2013,** *37* (8), 2399-2407.

34. Ray, S.; Takafuji, M.; Ihara, H. Amino-Acid-Based, Lipid-Directed, In Situ Synthesis and Fabrication of Gold Nanoparticles on Silica: A Metamaterial Framework with Pronounced Catalytic Activity. *Nanotechnology* **2012,** *23* (49), 495301.

35. Xie, W.; Walkenfort, B.; Schluecker, S. Label-Free SERS Monitoring of Chemical Reactions Catalyzed by Small Gold Nanoparticles Using 3D Plasmonic Superstructures. *J. Am. Chem. Soc.* **2013,** *135* (5), 1657-1660.

36. Ren, X.; Tan, E.; Lang, X.; You, T.; Jiang, L.; Zhang, H.; Yin, P.; Guo, L. Observing Reduction of 4-Nitrobenzenthiol on Gold Nanoparticles In Situ Using Surface-Enhanced Raman Spectroscopy. *PCCP* **2013,** *15* (34), 14196-14201.

37. Stöber, W.; Fink, A.; Bohn, E. Controlled Growth of Monodisperse Silica Spheres in the Micron Size Range. *J. Colloid Interface Sci.* **1968,** *26* (1), 62-69.

38. Küstner, B.; Gellner, M.; Schütz, M.; Schöppler, F.; Marx, A.; Ströbel, P.; Adam, P.; Schmuck, C.; Schlücker, S. SERS Labels for Red Laser Excitation: Silica-Encapsulated SAMs on Tunable Gold/Silver Nanoshells. *Angew. Chem. Int. Ed.* **2009,** *48* (11), 1950-1953.

39. Quast, A. D.; Bornstein, M.; Greydanus, B. J.; Zharov, I.; Shumaker-Parry, J. S. Robust Polymer-Coated Diamond Supports for Noble-Metal Nanoparticle Catalysts. *ACS Catal.* **2016**, 4729-4738.

40. Zhou, J.; Ren, F.; Wu, W.; Zhang, S.; Xiao, X.; Xu, J.; Jiang, C. Controllable Synthesis and Catalysis Application of Hierarchical PS/Au Core–Shell Nanocomposites. *J. Colloid Interface Sci.* **2012,** *387* (1), 47-55.

41. Pocklanova, R.; Rathi, A. K.; Gawande, M. B.; Datta, K. K. R.; Ranc, V.; Cepe, K.; Petr, M.; Varma, R. S.; Kvitek, L.; Zboril, R. Gold Nanoparticle-Decorated Graphene Oxide: Synthesis and Application in Oxidation Reactions Under Benign Conditions. *J. Mol. Catal. A: Chem.* **2016,** *424*, 121-127.

42. Damato, T. C.; de Oliveira, C. C. S.; Ando, R. A.; Camargo, P. H. C. A Facile Approach to TiO2 Colloidal Spheres Decorated with Au Nanoparticles Displaying Well-Defined Sizes and Uniform Dispersion. *Langmuir* **2013,** *29* (5), 1642-1649.

43. Layek, K.; Kantam, M. L.; Shirai, M.; Nishio-Hamane, D.; Sasaki, T.; Maheswaran, H. Gold Nanoparticles Stabilized on Nanocrystalline Magnesium Oxide as an Active Catalyst for Reduction of Nitroarenes in Aqueous Medium at Room Temperature. *Green Chem.* **2012,** *14* (11), 3164-3174.

44. Davies, G. *Diamond* Adam Hilger, Bristol, 1984.

45. Bundy, F. P.; Hall, H. T.; Strong, H. M.; Wentorf, R. H. Man-Made Diamonds. *Nature* **1955,** *176* (4471), 51-55.

46. Angus, J. C. Diamond Synthesis by Chemical Vapor Deposition: The Early Years. *Diamond Relat. Mater.* **2014,** *49*, 77-86.

47. Isakova, V. G.; Isakov, V. P. Thermal Oxidation Initiated in Explosive Detonation Products by Exothermal Pyrolysis of Metal Acetylacetonates. *Phys. Solid State* **2004,** *46* (4), 622-624.

CHAPTER 2

EXPLOITING INTRINSIC IMPURITIES OF HPHT DIAMOND FOR CATALYSIS[1]

2.1 Introduction

High-pressure high-temperature (HPHT) diamond is widely used as an abrasive and more recently has proven to be a versatile material for applications ranging from chemical separations to its use as a support for catalytically active nanoparticles (NPs).[1-3] It has been previously demonstrated that catalytically active AuNPs have been attached to both bare HPHT nanodiamond (ND) surfaces as well as thiol-ene polymer-coated ND. As shown in Chapter 4 of this work, we have noted that bare HPHT ND demonstrates the ability to catalyze the reduction of 4-nitrophenol, while thiol-ene polymer-coated ND revealed negligible catalytic activity.[1, 4-5] One possible explanation for this difference in catalytic activity is the presence of metallic impurities in HPHT ND.

HPHT diamond is produced in large belt presses using a carbon source and finely powdered metal catalysts/solvents (commonly Fe, Ni, and Co). At the high pressures and temperatures (~10 GPa and >2,000 °C) used to produce HPHT diamond, the graphite and metal catalysts liquefy and diamond crystal growth proceeds slowly over the course of many hours, days, or weeks, depending on the final crystal size.[6-7] Once removed from

[1] All experimental work in this chapter was performed by the author with the exception of the following: UV-Vis absorption spectroscopy experiments were performed by Rebecca Luke and BET measurements were obtained through the Metallurgy Department analytical facilities.

the press, subsequent size reduction via milling breaks larger diamond crystals into smaller ones with larger surface areas. These diamond powders with varied sizes are cleaned using strong acid baths and separated. However, even with rigorous cleaning, a variety of impurities inherent to the production process persist.[8] The metal catalysts used in initial diamond crystal formation exist as metal impurities homogeneously distributed throughout the diamond particles. Although extensive cleaning using strong acids may remove some dissolvable exposed surface metals, impurities in the interior of the particles are unlikely to be removed by even the most stringent cleaning protocols.[9] In addition, interactions between diamond particles after cleaning can result in fracturing and breakage, yielding fresh diamond surfaces and exposing metal impurities that had previously been buried in the interior.

Exhaustive characterization of HPHT ND by the Linford group and others has shown ND to be a complex material best described as a composite with a number of noncarbon impurities. Inductively coupled plasma optical-emission spectroscopy or mass spectrometry (ICP-OES or ICP-MS), X-ray fluorescence (XRF), X-ray absorption near-edge structure (XANES), and proton induced X-ray emission (PIXE) have been used to observe these intrinsic impurities in HPHT ND.[9-10] These studies showed impurities in concentrations ranging from sub-ppb levels to those exceeding ppm that were not completely removed even after several acid washings. The analysis by Linford and co-workers identified several metals, including Al, Cr, Cu, Fe, Mn, Mo, Ni, K, Ti, W, Ca, and Co. The variety of elements present suggests that ND synthesis, milling, and size separation result in a complicated multicomponent material.

Although these intrinsic impurities may be undesirable in some applications, for

others, such as chemical catalysis, metal impurities might be desirable. We hypothesized that if the inclusions of metal impurities were accessible at the surface of these NDs, then they would be capable of acting as catalysts. The possibility of using metal impurities in ND as catalysts was bolstered by studies of metal nanoparticles at oxide surfaces, where Cu, Fe, Ni, Ti, and Co had been successfully incorporated into a wide variety of catalytically active composite materials.[4, 11-13]

Using the catalytic reduction of 4-NP, we investigated the role of low-level impurities in HPHT diamond powders as possible catalysts in a highly basic aqueous environment. In order to address any potential heterogeneity of impurities that may exist from different manufacturers, we purchased five different powders from four manufactures of HPHT diamond. The work detailed here shows that these intrinsic metallic impurities are indeed catalytically active in the 4-NP reduction reaction.

2.2 Materials and Methods

2.2.1 Reagents

All water was obtained from a Barnstead NANOPure Diamond Ultrapure water system with the typical resistivity measuring 18.2 MΩ-cm. TraceSELECT HCl and HNO_3 were obtained from Sigma-Aldrich for ICP-OES analysis. Sodium borohydride powder, $NaBH_4$, 98 +%, was obtained from Acros Organics. Sodium hydroxide pellets (NaOH) certified ACS grade were obtained from Fisher Scientific. Finally, 4-nitrophenol (4-NP) ReagentPlus, ≥99% was obtained from Sigma Aldrich.

2.2.2 UV-Vis Absorption Analysis

Two Hellma Analytics UV Quartz Suprasil (200-2500 nm, 3.5 mL, 10 mm path length) fluorescence cuvettes with wells for magnetic stirrers were used for all UV-Vis absorption spectroscopy measurements. Prior to use, each cuvette (including the stir bar) was cleaned using copious amounts of water and then filled with aqua regia (3:1 conc HCl: HNO_3) and allowed to sit for 5 min to remove any metallic contaminants from previous experiments. Aqua regia rinsing was repeated three times to ensure complete removal of trace contaminants. After the third rinse, the cuvettes were washed with water five times each. One cuvette was filled with water and used as the blank. The second cuvette was dried with N_2 and exact masses were obtained for each addition to the sample cuvette to ensure repeatability. A fresh stock solution of $NaBH_4$ in 1M NaOH was prepared for each run by combining 2.5 g of 1 M NaOH and 0.008 g of $NaBH_4$. Stock 4-NP solution was prepared with 0.00270 g of 4-NP and 20.710 g of water. The sample cuvette was tared on an analytical balance and 0.554 g of the $NaBH_4$ stock solution was added using an auto pipette. To the same cuvette, 0.05 g of the 4-nitrophenol solution was added, followed by the addition of 1.88 g of water. The cuvettes were placed in the UV-Vis instrument (Perkin-Elmer Lambda 750 UV/Vis/VIR spectrophotometer) in temperature-controlled Peltier cells (Quantum Northwest Inc., Liberty Lake, WA). Both the sample and reference were heated to 25 °C and stirred at a rate of 1000 rpm. Stock nanodiamond/water solutions were prepared by sonicating in a bath sonicator and thoroughly mixing 0.05 g nanodiamond powder with 124 g water. While stirring vigorously, 0.05 g of the nanodiamond stock solution was added using an auto pipette. The exact mass of added nanodiamond stock solution was obtained by recording the mass

before and after the reaction was complete. The absorbance at 400 nm was monitored until a flat baseline was observed using a PerkinElmer Lambda 750 UV/Vis/NIR spectrophotometer.

2.2.3 Brunauer-Emmett-Teller (BET) Analysis

BET specific surface area analysis was performed on a Micromeritics ASAP-2020 analyzer using nitrogen adsorption and desorption isotherms at -195.6 °C after samples were degassed under vacuum at 250 °C for 3 h.

2.2.4 Inductively Coupled Plasma Optical Emission Spectroscopy (ICP-OES)

Elemental stock **s**tandards were obtained from Inorganic Ventures (Christianburg, VA) as pure acid stabilized solutions which were diluted to obtain calibration plots between 0.05 and 1 ppm. HPHT diamond powders were digested in Aqua Regia (3:1 HCl:HNO_3) for 48 h prior to dilution in a ~5% HNO_3 matrix where final sample concentrations were within the range of linearity for the standard calibration plots. Analysis was carried out on a Thermo Scientific iCAP 6000 series ICP spectrometer.

2.2.5 Transmission Electron Microscopy (TEM)

TEM images were obtained using a JEOL 2800 S/TEM operating in conventional TEM mode at an accelerating potential of 200 kV. Samples were prepared from water dispersions using 3-5 µL dropped onto lacey formvar/carbon, 400 mesh, copper grids (Ted Pella Prod # 01885-F) and allowed to dry before imaging.

2.3 Results and Discussion

Five ND powder samples from four vendors were imaged using transmission electron microscopy (TEM), allowing direct comparison of the nanoscale morphological structure of these different ND powders. The images in Figure 2.1 clearly show that these HPHT ND powders are solid, nonporous materials with a wide range of sizes. Close inspection of the TEM images reveals that the smallest particles have a tendency to flocculate and stick to the surface of the largest particles. Primary particle sizes are observed to range between single-digit nm particles to the largest particles of several hundred nanometers. Complete dispersal of all primary particles is problematic, and often surface functionalization is used to enhance colloidal stability.[14-19]

While TEM imaging is useful for the direct inspection of these ND powders, the range of particle sizes seen in TEM poses a significant characterization problem. The limited information from the manufacturer includes size distributions which would seem to indicate that the ND powder sizes are extremely similar in size. Further inquiry into these data from the manufacturers revealed that the given size for each ND powder is merely a product category, which might vary from vendor to vendor and as such cannot be relied upon for quantitative comparison. The similar results likely originate with the techniques used to determine particle size, such as dynamic light scattering (DLS), which is prone to errors associated with particle flocculation and assumptions of spherical particles being monomodal.[20] The images in Figure 2.1 show that these assumptions would likely lead to large errors due to the nonmonomodal and nonspherical nature of ND. Other techniques, such as electrozone counting and disk centrifugation, are also used for diamond particle sizing; however, the heterogeneity of particle shapes, sizes, and

aggregation leads to a large degree of uncertainty. For these reasons, we chose not to use particle size as the discriminating property for these ND powders, and instead used surface area because of its direct relationship to potential surface sites that might be responsible for the observed heterogeneous catalysis.

BET theory was used for specific surface area (SSA) analysis of nitrogen absorption/desorption isotherms, allowing direct comparison of the diamond surfaces accessible to reactants during catalysis. The SSAs, shown in Table 2.1, provide a more quantitative comparison of an important ND surface property that is directly related to heterogeneous catalysis. The SSAs range in magnitude from 14 to 42 m^2/g, and comparison with the manufacturer-provided particle sizes reveals that indeed, nominally similar particle size classifications are readily distinguishable by SSA.

Besides SSAs, another quantifiable parameter that we would expect to be related to our observation of heterogeneous catalysis is metal content. Although Linford and co-workers identified many potentially active catalytic metal impurities in HPHT ND, we limited our analysis to the metal impurities with the largest concentrations observable using ICP-OES; namely Fe and Ni. Table 2.1 summarizes the results of elemental analysis using ICP-OES and confirms that both Fe and Ni exist as acid-leachable surface impurities present at concentrations of ppt or lower. Both of these metals are expected to be highly active as catalysts, capable of reducing 4-NP[21-25]; however, these impurities must be relatively dispersed because TEM fails to reveal obvious regions of high contrast due to increased electron scattering, as would be expected if the metallic impurities existed as nanoparticles.

We evaluated the activity of metal impurities in ND with a model reaction

catalyzed by transition metal nanoparticles. The reduction of 4-nitrophenol (4-NP) to 4-aminophenol (4-AP) by the mild reducing agent sodium borohydride ($NaBH_4$) allows facile monitoring of the catalytic activity of metals in aqueous environments using UV-visible absorption spectroscopy. Advantages to this reaction include an easily visible color change from yellow to colorless, the absence of side products, $NaBH_4$ alone not being capable of reducing 4-NP, and upon addition of an appropriate metal catalyst, the conversion to 4-AP readily occurring.

Using UV-Vis absorption spectroscopy as an indirect probe of the activity of these various trace impurities allows for the bulk determination of the catalytic activity. The 4-nitrophenolate ion (4-NP) exhibits a characteristic absorbance at 400 nm, giving aqueous solutions a bright yellow color.[26] The reduction product, 4-AP, has a weaker characteristic UV absorbance at 300 nm. By monitoring the absorbance of 4-NP at 400 nm, a direct relationship between absorbance and reaction progress can be observed. Figure 2.2 is an example of a time-resolved plot for the reduction reaction progress when using ND powder as the catalytically active material. Initial addition of the ND powder causes the optical density of the solution to increase dramatically, followed by an induction period in which dissolved oxygen is consumed, while further changes in absorbance are solely due to catalytic conversion of 4-NP to 4-AP.[27] After some time, the cloudy solution (due to ND powder dispersion) changes from yellow to colorless and the changes in absorbance become negligible. It is essential to note that ample empirical evidence revealed that hydrogen bubbles evolved from aqueous $NaBH_4$ decomposition and made reproducible data acquisition impossible under pH neutral reaction conditions. Preparation of the aqueous $NaBH_4$ solution in 1 M NaOH (pH ~14) increased the stability

of the dissolved $NaBH_4$ dramatically and eliminated the problematic evolution of hydrogen bubbles.[28-29] The preparation of reaction solutions in this highly basic environment was found to be necessary for data collection.

The apparent rate constant (k_{app}) for this reaction was determined by only considering the highest initial rate of change.[1, 30, 31, 32-34] This fitting region corresponds to roughly 1400 seconds centered at the highest slope region of a linearized natural log plot of the data. Using a nonlinear least squares fitting approach, k_{app} was readily determined for five trials of each ND powder. Although observation of changes in reactant and product concentrations is straightforward using UV-Vis spectrophotometry, it is not possible to determine turn-over-frequencies (TOFs). The restriction to using k_{app} instead of TOFs in this case is in large part due to the impossibility of direct determination of the number and quality of catalytically active sites owing to the many impurities in the ND powders, making this task impossibly complex.[35-36]

The catalytic activity of these ND powders follows similar trends, as shown by others such as Wunder et al. examining the role of ligand/surface stabilized metal nanoparticles in the reduction of 4-NP. The reduction can be assumed to be pseudo-first order in the initial postinduction period region.[30-32, 37] With the exception of the Eastwind Diamond (125 nm) sample, with a SSA of 41 m^2/g and a k_{app} of 125 s^{-1}, comparison of the k_{app} to the BET SSAs appears to scale linearly with SSA. As seen in Figure 2.3, this correlation between k_{app} and surface area may be due to the fact that higher-surface-area powders expose more of the metallic impurities responsible for the catalytic reduction of 4-NP to 4-AP. The mismatch between the k_{app} and BET SSA for the Advanced Abrasives ND powder might be due to elevated catalytic activity for metal impurities not evaluated

in this study, because these impurities may be present at such low concentrations that they are not readily observable using ICP-OES; however, despite the low concentration, the impurities may provide highly active sites for catalysis.

2.4 Conclusions

To our knowledge, this work is the first demonstration that unmodified HPHT nanodiamond powders are suitable catalysts for aqueous reduction of nitrophenols. The observation we make here of catalytically active ND powder impurities is doubtless useful for some applications; however, we have previously shown that thin films of thiol-ene polymers attached to ND powders passivate these catalytically active surface impurities.[1] It is possible that other coating methods would also passivate these active surface species. Nevertheless, future work in the catalytic reduction of 4-NP by ND-supported catalysts will require researchers to mitigate the possible participation of catalytically active surface species on HPHT ND powders. Future work may focus on exploring the influence of surface functionalities on catalytic efficiencies as these surface groups modulate access to active surface impurities. Perhaps an improved understanding of how accessibility of surface-active sites changes catalytic activity will improve heterogeneous catalyst design based on inexpensive ND powders.

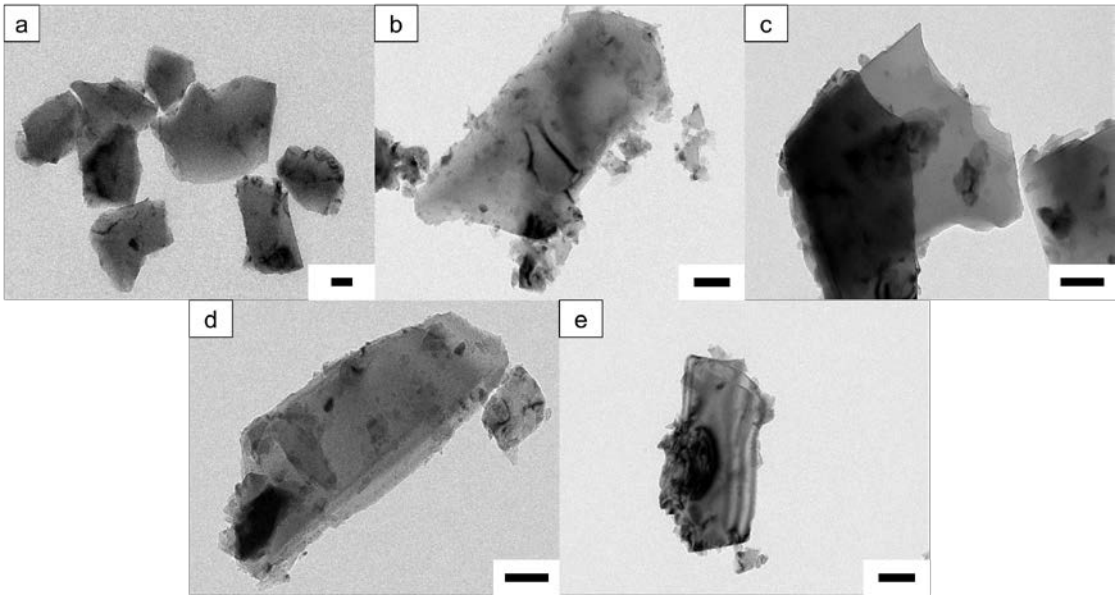

Figure 2.1 TEM images of bare ND with nominal sizes indicated by the manufacturers.

Note. a = Eastwind Diamond (0.25 µm); b = Advanced Abrasives (0-0.5 µm); c = Diamond Tech (0-0.5 µm); d = Eastwind Diamond (0.125 µm); e = Microdiamant (0-0.5 µm). All scale bars are 100 nm.

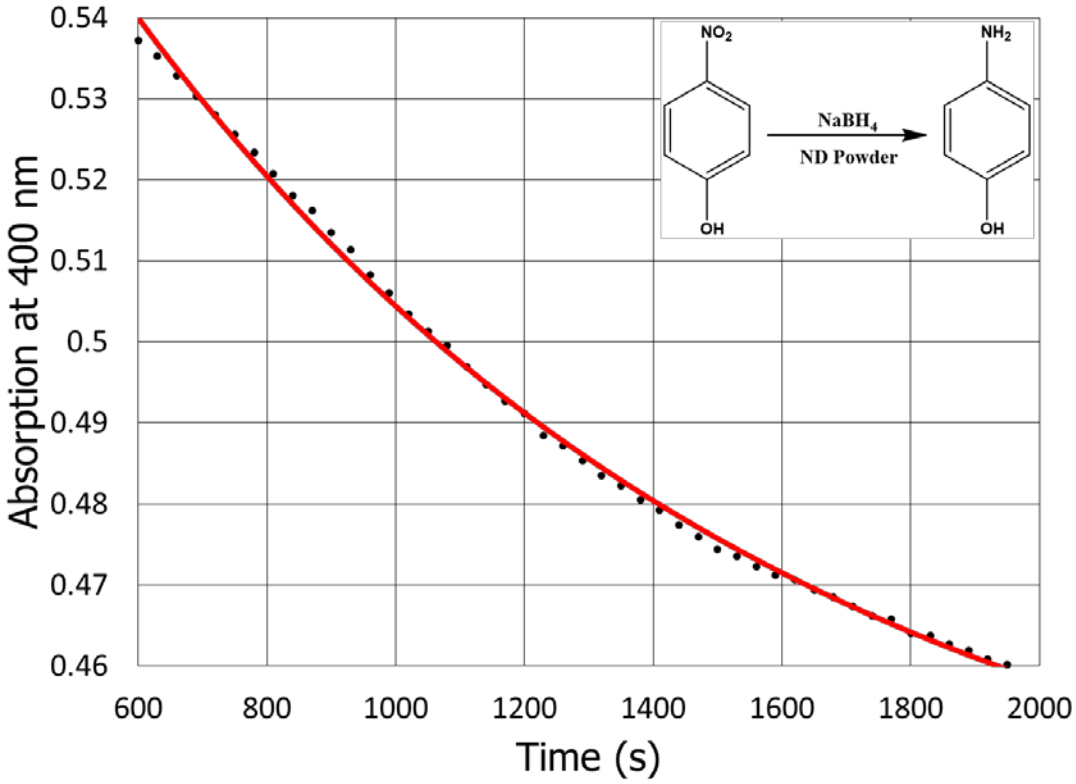

Figure 2.2 Example plot of the measured absorbance of 4-NP at 400 nm during the course of the catalytic reduction.

Note. Representative reaction using Advanced Abrasives ND powder. The experimental data (black) are plotted along with a single-component nonlinear least squares exponential fit (red).

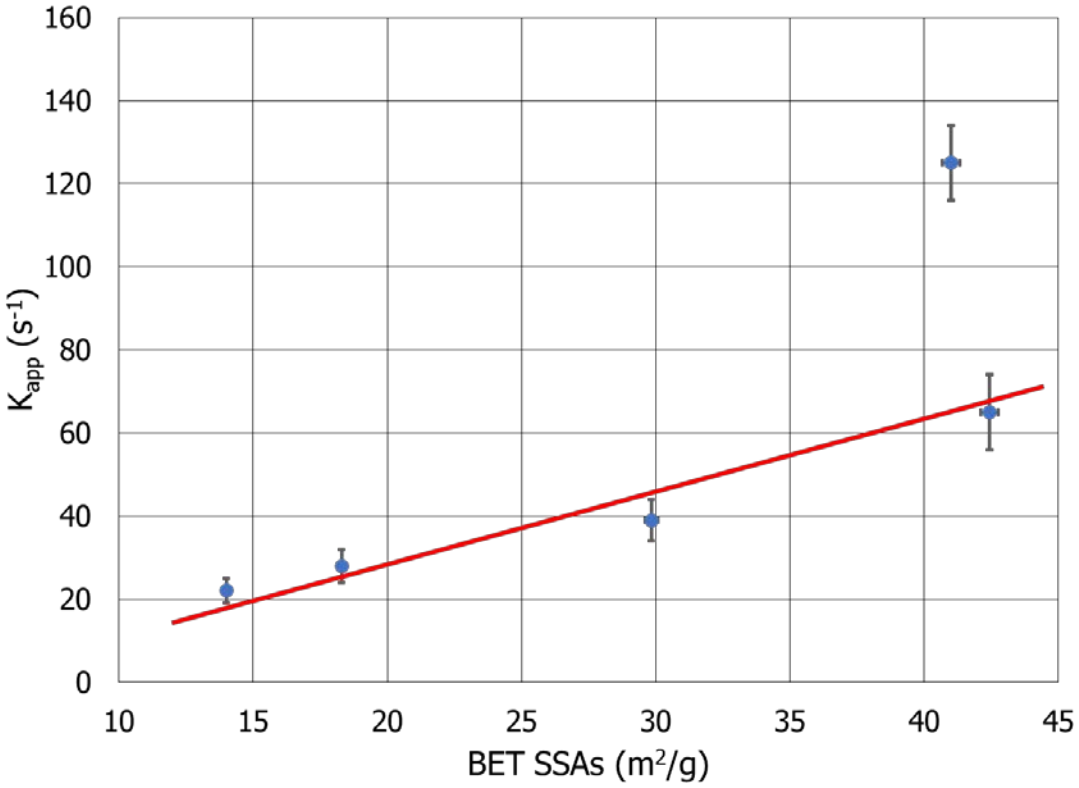

Figure 2.3 Plot of the apparent rate constant as
a function of BET determined SSAs.

Note. The red line is included as a guide to the eye, showing a possible linear relationship between the two parameters.

Table 2.1

Comparison of ND Powders From Several Vendors With Associated Manufacturer Product Size Classification, BET SSAs, Fe and Ni Concentrations, and Catalytic Efficiencies of HPHT Diamond Powders Expressed as k_{app}

Manufacturer[a]	Size[a] (nm)	BET Specific Surface Area (m^2/g)	g Fe per g Diamond	g Ni per g Diamond	k_{app} (s^{-1}) / g Diamond	σ k_{app} (s^{-1}) / g Diamond
Eastwind Diamond	250	14	$2.2x10^{-8}$	$1.9x10^{-10}$	22	3
Diamond Tech	0-500	18	$6.6x10^{-8}$	$2.7x10^{-9}$	28	4
Microdiamant	0-500	30	$5.3x10^{-8}$	$7.3x10^{-10}$	39	5
Eastwind Diamond	125	41	$1.6x10^{-8}$	$1.9x10^{-10}$	125	9
Advanced Abrasives	0-500	42	$4.3x10^{-7}$	$2.1x10^{-8}$	65	9

[a] Product description provided by manufacturer.

2.5 References

1. Quast, A. D.; Bornstein, M.; Greydanus, B. J.; Zharov, I.; Shumaker-Parry, J. S. Robust Polymer-Coated Diamond Supports for Noble-Metal Nanoparticle Catalysts. *ACS Catal.* **2016**, 4729-4738.

2. Wiest, L. A.; Jensen, D. S.; Hung, C.-H.; Olsen, R. E.; Davis, R. C.; Vail, M. A.; Dadson, A. E.; Nesterenko, P. N.; Linford, M. R. Pellicular Particles with Spherical Carbon Cores and Porous Nanodiamond/Polymer Shells for Reversed-Phase HPLC. *Anal. Chem*. **2011**, *83* (14), 5488-5501.

3. Saini, G.; Jensen, D. S.; Wiest, L. A.; Vail, M. A.; Dadson, A.; Lee, M. L.; Shutthanandan, V.; Linford, M. R. Core−Shell Diamond as a Support for Solid-Phase Extraction and High-Performance Liquid Chromatography. *Anal. Chem.* **2010**, *82* (11), 4448-4456.

4. Gao, F.; Yang, N.; Nebel, C. E. Highly Stable Platinum Nanoparticles on Diamond. *Electrochim. Acta* **2013**, *112* (0), 493-499.

5. La-Torre-Riveros, L.; Guzman-Blas, R.; Méndez-Torres, A. E.; Prelas, M.; Tryk, D. A.; Cabrera, C. R. Diamond Nanoparticles as a Support for Pt and PtRu Catalysts for Direct Methanol Fuel Cells. *ACS Appl. Mater. Interfaces* **2012**, *4* (2), 1134-1147.

6. Zhang, Y.; Zang, C.; Ma, H.; Liang, Z.; Zhou, L.; Li, S.; Jia, X. HPHT Synthesis of Large Single Crystal Diamond Doped with High Nitrogen Concentration. *Diamond Relat. Mater*. **2008**, *17* (2), 209-211.

7. Palyanov, Y. N.; Kupriyanov, I. N.; Borzdov, Y. M.; Surovtsev, N. V. Germanium: A New Catalyst for Diamond Synthesis and a New Optically Active Impurity in Diamond. *Scientific Reports* 2015, *5*, 14789.

8. Singh, B.; Smith, S. J.; Jensen, D. S.; Jones, H. F.; Dadson, A. E.; Farnsworth, P. B.; Vanfleet, R.; Farrer, J. K.; Linford, M. R. Multi-Instrument Characterization of Five Nanodiamond Samples: A Thorough Example of Nanomaterial Characterization. *Anal. Bioanal. Chem.* **2016**, *408* (4), 1107-1124.

9. Meng, Y.; Newville, M.; Sutton, S.; Rakovan, J.; Mao, H.-K. Fe and Ni Impurities in Synthetic Diamond. *Am. Mineral*. **2003**, *88* (10), 1555-1559.

10. Nunn, N.; Torelli, M.; McGuire, G.; Shenderova, O. Nanodiamond: A High Impact Nanomaterial. *Curr. Opin. Solid State Mater. Sci.* **2017**, *21* (1), 1-9.

11. Damato, T. C.; de Oliveira, C. C. S.; Ando, R. A.; Camargo, P. H. C. A Facile Approach to TiO2 Colloidal Spheres Decorated with Au Nanoparticles Displaying Well-Defined Sizes and Uniform Dispersion. *Langmuir* **2013**, *29* (5), 1642-1649.

12. Gupta, V. K.; Yola, M. L.; Eren, T.; Kartal, F.; Çağlayan, M. O.; Atar, N. Catalytic Activity of Fe@Ag Nanoparticle Involved Calcium Alginate Beads for the Reduction

of Nitrophenols. *J. Mol. Liq*. **2014**, *190*, 133-138.

13. Ma, H.; Wang, H.; Wu, T.; Na, C. Highly Active Layered Double Hydroxide-Derived Cobalt Nano-Catalysts for p-Nitrophenol Reduction. *Appl. Catal., B: Environmental* **2016**, *180*, 471-479.

14. Krueger, A.; Lang, D. Functionality Is Key: Recent Progress in the Surface Modification of Nanodiamond. *Adv. Funct. Mater*. **2012**, *22* (5), 890-906.

15. Mochalin, V. N.; Shenderova, O.; Ho, D.; Gogotsi, Y. The Properties and Applications of Nanodiamonds. *Nat Nano* **2012**, *7* (1), 11-23.

16. Meinhardt, T.; Lang, D.; Dill, H.; Krueger, A. Pushing the Functionality of Diamond Nanoparticles to New Horizons: Orthogonally Functionalized Nanodiamond Using Click Chemistry. *Adv. Funct. Mater*. **2011**, *21* (3), 494-500.

17. Liu, Y.; Gu, Z.; Margrave, J. L.; Khabashesku, V. N. Functionalization of Nanoscale Diamond Powder: Fluoro-, Alkyl-, Amino-, and Amino Acid-Nanodiamond Derivatives. *Chem. Mater.* **2004**, *16* (20), 3924-3930.

18. Krueger, A.; Boedeker, T. Deagglomeration and Functionalisation of Detonation Nanodiamond with Long Alkyl Chains. *Diamond Relat. Mater*. **2008**, *17* (7-10), 1367-1370.

19. Girard, H. A.; Petit, T.; Perruchas, S.; Gacoin, T.; Gesset, C.; Arnault, J. C.; Bergonzo, P. Surface Properties of Hydrogenated Nanodiamonds: A Chemical Investigation. *PCCP* **2011**, *13* (24), 11517-11523.

20. Lim, J.; Yeap, S. P.; Che, H. X.; Low, S. C. Characterization of Magnetic Nanoparticle by Dynamic Light Scattering. *Nano. Lett.* **2013**, *8* (1), 381.

21. Zhao, B.; Mele, G.; Pio, I.; Li, J.; Palmisano, L.; Vasapollo, G. Degradation of 4-Nitrophenol (4-NP) Using Fe–TiO2 as a Heterogeneous Photo-Fenton Catalyst. *J. Hazard. Mater*. **2010**, *176* (1–3), 569-574.

22. Feng, J.; Su, L.; Ma, Y.; Ren, C.; Guo, Q.; Chen, X. CuFe2O4 Magnetic Nanoparticles: A Simple and Eefficient Catalyst for the Reduction of Nitrophenol. *Chem. Eng. J.* **2013**, *221*, 16-24.

23. Sahiner, N.; Ozay, H.; Ozay, O.; Aktas, N. New Catalytic Route: Hydrogels as Templates and Reactors for In Situ Ni Nanoparticle Synthesis and Usage in the Reduction of 2- and 4-Nitrophenols. *Appl. Catal., A: General* **2010**, *385* (1–2), 201-207.

24. Yan, N.; Xiao, C.; Kou, Y. Transition Metal Nanoparticle Catalysis in Green Solvents. *Coord. Chem. Rev*. **2010**, *254* (9–10), 1179-1218.

25. Goyal, A.; Bansal, S.; Singhal, S. Facile Reduction of Nitrophenols: Comparative

Catalytic Efficiency of MFe2O4 (M = Ni, Cu, Zn) Nano Ferrites. *Int. J. Hydrogen Energy* **2014**, *39* (10), 4895-4908.

26. Pradhan, N.; Pal, A.; Pal, T. Silver Nanoparticle Catalyzed Reduction of Aromatic Nitro Compounds. *Colloids Surf., A* **2002**, *196* (2–3), 247-257.

27. Menumerov, E.; Hughes, R. A.; Neretina, S. Catalytic Reduction of 4-Nitrophenol: A Quantitative Assessment of the Role of Dissolved Oxygen in Determining the Induction Time. *Nano Lett*. **2016**, *16* (12), 7791-7797.

28. Minkina, V. G.; Shabunya, S. I.; Kalinin, V. I.; Martynenko, V. V.; Smirnova, A. L. Stability of Alkaline Aqueous Solutions of Sodium Borohydride. *Int. J. Hydrogen Energy* **2012**, *37* (4), 3313-3318.

29. Yu, L.; Matthews, M. A. Hydrolysis of Sodium Borohydride in Concentrated Aqueous Solution. *Int. J. Hydrogen Energy* **2011**, *36* (13), 7416-7422.

30. Gu, S.; Wunder, S.; Lu, Y.; Ballauff, M.; Fenger, R.; Rademann, K.; Jaquet, B.; Zaccone, A. Kinetic Analysis of the Catalytic Reduction of 4-Nitrophenol by Metallic Nanoparticles. *J. Phys. Chem.* ***C*** **2014,** *118* (32), 18618-18625.

31. Wunder, S.; Polzer, F.; Lu, Y.; Mei, Y.; Ballauff, M. Kinetic Analysis of Catalytic Reduction of 4-Nitrophenol by Metallic Nanoparticles Immobilized in Spherical Polyelectrolyte Brushes. *J. Phys. Chem. C* **2010**, *114* (19), 8814-8820.

32. Wunder, S.; Lu, Y.; Albrecht, M.; Ballauff, M. Catalytic Activity of Faceted Gold Nanoparticles Studied by a Model Reaction: Evidence for Substrate-Induced Surface Restructuring. *ACS Catal*. **2011**, *1* (8), 908-916.

33. Antonels, N. C.; Meijboom, R. Preparation of Well-Defined Dendrimer Encapsulated Ruthenium Nanoparticles and their Evaluation in the Reduction of 4-Nitrophenol According to the Langmuir–Hinshelwood Approach. *Langmuir* **2013**, *29* (44), 13433-13442.

34. Nigra, M. M.; Ha, J.-M.; Katz, A. Identification of Site Requirements for Reduction of 4-Nitrophenol Using Gold Nanoparticle Catalysts. *Catal. Sci. Tech*. **2013**, *3* (11), 2976-2983.

35. Boudart, M. Turnover Rates in Heterogeneous Catalysis. *Chem. Rev*. **1995**, *95* (3), 661-666.

36. Boudart, M. *Kinetics of Heterogeneous Catalytic Reactions*. 1984.

37. Herves, P.; Perez-Lorenzo, M.; Liz-Marzan, L. M.; Dzubiella, J.; Lu, Y.; Ballauff, M. Catalysis by Metallic Nanoparticles in Aqueous Solution: Model Reactions. *Chem. Soc. Rev*. **2012**, *41* (17), 5577-5587.

CHAPTER 3

DIRECT FUNCTIONALIZATION OF DIAMOND NANOPOWDERS[2]

3.1 Introduction

Diamond powders in the micron and nanometer scales have seen a rapid growth in applications apart from use as an efficient abrasive material. Although natural diamond is costly and the purity is highly variable, synthetic diamond is inexpensive and reproducibly manufactured on a large scale, making it an ideal substrate for surface scientists. Synthetic diamond is produced by chemical vapor deposition (CVD), detonation nanodiamond (DND), and high-pressure high-temperature (HPHT) methods. All three synthetic diamond types have been the focus of numerous successful endeavors to modify the surface chemistries and properties in a synergy of surface science and modern organic chemistry techniques.[1]

The appeal of modified diamond surface chemistries lies in the convenience of using familiar organic chemistry and the unparalleled chemical and mechanical stability of diamond in extreme environments.[2] In recent years, numerous successful efforts toward the surface functionalization of CVD and DND have been demonstrated. The Hamers group has done extensive work with CVD diamond surfaces, leading to H-

[2] All experimental work in this chapter was performed by the author with the exception of the following: zeta potential measurements were obtained by David Parker; initiator/HEMA modification and TGA were performed by Megan Bornstein.

terminated surfaces modified by photochemical grafting of organic alkenes with varied chain group properties.[3] Krueger, Shenderova, and others have developed methods for the preparation and surface modification of DND materials with surface functionalities such as hydroxylation, hydrogenation, halogenation, amidation, amination, silanization, and thiolation, to mention a few.[1, 4-13] A number of researchers have shown diamond to be compatible with biological systems.[2-3, 12, 14-18] Commonly, preparation of aminated ND surfaces is proposed as a means to prepare biologically compatible diamond surfaces. Additionally, aminated diamond surfaces have been proposed as attractive surfaces for growth of polymer brush systems because of the high chemical stability, biological compatibility, and diverse surface chemistries available for diamond materials[2]; however, much of this work has been primarily focused on CVD and DND as the substrate. Exploring the utility of these strategies as they relate to HPHT diamond is critical to the development of inexpensive functionalized diamond materials.

The sp^3 hybridized carbon surface of diamond offers a nearly limitless combination of functionalization strategies that have been developed in modern organic chemistry, and refining these methods greatly benefits the development of novel composite materials incorporating diamond. The work presented here demonstrates the successful direct modification of HPHT ND. Surface functionalization was directed by relying on previously published methods for CVD and DND materials.[7, 10, 19-21] Raw HPHT ND powders were hydrogenated using CVD hydrogen treatment followed by acetonitrile attachment through a benzoyl peroxide radical initiated process.[20-22] The surface nitriles were reduced to primary amines using $LiAlH_4$. These primary amines were then coated with an atom transfer radical polymerization (ATRP) polymer radical

initiator followed by growth of the ATRP polymer brushes using 2-hydroxyethyl methacrylate (HEMA) as the monomer unit.[23] The resulting material demonstrates purely covalent attachment of useful chemical moieties such as hydrogen, nitriles, amines, and polymer brushes on HPHT ND surfaces. The importance of this work lies mainly in the expanded application of accepted CVD and DND modification methods to HPHT ND surfaces.

3.2 Materials and Methods

3.2.1 Materials

HPHT diamond (~250 nm, MDP grade) was purchased from Advanced Abrasives. Acetonitrile (ACN, Fisher Scientific, HPLC grade), chloroform (Fisher Scientific, reagent grade), Luperox® A98 benzoyl peroxide ≥98% (BP, Sigma Aldrich), lithium aluminum hydride powder ($LiAlH_4$, Sigma Aldrich), α-bromoisobutyryl bromide (Alfa Aesar), N,N,N′,N″,N″-pentamethyldiethylenetriamine (Sigma Aldrich), and 2-dydroxyethyl methacrylate (HEMA, 98%, Sigma Aldrich) were used without further purification. All water was obtained from a Barnstead NANOPure Diamond Ultrapure water system with the typical resistivity measuring 18.2 MΩ-cm.

3.2.2 Preparation of NH_2-ND

HPHT ND powder (0 – 500 nm as specified by manufacturer, 42 m^2/g) was hydrogenated by heating in a quartz tube furnace at 850 °C for 5 h under 1 atm of H_2 at a flow rate of 3 L/hr.[22] Eight grams of this H-ND was sonicated in 500 mL HPLC grade acetonitrile for 30 min and 1 gram benzoyl peroxide (BP) was added at room temperature with vigorous stirring while dry N_2 was bubbled through the mixture continuously for 40

min.[20] While still bubbling dry N_2, the BP/ACN/ND mixture was heated to reflux for 1 h. The resulting CN-ND was rinsed with copious amounts of acetonitrile followed by chloroform and then redispersed by sonication in 500 mL of dry THF. While purging with dry N_2, 5 grams of $LiAlH_4$ powder was added slowly and the solution was stirred vigorously for 48 h. (Caution: $LiAlH_4$ powder is extremely reactive with moisture. Care must be taken to add this to the THF solution slowly, as $LiAlH_4$ powder will also react vigorously with THF if added rapidly.) While purging with dry N_2 to dilute evolved H_2 gas, concentrated HCl was added dropwise to this mixture until no further reaction was observed. (Caution: Careful control of HCl addition was accomplished using an addition funnel. Rapid addition of concentrated HCl to the $LiAlH_4$ will result in a violent chemical reaction and must be avoided with slow addition of HCl, dry N_2 purging, and extreme precautions, as well as proper personal protective equipment.) After all $LiAlH_4$ had been safely eliminated, rinsing of this mixture with copious amounts of 0.5 M HCl was continued to remove excess Li and Al from the solids. These solids were then rinsed with copious amounts of water and then dried with N_2 to yield NH_2-ND.

3.2.3 Preparation of Initiator-ND

In a round bottom flask, 0.571 g NH_2-ND, 40 mL of freshly distilled CH_2Cl_2, 1 mL anhydrous triethylamine, and a catalytic amount of 4-dimethylaminopyridine were combined and the headspace was flushed with nitrogen before adding 0.4 mL α-bromoisobutyryl bromide; the solution was then stirred at room temperature overnight. Solids were collected by centrifugation and washed in CH_2Cl_2 twice before air drying.

3.2.4 Preparation of HEMA-ND

In a round bottom flask, 0.499 g initiator-ND was mixed with 20 mL MeOH, 13.0 mg $CuCl_2$, 75 µL of ligand N,N,N′,N″,N″-pentamethyldiethylenetriamine, and 5 mL of HEMA with inhibitor removed (via alumina column and 0.45 µm PTFE filter); the mixture was degassed by two freeze-pump-thaw cycles (prior to 2nd thaw, 35 mg of CuCl was added and headspace was filled with nitrogen and capped with a septum). The solution was stirred and heated to 60 °C for 18 h, after which the solids were collected by centrifugation and rinsing with MeOH, 1 M HCl, twice with H_2O, and EtOH to facilitate air drying.

3.2.5 Chemical Vapor Deposition (CVD)

A 20 mL Coors™ combustion boat was filled with raw ND powder and the boats were loaded into a quartz tube furnace (Model OTF-1200X, MTI Corporation) with a trace gas mixer connected to the tube inlet and the outlet connected to a rough vacuum pump for initial purging with hydrogen gas performed 3x.

3.2.6 Diffuse Reflectance Infrared Fourier Transform Spectroscopy (DRIFTS)

DRIFTS samples were prepared with 5%–10 % ND powders diluted in KBr powder (PIKE Technologies). Spectra were collected using a PIKE Technologies DiffusIR accessory fitted to a PerkinElmer Spectrum 100 FTIR instrument with a dry nitrogen purge, and 256 scans were averaged with the resolution set to 4 cm^{-1}.

3.2.7 Thermogravimetric Analysis (TGA)

Measurements were performed on a TA Instruments Hi-Res 2950 with continuous nitrogen purging.

3.2.8 X-Ray Photoelectron Spectroscopy (XPS)

Data were collected using a Kratos Axis Ultra DLD system. Monochromatic Al K-alpha X-rays were used (1486.6 eV), with a power of 150 W (10 mA emission current, 15 kV on the anode). The base pressure in the analysis chamber was 8 X 10^{-10} Torr. All spectra were collected over an analysis area of approximately 300 x 700 microns (as defined by the hybrid/slot settings on the systems lens mode and aperture settings). For high and low resolution spectra, the hemispherical analyzer was operated in FAT (Fixed Analyzer Transmission) mode. Charging artifacts in the spectra were minimized using the system's charge neutralization system. Wide-energy region survey spectra and high-resolution regional spectra were collected using pass energies of 160 eV and 40 eV, respectively.

3.2.9 Zeta Potential

A Malvern Zetasizer Nano ZS was used for analysis of samples prepared at 25 ppm by mass in deionized water. Analysis was performed at 25 °C.

3.3 Results and Discussion

The general synthetic strategy for surface modification of HPHT nanodiamond (ND) is detailed in Figure 3.1. Dry, raw ND powder placed in a ceramic crucible boat was heated in a quartz tube furnace at 850 °C at atmospheric pressure with ultra-high-purity hydrogen flowed at a rate of 3 L/hr. This hydrogenated surface was then modified

by attachment of acetonitrile (ACN) groups when heated to reflux in a reaction flask with thermally initiated benzoyl peroxide radicals, abstracting hydrogens from both the surface of the hydrogenated ND and the methyl group on the ACN molecule. Surface nitriles were then reduced to primary amines using the strong reducing agent $LiAlH_4$. The aminated diamond surface was then modified by attaching a bromine containing polymer brush initiator molecule, α-bromoisobutyryl bromide, which is used specifically to attach to primary amines. Once modified by this initiator molecule, a polymer brush (based on 2-hydroxyehtyl methacrylate (HEMA) chains) can be grown on the ND surface to yield NDs with a hydrophilic polymer thin film.[24]

DRIFTS was used to monitor surface modification progress in the synthetic procedure, illustrated in the reaction scheme of Figure 3.1. DRIFTS spectra of as-received raw ND powders, shown in Figure 3.2, exhibit several characteristic infrared vibrational bands/features at frequencies related to surface oxygen content. Primarily, a broad feature observed at ~3160 cm^{-1} can be attributed to numerous surface hydroxyl groups and the variety of hydrogen bonding interactions among those –OH groups. A strong, sharp absorbance at ~1800 cm^{-1} is assigned to carbonyl groups, with the broadness of the peak originating from the incorporation of these carbonyl groups in several types of environments such as ketones, carboxylic acids, aldehydes, and esters. The last significant peak in the spectrum of raw ND was noted at ~1100 cm^{-1}. This is commonly attributed to sp^3 C-O bonding environments such as those found in surface ND oxygen groups. The presence of these oxygen-containing chemical moieties is consistent with air-oxidized surface sites between sp^3 diamond lattice carbon atoms, as other researchers have observed.[4-5, 11, 22, 25-26]

Dramatic changes in the DRIFTS spectrum after exposure to H_2 at high temperature indicates the formation of hydrogenated ND (H-ND), with negligible absorbance for those regions corresponding to oxygen-containing surface groups seen in raw-ND. The key absorbance of note for H-ND is that of aliphatic sp^3 C-H stretching modes in the 2800–3000 cm^{-1} region.[7, 27-30]

Successful attachment of nitrile groups to H-ND after reacting with ACN and benzoyl peroxide is confirmed in the DRIFTS spectrum of CN-ND by the presence of the characteristic nitrile absorbance at ~2270 cm^{-1}.[20-21] A strong peak at 1727 cm^{-1} assigned as a carbonyl, along with several medium-intensity peaks from aromatic sp^2 C-H stretching, at 3000–3100 cm^{-1}, indicate that the radical initiator, benzoyl peroxide, used to attach ACN has also fragmented into benzoate and phenyl groups that attached to the ND surface. The strong sharp peak at ~1271 cm^{-1} is assigned as the asymmetric CO-O stretch in an ester originating from the benzoate ester attachment.[31] The sharp peaks at ~1000–1150 cm^{-1} are related to C-O bonding environments and indicate benzoyl peroxide fragment attachments to the ND surface. A weak peak at 2112 cm^{-1} is characteristic of isonitrile groups, indicating some unwanted ACN attachment through the nitrogen, –$N^{+}{\equiv}C\text{-}CH_3$.[28] Finally, the structure of the aliphatic C-H stretching region at 2800–3000 cm^{-1} has been altered from H-terminated to CN-ND, corroborating the abstraction of surface –H groups replaced by either ACN or benzoyl peroxide fragments. Attachment of benzyl radicals from the rearrangement of the homolytic cleavage of benzoyl peroxide is confirmed by the presence of aromatic C-H stretching at ~3000–3100 cm^{-1}.[32]

Reduction of the CN-ND to form NH_2-ND via $LiAlH_4$ reduction is mostly inferred from the DRIFTS spectrum of NH_2-ND by noting the absence of characteristic

CN-ND peaks. As a strong reducing agent, $LiAlH_4$ is expected to not only reduce surface nitrile groups to primary amines but also reduce benzoate esters, leading to their elimination from the ND surface. Indeed, the region indicating attachment of nitrile and isonitrile groups, at 2000–2400 cm^{-1}, is featureless. The medium intensity peak at 1690 cm^{-1} and its lower frequency shoulder at 1655 cm^{-1} are expected to be the $–NH_2$ scissoring modes of the attached primary amines. The N-H stretching modes expected at ~3430 cm^{-1} and 3350 cm^{-1} are presumed to be overlapped with the much broader and stronger –OH stretching from surface hydroxyls centered at 3330 cm^{-1} that are presumed to be the result of the benzoate ester reduction. The corresponding C-O modes are observed again at ~1000–1150 cm^{-1}, originating from the same surface-bound hydroxyl groups.

Zeta potential values obtained for ND powders in water provide a good indication of changes in surface charge, as the ND surface is altered with each successive functionalization step. While the nonspherical and multimodal size distribution of ND makes absolute determinations of surface charge difficult, the surface charges for successive functionalization steps were expected to change significantly. Table 3.1 displays zeta potential measurements for water-based solutions of ND powders with different surface functionalization. Apart from the raw-ND, with a zeta potential of -46±6 mV, the ND powders in water do not appear to be very stable as colloids in pH neutral water, with values typically less than ±30 mV. These results compare favorably with other literature values for functionalized ND surfaces, with the zeta potential for raw-ND being large and negative due to oxygen-containing surface groups.[33] Upon hydrogenation, the surface potential reverses by 68 mV, switching sign to 22 ± 5 mV, indicating a substantial change in surface charge. Modification of the hydrogenated

surface with nitrile groups and benzoate esters results in a large change of 50 mV to a value for CN-ND of -28 ± 5 mV. Finally, reduction of the CN-ND surface with $LiAlH_4$ and subsequent neutralization with concentrated HCl reverses the potential by 45 mV, yielding NH_3^+-ND with a surface potential of 17 ± 5 mV. Each synthetic step caused zeta potentials to change dramatically, and the sign reversals for each step are a good indication of the drastic modifications of surface groups observed in the previously discussed DRIFTS results.

Additional evidence to support the conclusion that nitrogen groups were deposited onto the ND surface through the synthetic route outlined in the reaction scheme of Figure 3.1 is available in the XPS spectra shown in Figures 3.3 and 3.4. Figure 3.3 shows XPS spectra in the N 1s energy region for three functionalized ND surfaces: CN-ND, NH_2-ND, and α-bromoisobutyryl bromide modified NH_2-ND. CASA-XPS software peak fitting with the corresponding Shirley background is included as a guide to the eye to augment interpretation of the raw data. Nitrile groups have been observed on silicon surfaces at the same binding energies as the peak observed for CN-ND in Figure 3.3, at 398 eV.[34] This indicates that ACN attachment was successful and that a covalent bond was formed instead of merely physisorption onto the ND surface. Each functionalization step involves copious rinsings with solvent, sonication, and drying. As a result, only direct covalent linkages to the ND surface are expected to persist, leading to the observed N 1s photoelectron peak in not only the CN-ND but also the subsequently reduced surface, NH_2-ND, which exhibits a similar intensity peak at 398 eV. Furthermore, raw-ND surfaces examined with XPS do not yield sufficient photoelectrons at 398 eV for a discernable nitrogen peak to be observed above the background noise. While N 1s XPS

spectra reveal a surface that clearly contains nitrogenous chemical groups, it does not indicate the availability of these nitrogen groups for subsequent bonding. Accessibility must be determined through direct attachment of chemical groups that rely upon the presence of amine groups.

Confirmation of the presence of amines is possible using ATRP methods that depend on successful surface attachment of primary amines. By employing ATRP methods for polymer brush growth on the ND surface, the availability of these reactive surface groups can be revealed. Essentially, the ATRP method we employed consists of two steps: surface attachment of a radical initiator (α-bromoisobutyryl bromide) to the NH_2-ND surface followed by polymer brush growth with HEMA monomers. The initiator molecule will only react with primary amines that are freely accessible. Subsequent growth of the polymer brushes can take place only where initiator molecules are covalently bound to the surface. Intermediate rinsings with copious amounts of solvent in addition to sonication ensure that any noncovalently bound initiator or HEMA is removed, thereby improving our confidence in successful polymer brush growth and in the successful attachment of freely accessible surface amine groups.

Modification of the NH_2-ND surface with initiator does not reduce the surface nitrogen content, as seen in Figure 3.3; however, this fact alone does not confirm the attachment of α-bromoisobutyryl bromide to the NH_2-ND surface. If the initiator has successfully attached to the ND surface, as depicted in the reaction scheme of Figure 3.1, then the tertiary Br on the initiator provides a convenient indicator that α-bromoisobutyryl bromide has indeed covalently bonded to the surface of the NH_2-ND. The X-ray photoelectron spectrum of the region at 67–72 eV for initiator-ND shown in

Figure 3.4 exhibits the spin-orbit split Br 3d photoelectrons that would be indicative of successful initiator attachment.

Thermogravimetric analysis (TGA) is a widely utilized technique in colloid and surface chemistry that allows detection of thin pyrolizable films on nanoparticle surfaces. As shown in Figure 3.5, hydrogenated ND exhibits minimal mass loss upon heating to 800 °C. After attachment of ACN and subsequent reduction by $LiAlH_4$, the NH_2-ND has more nondiamond lattice carbon that can be removed upon heating and shows a mass loss of ~1%. Further functionalization with the radical initiator adds additional pyrolizable material to the ND surface that can be removed with heating, resulting in another ~2.8% mass loss. Finally, with addition of the HEMA polymer thin film the mass loss increase is dramatic, resulting in a further ~15% mass loss.

Further surface functionalization using ATRP routes not only resulted in high fractional mass loss for TGA, but the HEMA layer can also be directly observed using S/TEM imaging, shown in Figure 3.6. The HEMA layer appears to evenly coat all particles and can be seen in the images as a slightly lower contrast area around all of the ND particles. As an aid to the eye, parallel red lines in Figure 3.6 indicate the presence of HEMA layers on the ND.

3.4 Conclusions

Step-by-step surface modification of HPHT ND allows for homogeneous amination and subsequent HEMA polymer brush growth on diamond particles. Successful modification of these HPHT ND particles was confirmed by DRIFTS, zeta potential, XPS, TGA, and S/TEM imaging. Directly functionalized surfaces such as the ones described here are an attractive alternative to silane/silica chemistries. Diamond-

functionalized surfaces offer exceptional chemical stability that might cause dissolution or degradation in other, less-robust materials. Combining directly functionalized ND particles with other compatible materials will allow for the development of novel composite materials. Although a variety of surface modification strategies for ND exist, future development of these materials will rely on efforts like those described here to combine and link modification steps and provide the foundation for materials development based on diamond as a support or scaffolding.

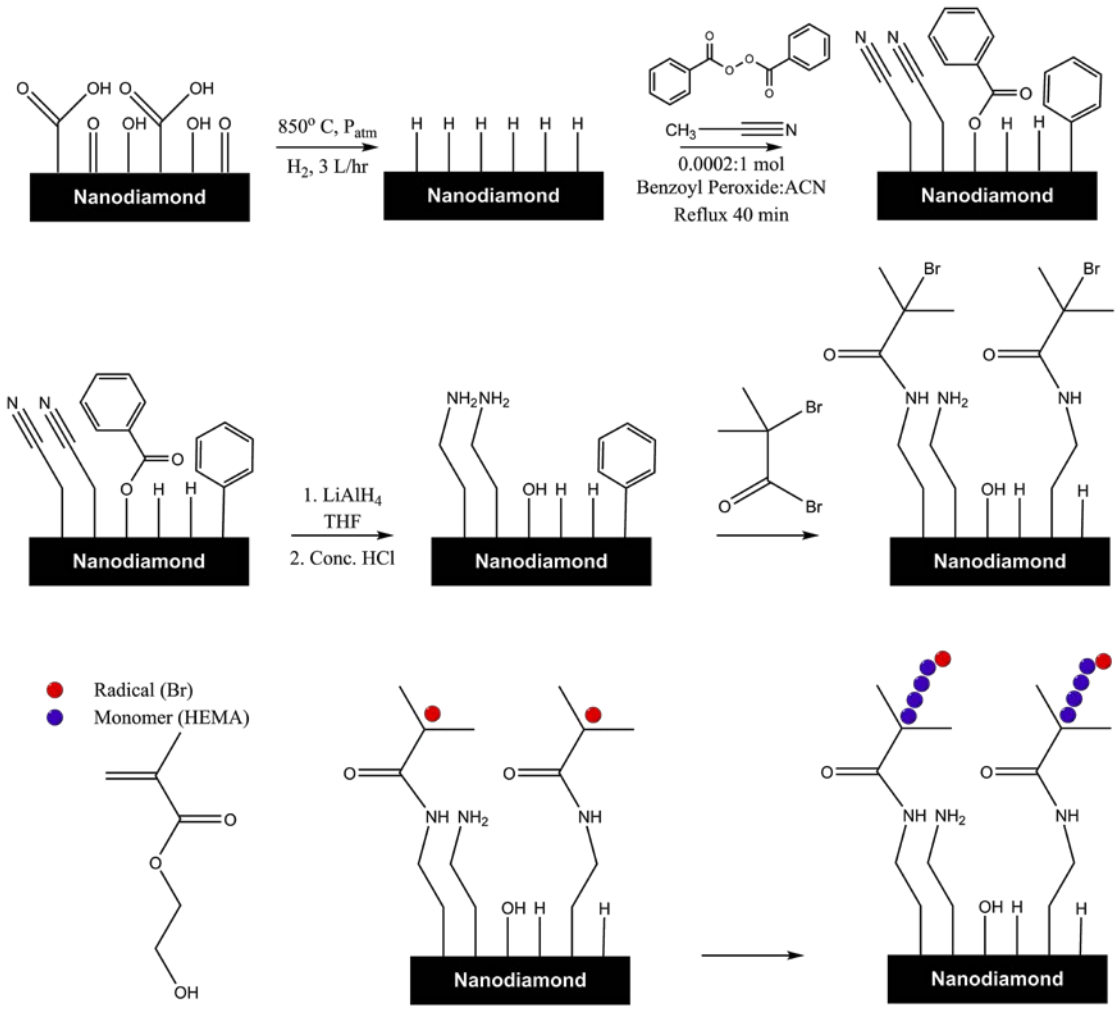

Figure 3.1 Reaction scheme used to functionalize raw ND powders producing HEMA polymer brush coated ND (HEMA-ND).

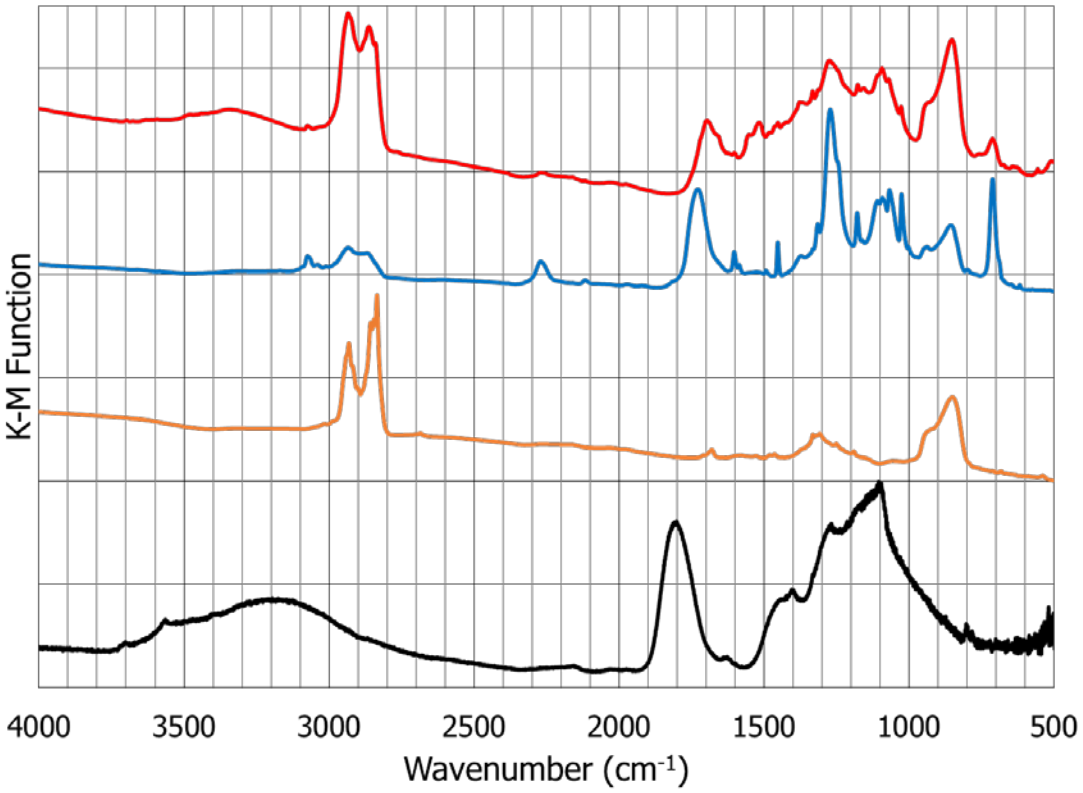

Figure 3.2 DRIFTS spectra of ND powders diluted with KBr: Raw-ND, H-ND, CN-ND, and NH_2-ND.

Note. Key: black = Raw-ND; orange = H-ND; blue = CN-ND; red = NH_2-ND. Spectra were acquired in a nitrogen-purged atmosphere to limit interference from CO_2 and H_2O.

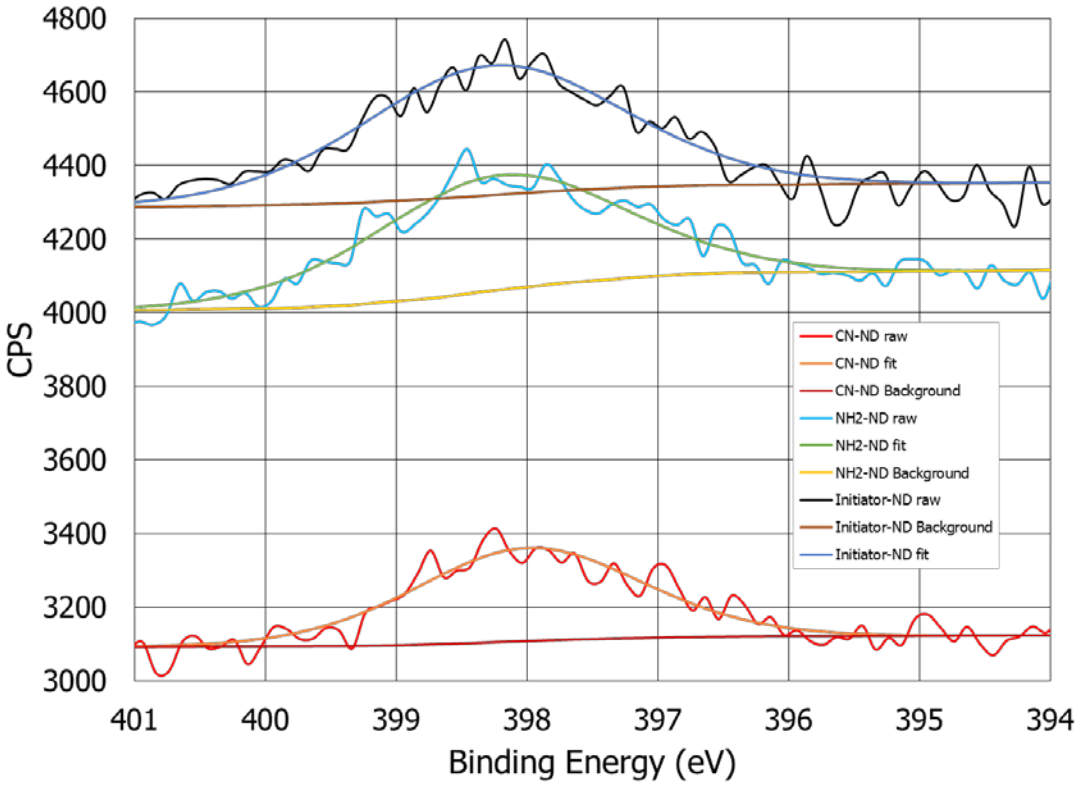

Figure 3.3 XPS N 1s spectra with associated peak fitting for CN-ND, NH_2-ND, and initiator-ND.

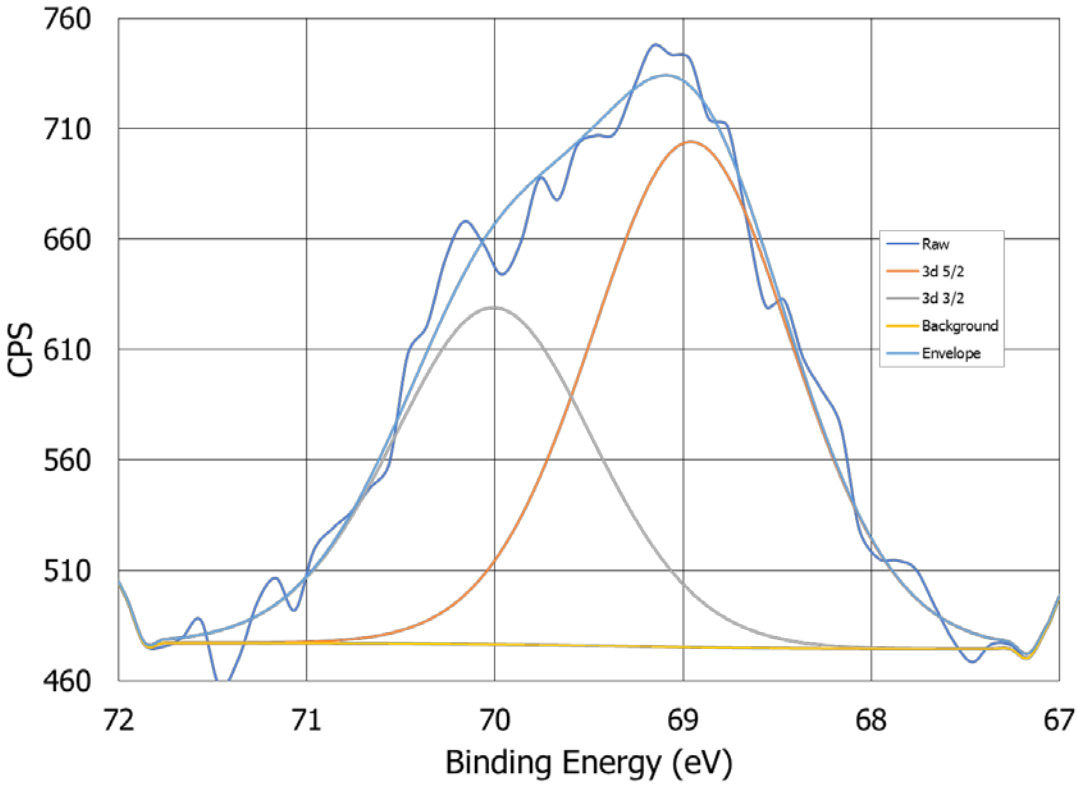

Figure 3.4 XPS Br 3d spectrum with associated peak fitting for initiator, α-bromoisobutyryl bromide, modified NH_2-ND.

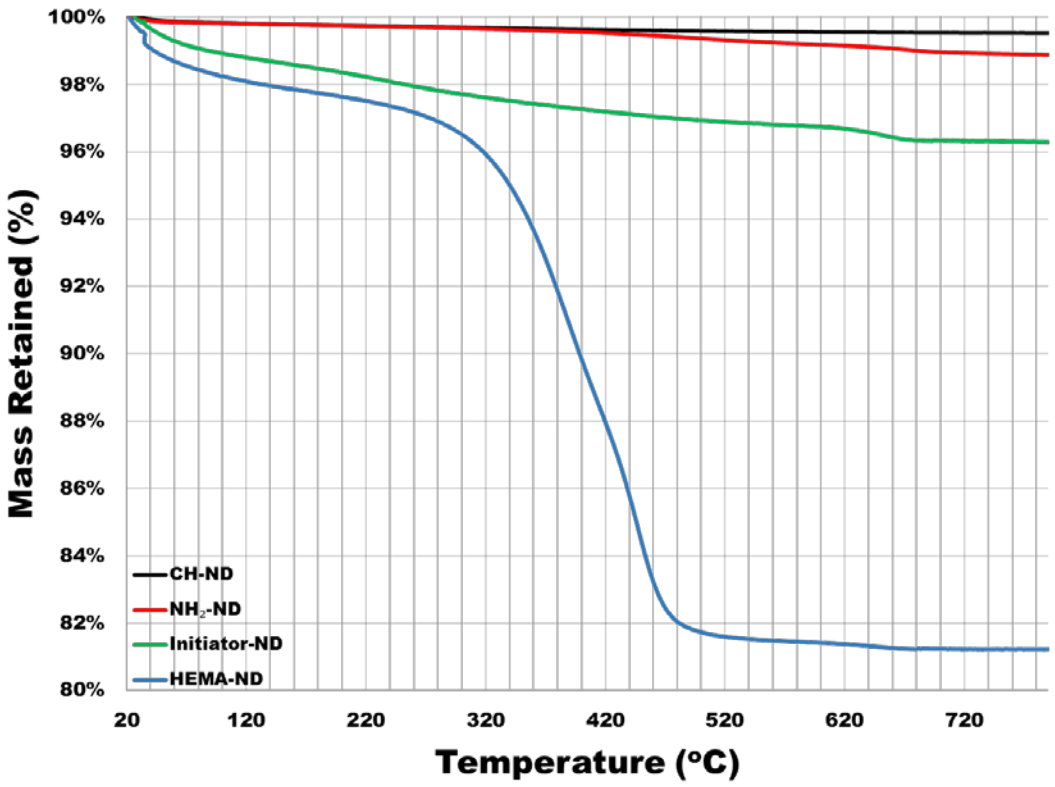

Figure 3.5 TGA mass loss data for H-ND, NH_2-ND, initiator-ND, and HEMA-ND.

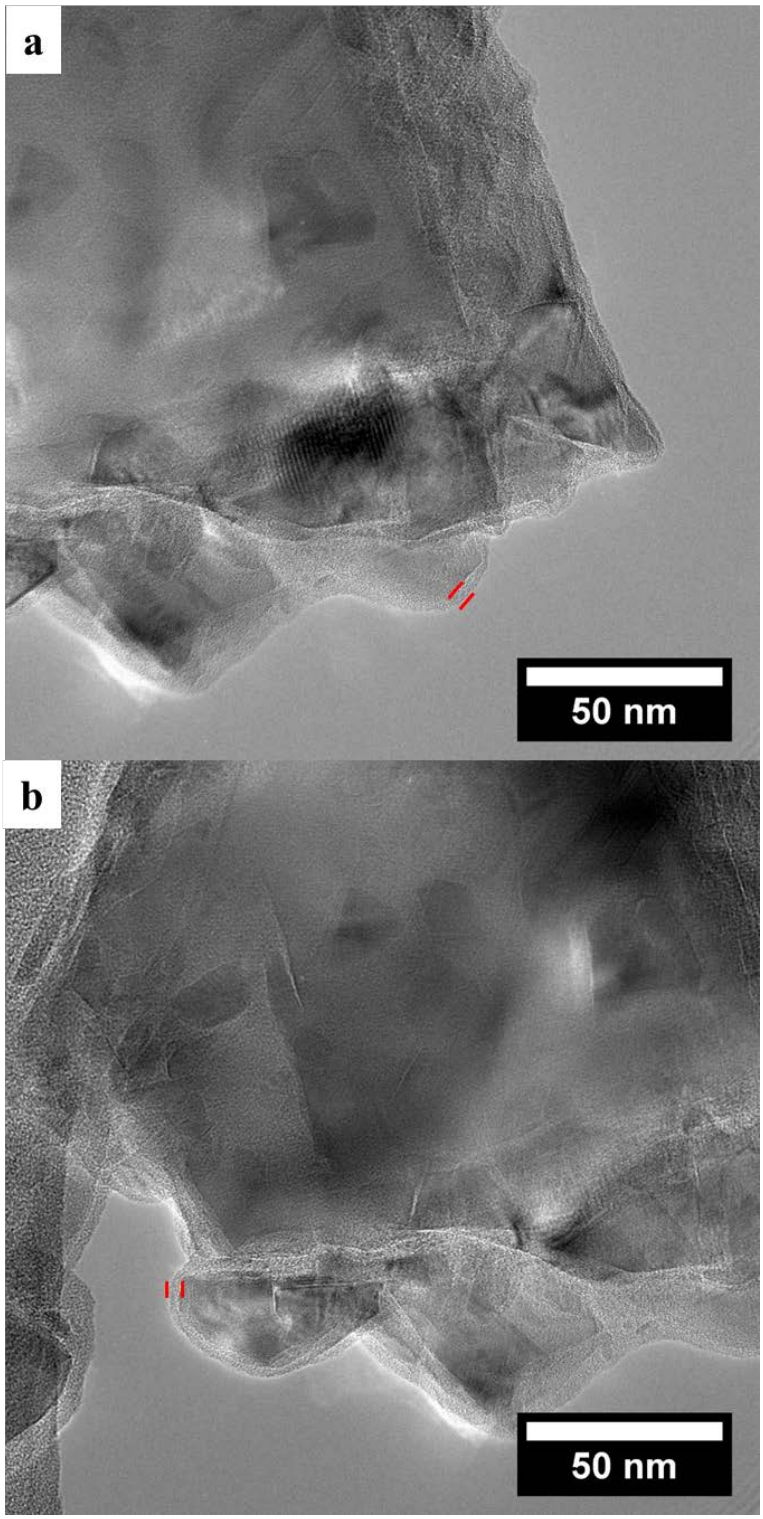

Figure 3.6 S/TEM micrographs of HEMA-ND particles.

Note. The thin, ~10 nm, HEMA coating on the surface of the ND is indicated by parallel red lines.

Table 3.1

Zeta Potential Measurements for Different Surface Functionalizations of ND

ND Material	Zeta Potential, ζ (mV)	σ (mV)
Raw-ND	-46	6
H-ND	22	5
CN-ND	-28	5
NH_2-ND	17	5

3.5 References

1. Nunn, N.; Torelli, M.; McGuire, G.; Shenderova, O. Nanodiamond: A High Impact Nanomaterial. *Curr. Opin. Solid State Mater. Sci.* **2017**, *21* (1), 1-9.

2. Dahoumane, S. A.; Nguyen, M. N.; Thorel, A.; Boudou, J.-P.; Chehimi, M. M.; Mangeney, C. Protein-Functionalized Hairy Diamond Nanoparticles. *Langmuir* **2009,** *25* (17), 9633-9638.

3. Szunerits, S.; Nebel, C. E.; Hamers, R. J. Surface Functionalization and Biological Applications of CVD Diamond. *MRS Bulletin* **2009**, *39* (6), 517-524.

4. Krueger, A.; Lang, D. Functionality Is Key: Recent Progress in the Surface Modification of Nanodiamond. *Adv. Funct. Mater.* **2012,** *22* (5), 890-906.

5. Meinhardt, T.; Lang, D.; Dill, H.; Krueger, A. Pushing the Functionality of Diamond Nanoparticles to New Horizons: Orthogonally Functionalized Nanodiamond Using Click Chemistry. *Adv. Funct. Mater.* **2011,** *21* (3), 494-500.

6. Krueger, A.; Boedeker, T. Deagglomeration and Functionalisation of Detonation Nanodiamond with Long Alkyl Chains. *Diamond Relat. Mater.* **2008,** *17* (7–10), 1367-1370.

7. Girard, H. A.; Petit, T.; Perruchas, S.; Gacoin, T.; Gesset, C.; Arnault, J. C.; Bergonzo, P. Surface Properties of Hydrogenated Nanodiamonds: A Chemical Investigation. *PCCP* **2011,** *13* (24), 11517-11523.

8. Basiuk, E. V.; Santamaría-Bonfil, A.; Meza-Laguna, V.; Gromovoy, T. Y.; Alvares-Zauco, E.; Contreras-Torres, F. F.; Rizo, J.; Zavala, G.; Basiuk, V. A. Solvent-free covalent functionalization of nanodiamond with amines. *Appl. Surf. Sci.* **2013,** *275*, 324-334.

9. Hsu, M.-H.; Chuang, H.; Cheng, F.-Y.; Huang, Y.-P.; Han, C.-C.; Chen, J.-Y.; Huang, S.-C.; Chen, J.-K.; Wu, D.-S.; Chu, H.-L.; Chang, C.-C. Directly Thiolated Modification onto the Surface of Detonation Nanodiamonds. *ACS Appl. Mater. Interfaces* **2014,** *6* (10), 7198-7203.

10. Jarre, G.; Heyer, S.; Memmel, E.; Meinhardt, T.; Krueger, A. Synthesis of Nanodiamond Derivatives Carrying Amino Functions and Quantification by a Modified Kaiser Test. *Beilstein J. Org. Chem.* **2014,** *10*, 2729-2737.

11. Krueger, A. The Structure and Reactivity of Nanoscale Diamond. *J. Mater. Chem.* **2008,** *18* (13), 1485-1492.

12. Krueger, A.; Stegk, J.; Liang, Y.; Lu, L.; Jarre, G. Biotinylated Nanodiamond: Simple and Efficient Functionalization of Detonation Diamond. *Langmuir* **2008,** *24* (8), 4200-4204.

13. Liang, Y.; Ozawa, M.; Krueger, A. A General Procedure to Functionalize Agglomerating Nanoparticles Demonstrated on Nanodiamond. *ACS Nano* **2009,** *3* (8), 2288-2296.

14. Coffinier, Y.; Szunerits, S.; Jama, C.; Desmet, R.; Melnyk, O.; Marcus, B.; Gengembre, L.; Payen, E.; Delabouglise, D.; Boukherroub, R. Peptide Immobilization on Amine-Terminated Boron-Doped Diamond Surfaces. *Langmuir* **2007,** *23* (8), 4494-4497.

15. Hens, S. C.; Cunningham, G.; Tyler, T.; Moseenkov, S.; Kuznetsov, V.; Shenderova, O. Nanodiamond Bioconjugate Probes and Their Collection by Electrophoresis. *Diamond Relat. Mater.* **2008,** *17* (11), 1858-1866.

16. Nebel, C. E.; Shin, D.; Rezek, B.; Tokuda, N.; Uetsuka, H.; Watanabe, H. Diamond and Biology. *J. R. Soc. Interface* **2007,** *4* (14), 439-461.

17. Yang, W.; Auciello, O.; Butler, J. E.; Cai, W.; Carlisle, J. A.; Gerbi, J. E.; Gruen, D. M.; Knickerbocker, T.; Lasseter, T. L.; Russell, J. N.; Smith, L. M.; Hamers, R. J. DNA-Modified Nanocrystalline Diamond Thin-Films as Stable, Biologically Active Substrates. *Nat. Mater.* **2002,** *1* (4), 253-257.

18. Zhang, G.-J.; Song, K.-S.; Nakamura, Y.; Ueno, T.; Funatsu, T.; Ohdomari, I.; Kawarada, H. DNA Micropatterning on Polycrystalline Diamond Via One-Step Direct Amination. *Langmuir* **2006,** *22* (8), 3728-3734.

19. Girard, H. A.; Arnault, J. C.; Perruchas, S.; Saada, S.; Gacoin, T.; Boilot, J. P.; Bergonzo, P. Hydrogenation of Nanodiamonds Using MPCVD: A New Route Toward Organic Functionalization. *Diamond Relat. Mater.* **2010,** *19* (7–9), 1117-1123.

20. Tsubota, T.; Hirabayashi, O.; Ida, S.; Nagaoka, S.; Nagata, M.; Matsumoto, Y. Chemical Modification of Hydrogenated Diamond Surface Using Benzoyl Peroxides. *PCCP* **2002,** *4* (5), 806-811.

21. Tsubota, T.; Ida, S.; Hirabayashi, O.; Nagaoka, S.; Nagata, M.; Matsumoto, Y. Chemical Modification of Diamond Surface Using a Diacyl Peroxide as Radical Initiator and CN Group-Containing Compounds for the Introduction of the CN Group. *PCCP* **2002,** *4* (15), 3881-3886.

22. Spitsyn, B. V.; Davidson, J. L.; Gradoboev, M. N.; Galushko, T. B.; Serebryakova, N. V.; Karpukhina, T. A.; Kulakova, I. I.; Melnik, N. N. Inroad to Modification of Detonation Nanodiamond. *Diamond Relat. Mater.* **2006,** *15* (2–3), 296-299.

23. Khabibullin, A.; Fullwood, E.; Kolbay, P.; Zharov, I. Reversible Assembly of Tunable Nanoporous Materials from “Hairy” Silica Nanoparticles. *ACS Appl. Mater. Interfaces* **2014,** *6* (19), 17306-17312.

24. Matyjaszewski, K.; Xia, J. Atom Transfer Radical Polymerization. *Chem. Rev.* **2001,**

101 (9), 2921-2990.

25. Singh, B.; Smith, S. J.; Jensen, D. S.; Jones, H. F.; Dadson, A. E.; Farnsworth, P. B.; Vanfleet, R.; Farrer, J. K.; Linford, M. R. Multi-Instrument Characterization of Five Nanodiamond Samples: A Thorough Example of Nanomaterial Characterization. *Anal. Bioanal. Chem.* **2016,** *408* (4), 1107-1124.

26. Mochalin, V. N.; Shenderova, O.; Ho, D.; Gogotsi, Y. The Properties and Applications of Nanodiamonds. *Nat. Nano.* **2012,** *7* (1), 11-23.

27. Silverstein, R. M.; Webster, F. X.; Kiemle, D.; Bryce, D. L. *Spectrometric Identification of Organic Compounds*. John Wiley & Sons: 2014; pp 118-125.

28. Pretsch, E.; Bühlmann, P.; Affolter, C.; Pretsch, E.; Bhuhlmann, P.; Affolter, C. *Structure Determination of Organic Compounds*. Springer: 2009; Vol. 13, pp 269-335.

29. Manfredotti, C.; Bonino, P.; De La Pierre, M.; Vittone, E.; Manfredotti, C. About Orientation Dependence of Physico-Chemical Properties of HPHT Diamond Surfaces Thermally Treated in H2 and D2 Environments. *Diamond Relat. Mater.* **2010,** *19* (4), 279-283.

30. Ando, T.; Ishii, M.; Kamo, M.; Sato, Y. Thermal Hydrogenation of Diamond Surfaces Studied by Diffuse Reflectance Fourier-Transform Infrared, Temperature-Programmed Desorption and Laser Raman Spectroscopy. *J. Chem. Soc., Faraday Trans.* **1993,** *89* (11), 1783-1789.

31. Chateauneuf, J.; Lusztyk, J.; Ingold, K. U. Spectroscopic and Kinetic Characteristics of Aroyloxyl Radicals. 2. Benzoyloxyl and Ring-Substituted Aroyloxyl Radicals. *J. Am. Chem. Soc.* **1988,** *110* (9), 2886-2893.

32. Gao, G.; Liu, D.; Tang, S.; Huang, C.; He, M.; Guo, Y.; Sun, X.; Gao, B. Heat-Initiated Chemical Functionalization of Graphene. *Scientific Reports* **2016,** *6*, 20034.

33. Williams, O. A.; Hees, J.; Dieker, C.; Jäger, W.; Kirste, L.; Nebel, C. E. Size-Dependent Reactivity of Diamond Nanoparticles. *ACS Nano.* **2010,** *4* (8), 4824-4830.

34. Schwartz, M. P.; Hamers, R. J. Reaction of Acetonitrile with the Silicon(0 0 1) Surface: A Combined XPS and FTIR Study. *Surf. Sci.* **2007,** *601* (4), 945-953.

CHAPTER 4

ROBUST POLYMER-COATED NANODIAMOND SUPPORTS FOR NOBLE METAL NANOPARTICLE CATALYSTS[3]

4.1 Introduction

Ultra-small noble metal nanoparticles (NPs) have become a central topic in nanoscience and catalysis due to the significant differences between the properties of NPs compared to bulk metals.[1] One material exhibiting this behavior is gold, which is inert as a bulk material, yet when prepared as ultra-small NPs displays remarkable catalytic activity. Since Haruta's work in the 1980s,[2] gold nanoparticles (AuNPs) have been shown to catalyze a variety of reactions, including oxidations, reductions, and carbon–carbon bond formation.[3-5]

Because of the importance of active site availability in heterogeneous catalysis, prevention of particle aggregation is essential to maintaining catalytic efficiency.[6] During catalytic reactions, reactants compete for active surface sites, potentially displacing ligands and eventually leading to unstable high-energy surface sites. This, in turn, causes particle aggregation, reduces catalytic activity, and limits reusability.[7-8] One approach

[3] Reproduced as published, with permission. Quast, A.D.; Bornstein, M.; Greydanus, B.J.; Zharov, I.; Shumaker-Parry, J.S. Robust Polymer-Coated Nanodiamond Supports for Noble Metal Nanoparticle Catalysts. *ACS Catalysis, 6*, 2016, 4729–4738, Copyright 2016 American Chemical Society. The first author conducted all experimental and characterization work with the exception of FTIR analysis performed by B.J.G. An AVI file showing a tilt-series TEM image sequence is available free of charge on the ACS Publications website at DOI:10.1021/acscatal.6b01243.

used to prevent NP aggregation involves the use of a support material that can be a co-catalyst or simply provide mechanical stability during catalytic cycles.[9-27] Porous and nonporous silica have been widely used because of the ease of modification of the silica surface with mercapto or amino functionalities, which serve as anchor groups for NP attachment.[27] However, the stability of silica-based materials is compromised in some chemical environments, such as high or low pH solutions, leading to nanoparticle aggregation and dissolution of the silica support material.[28-29] Polymer-supported AuNPs are attractive because in aqueous media they offer significant stability not available with silica supports[27]; however, many reactions require the use of organic solvents where polymeric supports such as polystyrene swell and dissolve.[5]

In an effort to address the stability challenges of metal nanoparticles and develop a versatile and robust catalytic platform, we investigated a polymer-diamond composite material that we expected to offer high mechanical and chemical stability in diverse environments. By coating synthetic diamond particles with a thin polymer adhesion layer, a scaffold was formed for high surface density deposition of ultra-small metal NPs with high catalytic activity. The polymer-diamond support exhibited enhanced stability compared to silica particle supports, offering access to reactions and conditions that were previously limited by support-material stability and reaction-environment incompatibility.

4.2 Materials and Methods

4.2.1 Reagents

Pentaerythritol tetra(3-mercaptopropionate) (PETMP), triallyl-1,3,5-triazine-2,4,6-trione (TATATO), 2,2-dimethoxy-2-phenylacetophenone (DMPA), N-3-

dimethylaminopropyl)-N'-ethylcarbodiimide HCl (EDAC), pentafluorophenol (PFP), triethylphosphine gold (I) chloride, chloroplatinic acid hydrate, bis(triphenylphosphine)palladium(II) dichloride, triphenylphosphine (TPP), sodium borohydride ($NaBH_4$), 4-nitrophenol (PNP), 0.5 M THF solution of 9-Borabicyclo[3.3.1]nonane (9-BBN), and isopropanol (IPA) were obtained from Sigma-Aldrich. N-(3-Aminophropyl)methacrylamide hydrochloride, >98% (APMAA) and 2-aminoethyl methacrylate hydrochloride, 95% (AEMA) were purchased from Polysciences, Inc. Reagent grade acetonitrile (ACN), methylene chloride, chloroform, hexanes, toluene, and acetone were purchased from Fisher Scientific. Ethyl alcohol (200 proof) was purchased from Decon Labs. Methanol was purchased from Omni Solve. (3-Mercaptopropyl)trimethoxysilane (MCPTMS), 95% was purchased from Alfa Aesar. Rhodamine B, 98% was purchased from Acros Organics. Dansyl chloride ≥99.0 was purchased from Fluka. Aqueous solutions of 10% monocrystalline diamond powder (MDP(N)) produced by the belt-type press method using a nickel/iron catalyst were purchased from Advanced Abrasives Corp. All water used was obtained from a Barnstead Diamond Nanopure system with a resistivity ≥18.0 MΩ·cm. All reagents were used without further filtration or purification. For TEM imaging, copper formvar/carbon grids (200 mesh) were acquired from Electron Microscopy Sciences.

4.2.2 Preparation of Polymer-Coated Diamond-Supported AuNPs

The following reagents were mixed vigorously and added in the order listed to prevent premature polymerization from uninhibited monomers. Approximately 0.2 g of 0.25 μm MDP diamond (2 g of 10% diamond solution in water as provided by the manufacturer) was mixed with the following: 2.8 g ACN, 5.8 g water, 0.0002 g Et_3AuCl,

0.04 g PETMP, 0.08 g TATATO, 0.014 g APMAA or AEMA, and 0.00537 g DMPA. The combined solution was mixed vigorously for at least 30 min prior to exposure to UV light. The mixture was then exposed to a UV lamp for 1 h while mixing; it was then centrifuged and the solid was rinsed with copious volumes of IPA and ACN. The resulting solids were then mixed with 5.0 mL of 0.130 molal Et_3PAuCl in ACN overnight. While mixing, over the course of 10 min, 10 drops of an aqueous 0.1 M $NaBH_4$ solution was added and the solution was allowed to continue mixing for >24 h. The resulting solids were then rinsed with copious amounts of H_2O and IPA and then stored in IPA. The amount of Et_3PAuCl was increased or decreased to obtain the desired catalyst loading and the same method was used for equimolar solutions of Pt and Pd salts. APMAA and/or AEMA were included only if primary amines were to be incorporated into the polymer coating.

4.2.3 UV Irradiation

Curing solutions were stirred at an approximate distance of five inches from a 15-Watt Ultra Violet Products (UVP) XX-15S 254nm benchtop lamp.

4.2.4 PNP Reduction Conditions for Polymer/ ND-Supported Materials

When testing the catalytic efficiencies of composite materials, $6.54x10^{-5}$, $6.82x10^{-5}$, and $6.89x10^{-5}$ g of the Au, Pd, or Pt/polymer/ND materials were used, where the mass % metals content was 23.7, 0.75, and 1.14%, respectively. These materials were combined with water so that the final concentrations of the aqueous mixtures were 3 μM 4-NP and 3 mM $NaBH_4$ (at least 1000x molar excess of $NaBH_4$).

4.2.5 Synthesis of TPP-AuNPs

In a mixture of acetonitrile and toluene (10:40 mL), 0.017 g (0.05 mmol) of chloro(triethylphosphine)gold(I) (Et_3PAuCl) was dissolved. TPP (0.0786 g, 0.3 mmol) was added to the mixture at room temperature. The contents were stirred for 30 min, after which 0.4 mL of 9-BBN (0.2 mmol) was injected into the mixture. After an additional 30 min of stirring, a solid appeared. The reaction mixture was centrifuged and the solid was collected. The solid was then washed twice with hexane to remove any impurities. After drying by nitrogen flow, a black solid was obtained. The black solid was dissolved in nanopure water (>18 MQ) and the mixture was sonicated in a Branson ultrasonic cleaner. The solution was centrifuged and the small aggregates at the bottom of the tube were discarded. The supernatant was centrifuged two more times and the final solution was used as the stock TPP AuNP solution in the catalysis investigations discussed below.

4.2.6 Preparation of Silica-Supported AuNPs

Roughly 1.2 g of 250 nm silica spheres, produced according to the Stöber method, were treated with fresh 100 °C piranha solution overnight.[30] The silica was then washed with copious amounts of water and ACN, then dried with nitrogen. The cleaned and dried silica was added to a solution of 40 mL ACN, to which ~1 mL of MCPTMS was added. The mixture was stirred for 48 h, after which the silica was washed with copious amounts of ACN. The MCPTMS-coated silica was then added to 5 mL of TPP stabilized AuNPs (2.4 µM Au in H_2O) and the solution was stirred for 24 h and then rinsed thoroughly with ACN .[31]

4.2.7 Preparation of Bare Diamond-Supported AuNPs

In an Erlenmeyer flask, 2.2 g of 0.25 μm MDP diamond solution (6.21% in H_2O) was added to 4.9 g of Au/ACN mix (0.071 molal Et_3PAuCl in ACN) and stirred for at least 30 min after which a five-fold mol excess (with respect to moles of Au salt) of $NaBH_4$ in 5 mL H_2O was added dropwise and allowed to continue mixing for 30 min before rinsing with ACN and H_2O and then drying with nitrogen.

4.2.8 Thermogravimetric Analysis (TGA)

Measurements were performed on a TA Instruments Hi-Res TGA 2950 thermogravimetric analyzer.

4.2.9 Fluorescent Tagging and Imaging

Attachment of rhodamine B and dansyl chloride were performed according to previously published methods and the same AuNP/polymer/ND materials described above.[32-34] Fluorimetry spectra were acquired using a Hitachi F-7000 fluorescence spectrophotometer. Fluorescence images were collected using an Olympus BX40 fluorescence microscope with a Photometrics CoolSNAPcf color camera made by Roper Scientific. The excitation/emission filter set was 557/571 nm and the acquisition time was 0.01 s.

4.2.10 X-Ray Photoelectron Spectroscopy (XPS)

Data were collected using a Kratos Axis Ultra DLD system. Monochromatic Al K-alpha X-rays were used (1486.6 eV), with a power of 150 W (10 mA emission current, 15 kV on the anode). The base pressure in the analysis chamber was 8 X 10^{-10} Torr. All spectra were collected over an analysis area of approximately 300 x 700 microns (as

defined by the hybrid/slot settings on the system's lens mode and aperture settings). For high and low resolution spectra, the hemispherical analyzer was operated in FAT (fixed analyzer transmission) mode. Charging artifacts in the spectra were minimized using the system's charge-neutralizations system. Wide-energy region survey spectra and high-resolution regional spectra were collected using pass energies of 160 eV and 40 eV, respectively.

4.2.11 Diffuse Reflectance Infrared Fourier Transform Spectroscopy (DRIFTS)

A PIKE Technologies DiffusIR accessory was attached to a Perkin-Elmer Spectrum 100 FTIR for DRIFTS data collection. Powdered samples were diluted with KBr powder and spectra were acquired by averaging 64 scans with the resolution set to 4 cm^{-1}.

4.2.12 UV-Visible Spectroscopy

Using a Perkin-Elmer Lambda 750 UV/Vis/NIR spectrophotometer, absorbance measurements at 400 nm were collected in time scan mode at intervals of 0.2s and a bandwidth of 4nm.

4.2.13 Transmission Electron Microscopy (TEM)

TEM images were collected using a JEOL 1400 plus with an accelerating potential of 120 kV and a LaB_6 thermionic source. Determination of particle diameters was limited due to the irregularity and thickness of the diamond supports. Consequently, the EM images exhibited large changes in contrast. This made flat-field correction of the images difficult, and as a result, particle counts were lower than desirable. Manual

determination of particle diameters resulted in greatly reduced uncertainties when compared to image software particle analysis. Single-axis tilt images were obtained using automated EM data acquisition with SerialEM software, with 1° changes between images for a total of 116°. The series of images was then processed to correct alignment errors using IMOD 4.7. The AuNPs/polymer/ND composite seen in the AVI file is the same material as that used in Figure 4.1 A, B.

4.2.14 Scanning Transmission Electron Microscopy (S/TEM)

A JEOL 2800 S/TEM operating at an accelerating potential of 200 kV with a hot field emission gun (FEG) source and equipped with an ultrafast energy dispersive spectrometer was used to collect secondary electron as well as bright and high angular annular dark field (HAADF) images, with a probe size of 1.5 nm and a camera length corresponding to a detector semi-angle of 62.1 milliradians. The dual EDS detectors, with a total area of 100 mm^2, have a combined solid angle collection efficiency of 1.9 steradians.

4.2.15 Inductively Coupled Plasma-Optical Emission Spectroscopy (ICP-OES)

A Thermo Scientific iCAP 6000 series ICP spectrometer was used for elemental analysis. Samples were digested with freshly prepared hot aqua regia using concentrated TraceSELECT® HNO_3 and HCl obtained from Sigma-Aldrich. Standard solutions were prepared using 1000 ppm metal standards obtained from Inorganic Ventures.

4.2.16 BET Surface Area Analysis

A Micromeritics ASAP-2020 analyzer was used to measure BET surface area by nitrogen adsorption and desorption isotherms at -195.6 °C after the sample was degassed in vacuum at 250 °C for 3 h.

4.3 Results and Discussion

Nanodiamond (ND) offers chemically and mechanically robust nanoparticles with reactive functional groups at their surface. We used these surface groups to anchor a thin polymer layer with the intention of creating a scaffold for immobilization of metal nanoparticles. Recent studies of ND particles indicate that sp^2 carbon atoms in a graphitic shell cover the core sp^3 carbon atoms inside the particles. The surface of the ND particles contains such functionalities as vinyl, hydroxyl, and carboxylic acid groups that can be modified under a variety of conditions.[35] For example, Hamers *et al.* have shown thiol-ene chemistry to be suitable for chemical modification of ND surfaces.[36-37] Separately, Dickey *et al.* demonstrated the effectiveness of thiol-ene polymers for gold adhesion.[38]

Thus, we used thiol-ene chemistry for both attachment of a polymer film to nanodiamond and subsequent immobilization of noble metal nanoparticles. In this process, a photo-initiator 2,2-dimethoxy-2-phenylacetophenone (DMPA) was exposed to UV light at 254 nm, generating free radicals that cleave the S-H bonds in pentaerythritol tetra(3-mercaptopropionate), PETMP, which then combine with vinyl monomers present in solution and with the double bonds present on the ND surface (Figure 4.2).[38] Although triallyl-1,3,5-triazine-2,4,6-trione (TATATO) monomer is commonly used for this purpose, we also experimented with incorporating primary amine groups using 2-aminoethyl methacrylate (AEMA) and/or N-(3-aminopropyl)methacrylamide (APMAA)

monomers.[36-37, 39-42] A proposed mechanism for this polymerization process is shown in the reaction scheme of Figure 4.2.

Photoinitiated radical polymerization of thiol-ene polymers onto the surface of ND is likely a complex process involving several steps. Although there are numerous possible routes for this polymerization process, we propose one possible pathway, as shown in Figure 4.3. First, UV irradiation cleaves the photonitiator, 2,2-dimethoxy-2-phenylacetophenone (DMPA), into two radicals. These radicals abstract a hydrogen to produce sulfur radicals from the tetra thiol monomer, pentaerythritol tetra(3-mercaptopropionate) (PETMP). These sulfur radicals propagate the polymerization by reacting with alkene groups of triallyl-1,3,5-triazine-2,4,6-trione (TATATO), 2-aminoethyl methacrylate hydrochloride (AEMA) and/or N-(3-aminopropyl)methacrylamide (APMAA). The numerous possible combinations of the propagation steps based on the molecules in the reaction scheme of Figure 4.3 allow for the formation of multiple cross-links. Additional complexity may result from termination steps in which two free radicals combine between monomers or with the reactive groups on the surface of the diamond particles.

Initially, we attempted the polymerization on the surface of NDs and planned to follow this with the immobilization of metal NPs; however, the resulting composite material was highly inhomogeneous, with most of the NDs being either sparsely covered with metal NPs or completely lacking any surface-bound NPs. Additionally, polymer films did not possess consistent thickness or surface coverage. ND particles were either not coated with polymer or large polymer masses were found to encase many NDs. These observations led us to modify our preparation methods in an effort to achieve a more

homogeneous mixture of metal NPs, polymer, and ND. We discovered that when the metal NP precursor salts were present in the reaction mixture, more uniform polymeric films were formed on the ND surface. As a result, this became our approach to prepare the metal particle catalysts on the polymer-coated ND. Future studies will aim to elucidate the mechanisms involved and the role of the metal salts, but this is beyond the scope of this report.

Upon treatment with sodium borohydride ($NaBH_4$), gold (Au), platinum (Pt), and palladium (Pd), NPs immobilized on the surface of the polymer-coated NDs were formed. Figure 4.1 shows TEM images of Au, Pt, and Pd NPs on polymer-coated ND supports. The roughly 200 nm ND particles appear to form large agglomerates; however, this aggregation is mainly due to the drying process in TEM sample preparation. These agglomerates are easily dispersed in solution using ultrasonication. A closer inspection of these NDs (Figure 4.1 b) shows AuNPs with a diameter of ~3 nm on the polymer/diamond surface. As seen in Figure 4.1 b, the AuNPs follow the contour of the diamond support closely, suggesting that the polymer adhesion layer is thin.

In addition to Au, *in situ* particle growth worked for the formation of Pt and Pd NPs, as can be seen in Figure 4.1 C–D. The ability to incorporate different metals demonstrates the versatility of the polymer/diamond composite as a support material. Several factors were found to influence the NP growth: the concentration of $NaBH_4$ added to the metal salt seeded polymer/NDs, the rate at which the $NaBH_4$ was added to the mixture, the concentration of metal salt, and the temperature of the mixture at the time of NP growth. Although we do not discuss the optimization of these parameters here, the final conditions used for preparation of the materials are described in detail in

the Materials and Methods section.

The presence of the polymer layer on the surface of NDs was confirmed by thermogravimetric analysis (TGA, Figure 4.4), which showed a mass fraction of the polymer in the NP/polymer/NDs of 0.4 for AuNPs and of 0.1 for Pt and Pd NPs. We used the following relationship to covert the mass fraction to an average polymer thickness

$$P_{thick} = \frac{m_p S_d}{\rho_p} \tag{4.1}$$

where P_{thick} (nm) is the polymer thickness, m_p (unitless) is the mass fraction of polymer per gram of diamond, S_d (nm^2/g) is the surface area of the ND, and ρ_p (g/nm^3) is the density of the polymer. Using an average polymer density of 1.2 g/cm^3 (1.28 g/cm^3 for PETMP and 1.1590 g/cm^3 for TATATO), ND density of 3.513 g/cm^3, and Brunauer-Emmett-Teller (BET) specific surface area for ND of 19.5 m^2/g, the thickness of the polymer films can be estimated as ~29 nm for the Au/polymer/ND and ~5 nm for the Pt/polymer/ND and Pd/polymer/ND. Although TEM is capable of sub-nm resolution, the polymer adhesion layer is not visible in the TEM images shown in Figure 4.1. This is likely the result of drying and shrinking of the polymer in the high-vacuum environment of the TEM, as well as the low polymer density.

The presence and composition of the polymer layer were also confirmed by DRIFTS. The spectrum for the bare NDs is smooth and featureless, as expected, while the principle monomers have several identifying features above 1500 cm^{-1} in addition to those in the fingerprint region (Figure 4.5 a), such as carbonyl peaks characteristic of the PETMP and TATATO monomers at 1738 cm^{-1} and 1688 cm^{-1}, respectively. These same carbonyl peaks are observed in the composite particles (Figure 4.5 b), indicating that the

PETMP and TATATO were incorporated into the polymer. Furthermore, because the molar ratio of PETMP:TATATO is 3:4, the carbonyl peaks in the DRIFTS spectra of polymer/NDs have similar intensities. Other characteristic peaks are located at 3085 cm^{-1} (weak), 1466 cm^{-1} (strong, sharp), and 765 cm^{-1} (sharp) in the IR spectra of the composite particles and in the IR spectrum of pure PETMP. The thiol peak at 2600 cm^{-1} is well resolved in the spectrum of pure PETMP but not in the spectra of the composite particles. The absence of the S-H vibrational mode in the composite particles could be due to the oxidation of sulfur, bonding to metal clusters, and/or low concentration; however, the thiol region is typically very weak in materials that contain S-H bonds, and its absence is not unexpected.[43-44] Finally, three peaks centered at 1185 cm^{-1} are present in the composite particles as well as the IR spectrum of pure TATATO.

X-ray photoelectron spectroscopy (XPS) analysis confirmed the presence of the metal NPs observed in the TEM images. The XPS spectra (Figure 4.6 A–C) also demonstrated that the metal NPs are localized on the surface of the polymer coating because the Au 4f, Pt 4f, and Pd 3d regions are clearly observable and XPS is most sensitive to the composition in the top few nanometers of the surface.[45] If the metal NPs were embedded inside polymer layers that were 5–29 nm thick, then the metal photoelectrons would be completely blocked. The peak shapes and positions of both Au $4f_{7/2}$ (84 eV) and Pt $4f_{7/2}$ (71 eV) seem to indicate that most of these atoms are in the Au(0) and Pt(0) state. However, the location and peak shape of Pd $3d_{5/2}$ indicates that the PdNPs/polymer/ND material is mostly decorated with Pd(II) (337 eV) and that Pd(0) (335 eV) is much less abundant. This difference between the abundance of oxidation states for Au and Pt vs Pd is likely a result of several factors: oxide formation, Pd-S

bonding, and incomplete reduction of the precursor Pd salt.[46] TEM images unambiguously confirm the presence of PdNPs; however, Pd is also easily oxidized and this oxidation may have contributed to an increase in the relative abundance of Pd(II) vs Pd(0) between the preparation of the PdNPs/polymer/ND material and subsequent XPS analysis. The presence of the polymer on the ND surface was confirmed by S 2p peaks in the XPS spectra (Figure 4.6 D). The lower intensity of the peaks observed for sulfur compared to that of metal NPs is an indication that the polymer adhesion layer is likely a significantly smaller fraction of the total mass of the composite particles.

High-angle annular dark field-S/TEM (HAADF) was used to study the distribution of the metal NPs on the surface of the composite material (Figure 4.7 A, C, E). As Pennycook *et al.* have shown previously,[47] HAADF images are formed using high-angle incoherent Rutherford scattered electrons. As the number of protons (Z-number) increases, the scattering cross-sections increase as Z^2. As a result, the HAADF technique is particularly suitable for obtaining images of NP/polymer/ND particles. Indeed, Au, Pt, and Pd atoms appear nearly 173×, 169×, and 58× brighter than carbon atoms in the polymer or diamond support, respectively.[48] Although Figure 4.6 reveals that 4.5 ± 0.8 nm (N = 101) AuNPs are more easily discernable than the dimmer 1.2 ± 0.3 nm (N = 40) PtNPs or the 1.5 ± 0.2 nm (N = 62) PdNPs, this difference in contrast most likely results from the significant difference in cluster size. The larger AuNPs contain approximately 2,600 atoms while average PtNPs and the PdNPs are estimated to contain only ~60 and ~100 atoms, respectively. Another interesting observation is that PtNPs not only coated the surface of the polymer/diamond surface as individual clusters, but also as larger, loosely packed agglomerates of 18 ± 3 nm (N = 14).

Secondary-electron imaging (SEI)-S/TEM images (Figure 4.7 B, D, F) provide evidence of the accessibility of the surface-bound noble metal NPs for catalysis by revealing that the NPs decorate the surface of the polymer/ND composite. The SEI-S/TEM images offer depth of field at extremely high spatial resolution and show that the metal NPs are not embedded in the polymers, but instead are adhered to the surface of the polymer/ND composite particles.

High-resolution energy-dispersive spectroscopy (EDS) obtained with S/TEM provided chemical mapping of the polymer and Au, Pt, or Pd NPs attached to the polymer/ND surface. As evident from Figure 4.7, the polymer coating appears to cover the entire ND surface. The BF-S/TEM images in Figure 4.8 (A, D, and G) are clearly correlated to the maps of the characteristic sulfur-K X-rays at 2.3 keV shown in Figure 4.7 B, E, and H. One of the monomers in the polymer coating is PETMP, which is a tetra-thiol molecule, the only sulfur-containing molecule. Therefore, the sulfur EDS map indicates that the polymer coating is confined to the surface of the ND shown in the bright-field (BF)-S/TEM images. Figure 4.8 C, F, and I correspond to the Au-L, Pt-M, and Pd-L X-ray lines at 9.7, 2.0, and 2.8 keV, respectively. These EDS maps demonstrate that metal NPs are adhered to the surface of the thiol-ene polymer that coats the entire surface of the ND and follows the topography of the diamond surface with high fidelity. These maps complement the XPS data and show that the sulfur bonding environment corresponds to the local attachment of the metal NPs.

Finally, because the development of green catalysts is desirable, we studied the catalytic properties of NP/polymer/ND composite particles in an aqueous reaction of high significance. The catalytic efficiencies of the Au, Pt, and Pd NPs supported on the

polymer/ND particles were probed using the reduction of para-nitrophenol (PNP) to para-aminophenol (PAP) with $NaBH_4$, which is easily followed using UV-Vis absorbance measurements.[49] In addition to the convenient monitoring, this reaction is important because PAP is widely used as a precursor in the industrial synthesis of paracetamol (acetaminophen).[50] Nitrophenols have also been identified as priority pollutants, making their conversion to less toxic aminophenols a desirable environmental goal.[51-52] Without a catalyst, an aqueous mixture of PNP and $NaBH_4$ persists indefinitely as a clear, bright yellow solution with an absorbance at 400 nm. Upon the addition of the NP/polymer/NDs, the PNP absorption band at 400 nm gradually decreases, while a weaker absorption band at 300 nm, corresponding to the reduction product, 4-aminophenol, appears in the UV spectrum. The resulting solution is very basic (8<pH<14), creating a particularly challenging environment for the NP catalysts.

Instead of reporting TOFs, we quantify the catalytic activity in units of catalytic cycles per active site per second, a quantity known as the site time yield (STY),

$$STY = \frac{5n_p}{6D_M n_m t} \tag{4.2}$$

where n_p is the number of moles of product produced during the measurement time, D_M is the metal size dispersion, n_m is the total moles of metal atoms used, and t is the measurement time. The ratio of surface atoms to total atoms in a metal cluster is the metal size dispersion,

$$D_M = \frac{6n_s M_w}{\rho N d_p} \tag{4.3}$$

where n_s is equal to the number of metal atoms on the particle surface per unit area, M_w is

the molecular weight of the metal, ρ is the bulk metal density, N is Avagadro's number, and d_p is the diameter of the metal clusters as determined by TEM.[53-54] The STY calculation takes into consideration the surface area in addition to the total amount of metal to account for the surface specificity of most catalytic processes. In evaluating catalytic efficiencies using STYs, the importance of NP size is accounted for by using D_M. This size-related factor takes into account the fact that as the NP diameter decreases, the effective total surface area increases, leading to a greater number of defect sites important to catalysis. This factor has been evaluated by many others, and the reader is directed to the related publications for a more in-depth discussion.[55-57]

When used as the catalyst for the reduction of PNP, the STYs for Au, Pt, and Pd NPs immobilized on polymer/NDs were observed to be within a typical range of reported values for Au and Pd NPs, with AuNPs being less catalytically active than Pd (see Table 4.1).[58] However, the activity of our PtNPs is higher than expected relative to the Au and Pd NPs. It is possible that the attachment of the PtNPs to the polymer may influence the adsorption energy of PNP, leading to a more favorable reaction environment than that of unsupported PtNPs.[59] Comparison of the STYs of the Au, Pd, and Pt NPs on the composite supports observed in this work with those reported for other metal NP systems is very informative. Fenger and coworkers presented the catalytic efficiency data for unsupported CTAB-stabilized AuNPs.[20, 57, 60-62] The higher catalytic rates of Fenger's materials and other unsupported systems are expected because substrate access to active sites is unhindered, whereas supported NPs are much less accessible; however, while possessing these extremely high activities, unsupported NPs are highly susceptible to aggregation and subsequent loss of catalytic activity. As a comparison, STYs for PNP

reduction for catalyst NPs supported on SiO_2 and TiO_2 are presented in Table 4.1.[60, 63-64] In these examples, SiO_2-supported NPs exhibit higher rates of PNP conversion; however, these studies neglected to show, as we have, that SiO_2 readily dissolves in this high pH reaction solution. This instability of SiO_2-based supports is the most compelling reason not to use these materials for acidic/basic aqueous reactions. Although the polymer/ND composites presented in our study exhibit lower conversion rates, their stability surpasses that of SiO_2-based systems, as shown below.

The stability of the AuNP/polymer/ND particles in an aqueous environment of high pH, generated in the above reaction, was compared to two known supported catalysts: AuNPs on mercaptosilane-coated silica spheres and AuNPs on bare diamond.[12, 27, 30, 65] AuNP/polymer/NDs and AuNP/NDs were stored for one week in an aqueous solution saturated with 4-NP and $NaBH_4$ (with pH of ~14). In the case of the AuNP/mercaptosilane/SiO_2 materials, the particles were exposed for only one day to avoid complete dissolution. As seen in Figure 4.9, the AuNPs on silica spheres and bare ND formed large aggregates. As expected, the silica spheres also dissolved in the extremely basic solution. Although the AuNPs on the polymer/ND samples did begin to aggregate, the extent of the aggregation was significantly smaller than that for the AuNPs supported on silica particles or AuNPs on bare NDs. When stored dry at ambient conditions for >6 months, the AuNPs on bare diamond aggregated extensively, whereas the AuNP/polymer/NDs showed no noticeable aggregation.

The stability of the polymer/ND particles was also tested with a variety of polar and nonpolar organic solvents. The composites remained unchanged after rinsing with copious amounts of acetone, isopropanol, acetonitrile, hexanes, methylene chloride,

chloroform, and toluene. This is a critical advantage over polymer-only supports, such as polystyrene, which swell and dissolve in most organic solvents.[11, 66] Thus, NP-coated polymer/ND particles are significantly more robust than silica, diamond, or polymer particles alone.

Traditional methods for surface modification of diamond require the use of high temperatures and pressures and of potentially harmful chemicals.[35] Our method of coating nanodiamond with a polymer creates a surface with numerous postfunctionalization possibilities. The reactivity of the primary amine groups in the polymer was investigated by attaching fluorescent tags. The incorporation of primary amine groups was accomplished by doping the monomer mixtures—which contained the metal salts and were identical to the materials prepared to support the NP catalysts—with either AMPAA or AEMA, two methacrylate monomers containing primary amines. A detailed description of this incorporation is available in the Materials and Methods section. Using well-established methods, we treated polymer/NDs with dansyl chloride and rhodamine B, which react with primary amines to form covalent bonds, and measured the fluorescence of the resulting materials (Figure 4.10).[32-34] Fluorimetry data showed strong fluorescence of dansylated polymer/NDs at 500 nm with an excitation wavelength of 300 nm, indicating that dansyl chloride had indeed attached to the primary amines of the polymer coating. Separately, epifluorescence microscopy showed negligible background fluorescence for bare nanodiamond, while polymer/NDs exhibited strong fluorescence when treated with rhodamine B (Figure 4.10). Thus, both of these fluorescent tags were successfully attached to the AuNP/polymer/ND surface, confirming the presence, accessibility, and reactivity of the primary amine groups.

4.4 Conclusions

In summary, we described a method to prepare novel thiol-ene polymer-coated ND particles with reactive surfaces. The polymer/ND particles function as a support by immobilizing Au, Pt, and Pd nanoparticles that retain their catalytic activity. The polymer/ND particles offer a versatile surface with an inert core that will allow probing reaction environments that were previously inaccessible. The successful use of this support for Au, Pt, and Pd nanoparticles suggests that it may be suitable for other transition metal and alloy nanoclusters. In an effort to further increase the catalytic efficiency of polymer/ND-supported catalysts, we are working toward developing higher surface area ND supports. We also aim to characterize the catalytic microenvironment in these particles.

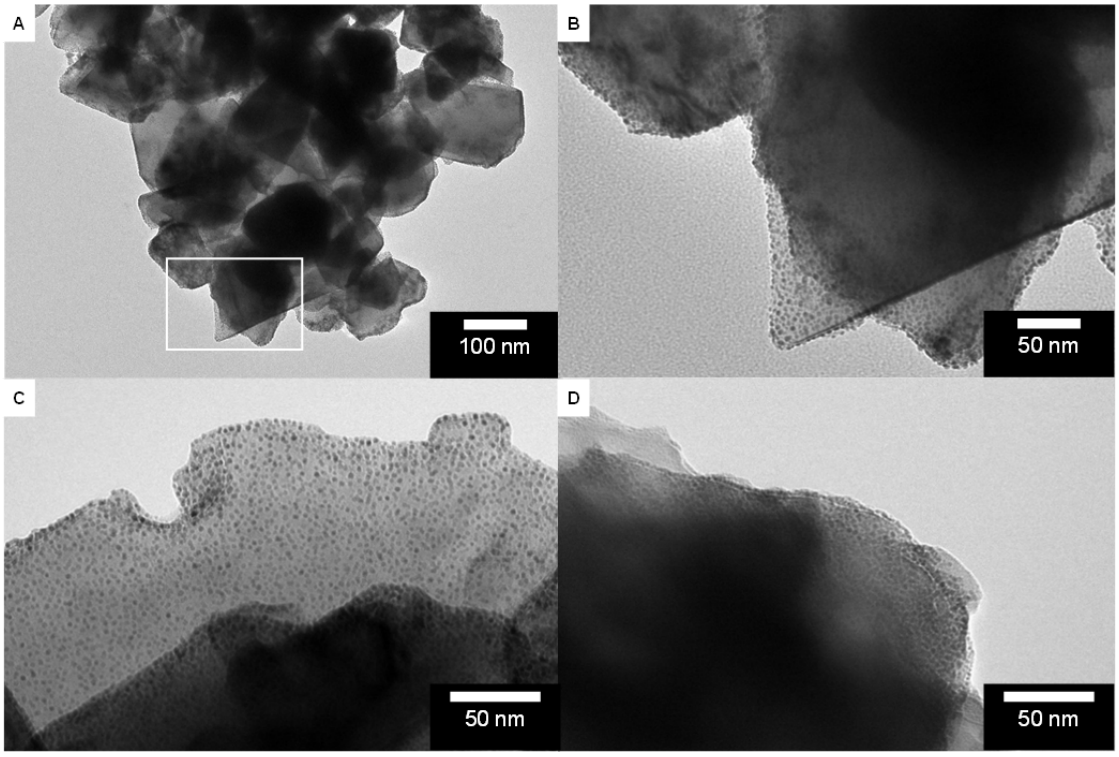

Figure 4.1 TEM images of polymer/diamond supports decorated with three different types of metal NPs.

Note. A = AuNPs/polymer/NDs; B = higher magnification of AuNPs/polymer/NDs; C = PtNP/polymer/NDs; D = PdNP/polymer/NDs.

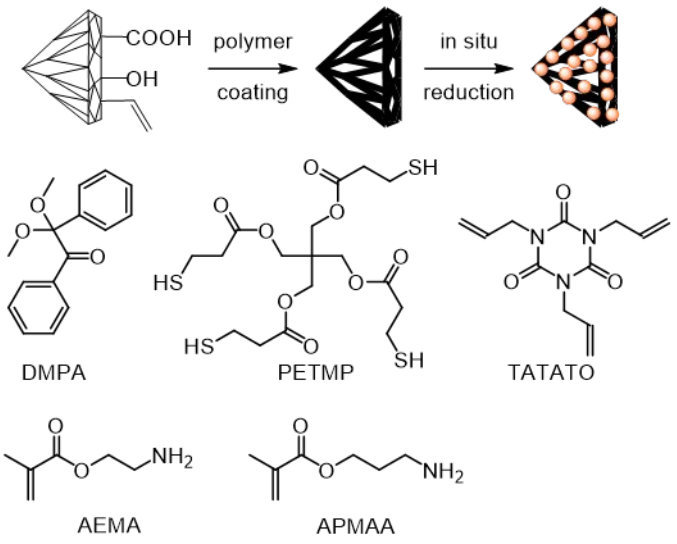

Figure 4.2 Photoinitiator and monomers used in polymer coating of NDs.

Note. The latter were then decorated with metal NPs via *in situ* reduction of metal salts.

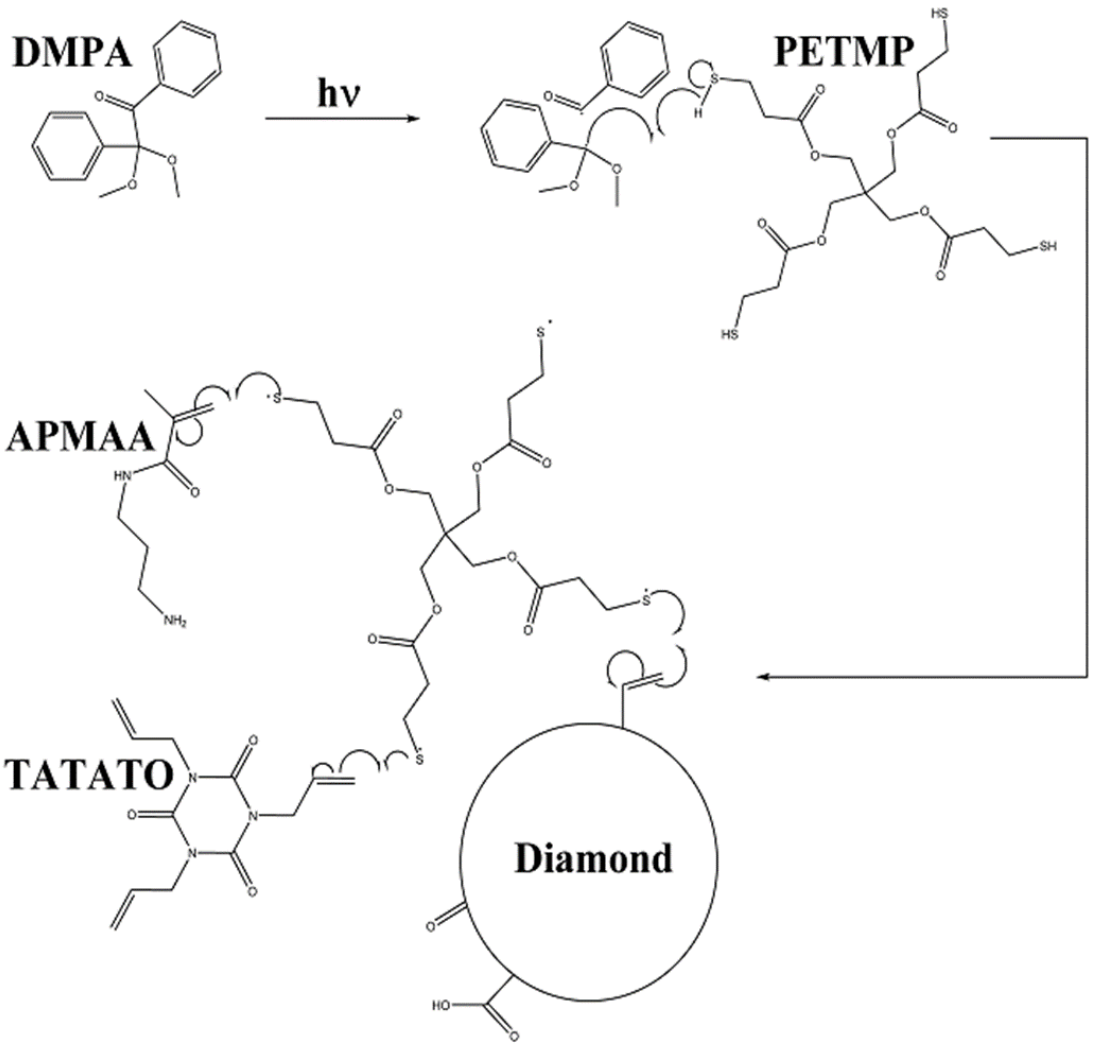

Figure 4.3 Reaction scheme: Proposed reaction pathway for photoinitiated radical polymerization and attachment of polymer onto diamond surface.

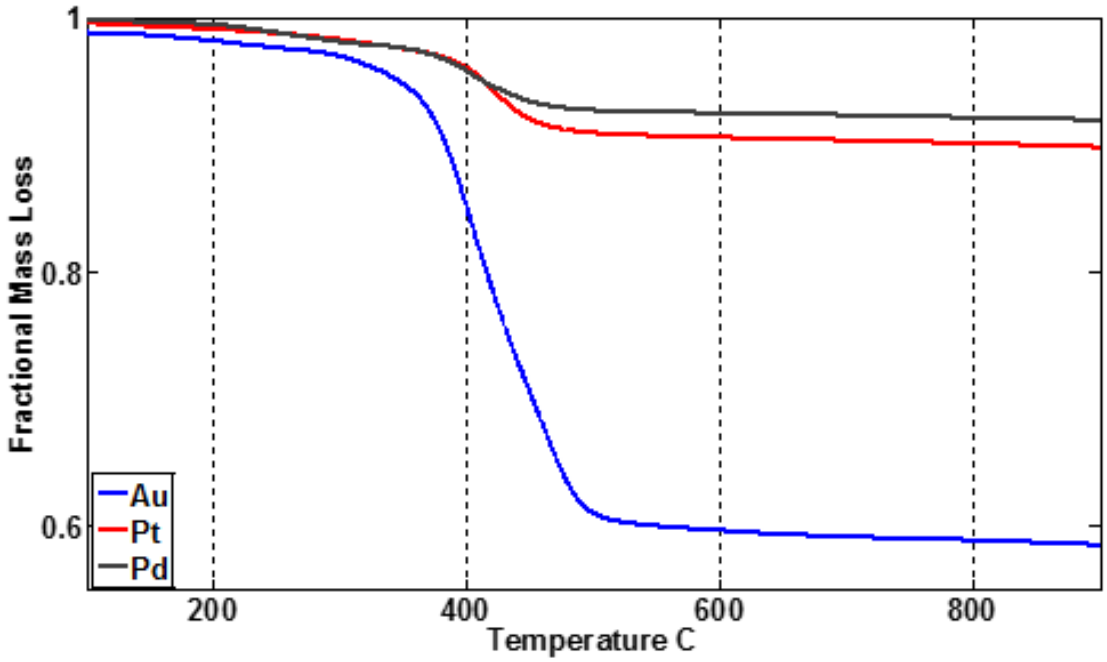

Figure 4.4 Thermogravimetric analysis (TGA) of the thiol-ene polymer/ND composites supporting either Au, Pt, or Pd NPs obtained to confirm the presence of the polymer.

Note. Mass loss curves show that the onset of polymer decomposition occurs at ~350 °C and continues until ~500 °C.

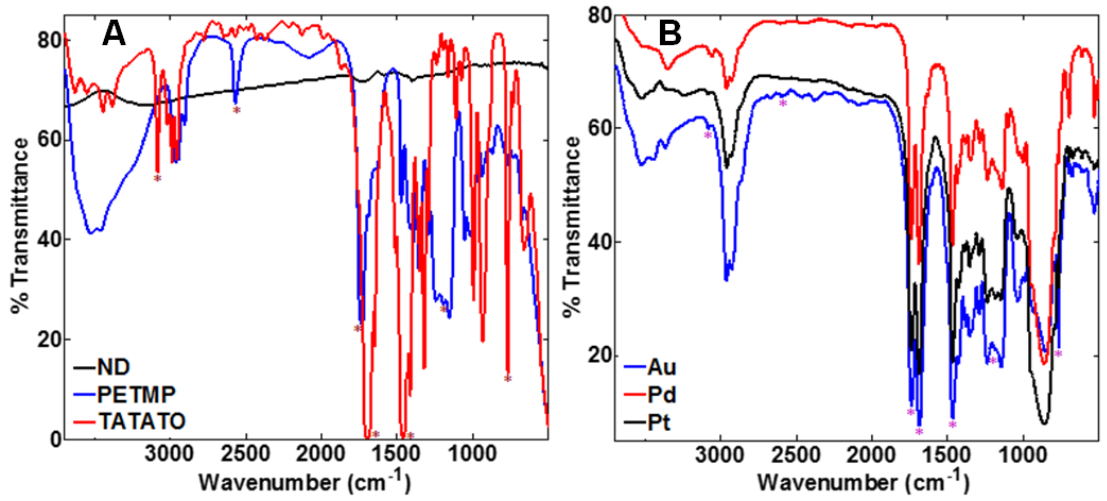

Figure 4.5 Vibrational spectra of (A) monomers (neat films on NaCl) and diamond (dried powder diluted with KBr) probed by DRIFTS, (B) DRIFTS spectra for polymer/NDs with imbedded Au, Pd, or Pt NPs.

Note. Asterisks in both panels indicate features similar between monomers and polymer/NDs.

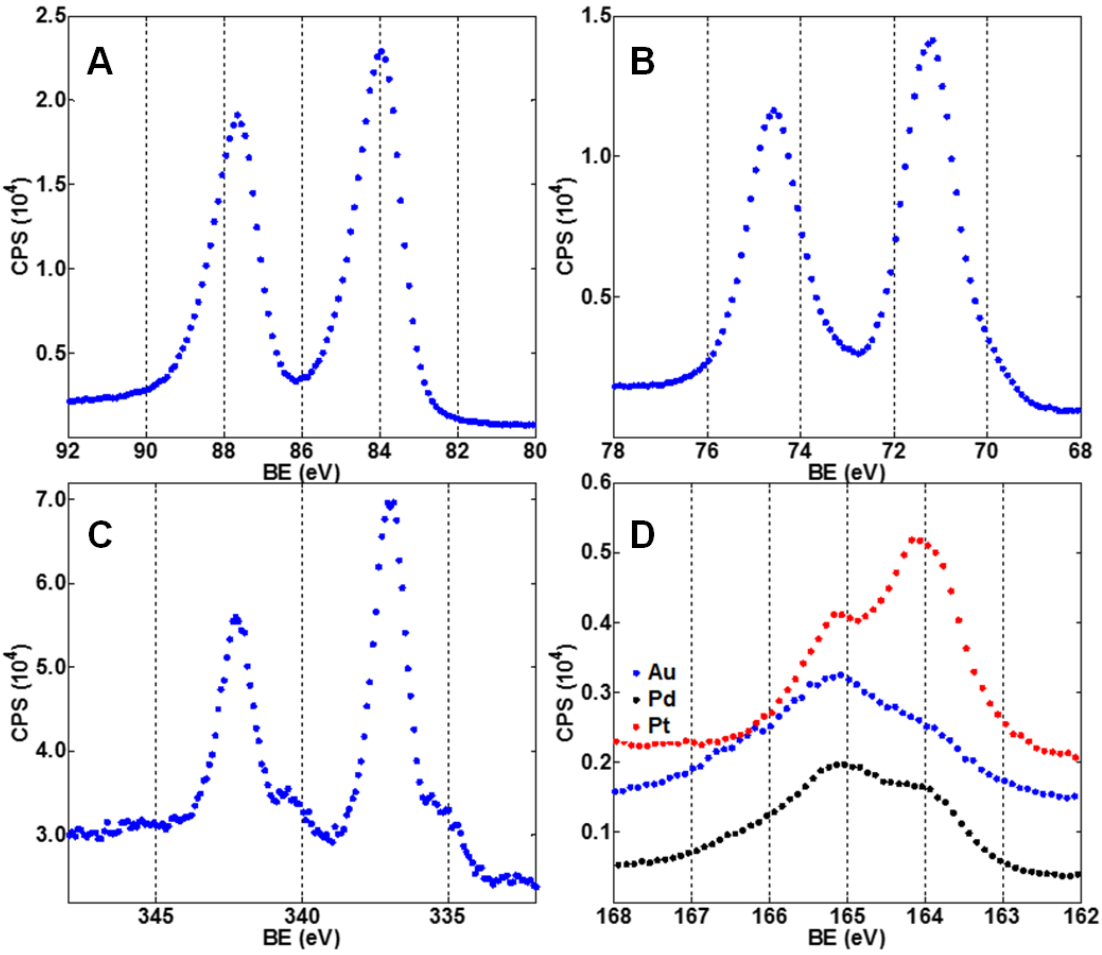

Figure 4.6 XPS spectra of polymer/ND materials.

Note. A = Au 4f region of AuNP/polymer/NDs; B = Pt 4f region of PtNP/polymer/NDs; C = Pd 3d region of PdNP/polymer/NDs; D = S 2p region for all three materials.

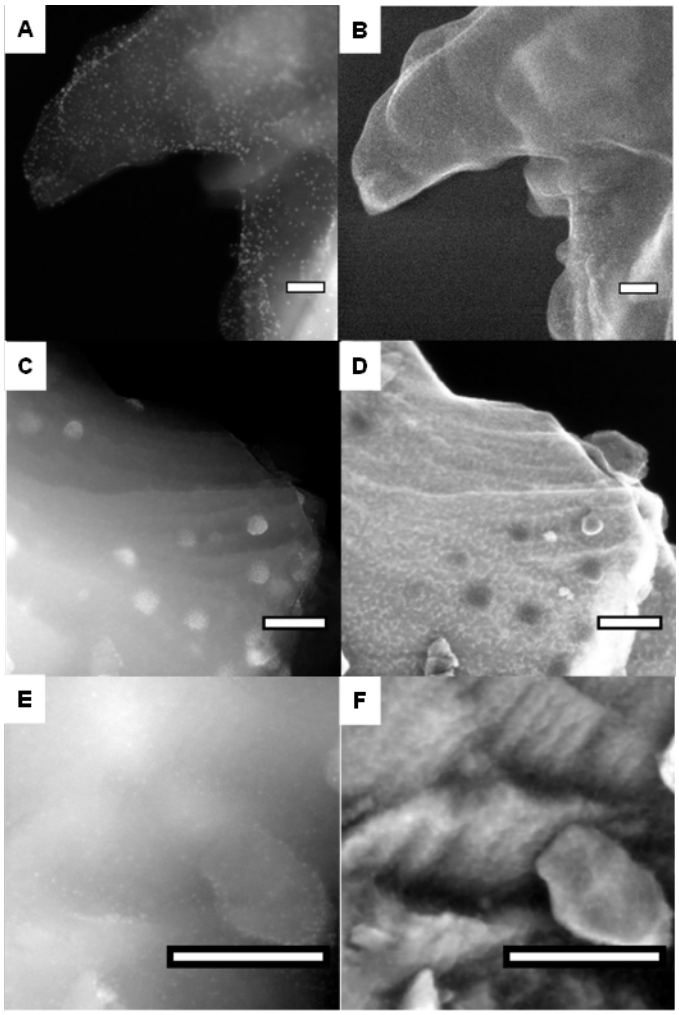

Figure 4.7 HAADF-S/TEM images of (A), (C), and (E) polymer/NDs decorated with Au, Pt, and Pd NPs, respectively.

Note. B, D, and F show SEI-S/TEM of the same region as the HAADF-S/TEM images for Au, Pt, and Pd, respectively. All scale bars are 50 nm.

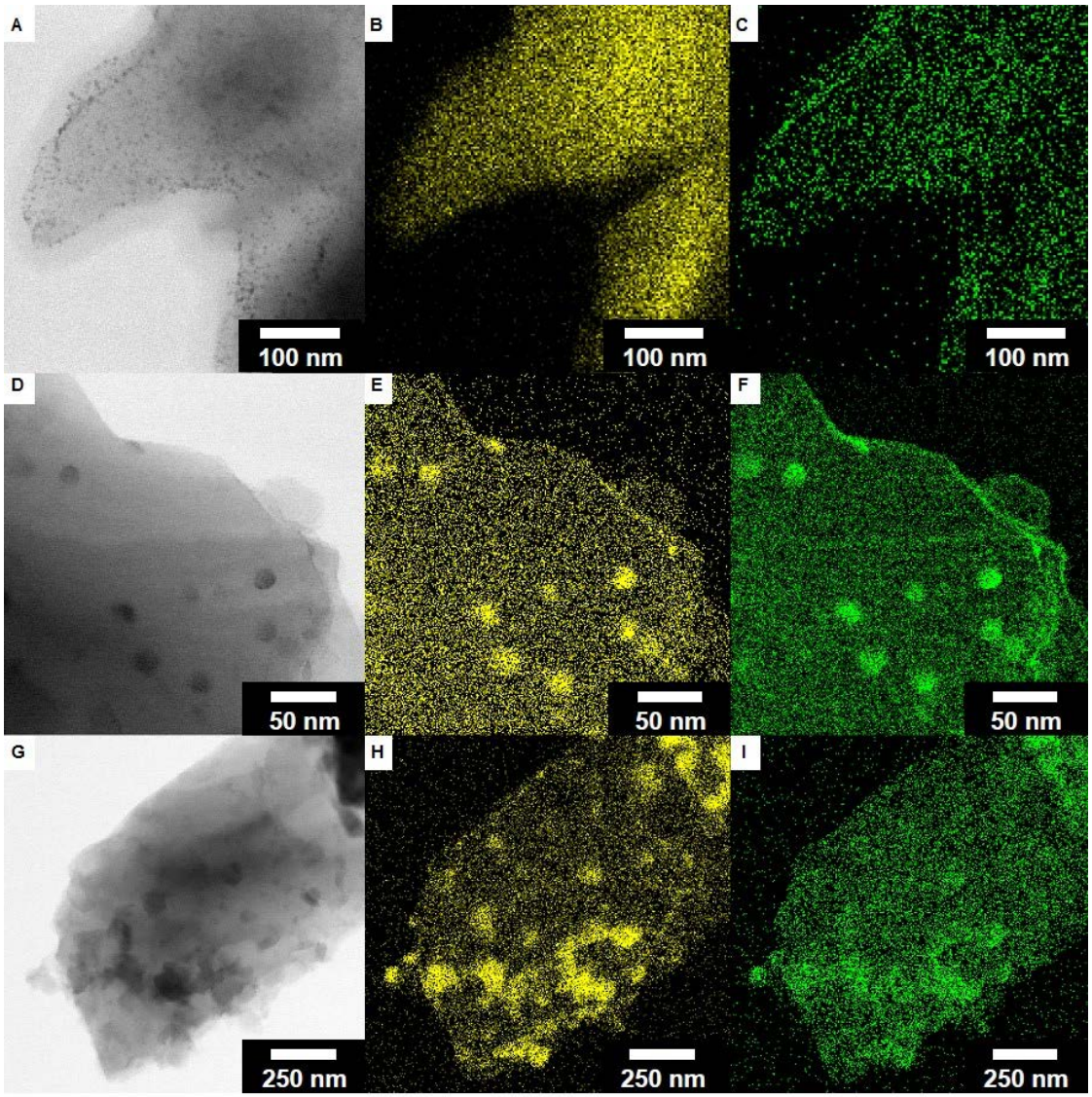

Figure 4.8 BF-S/TEM images of polymer/NDs decorated with (A) Au, (D) Pt, and (G) Pd.

Note. EDS images extracted from the sulfur K-line of the same polymer/NDs as seen in the BF-S/TEM images decorated with (B) Au, (E) Pt, and (H) Pd NPs, respectively. EDS images extracted from the (C) Au M-line, (F) Pt M-line, and (I) Pd L-line of NP-decorated polymer/NDs are of the same regions as seen in the BF-S/TEM and sulfur K-line EDS images.

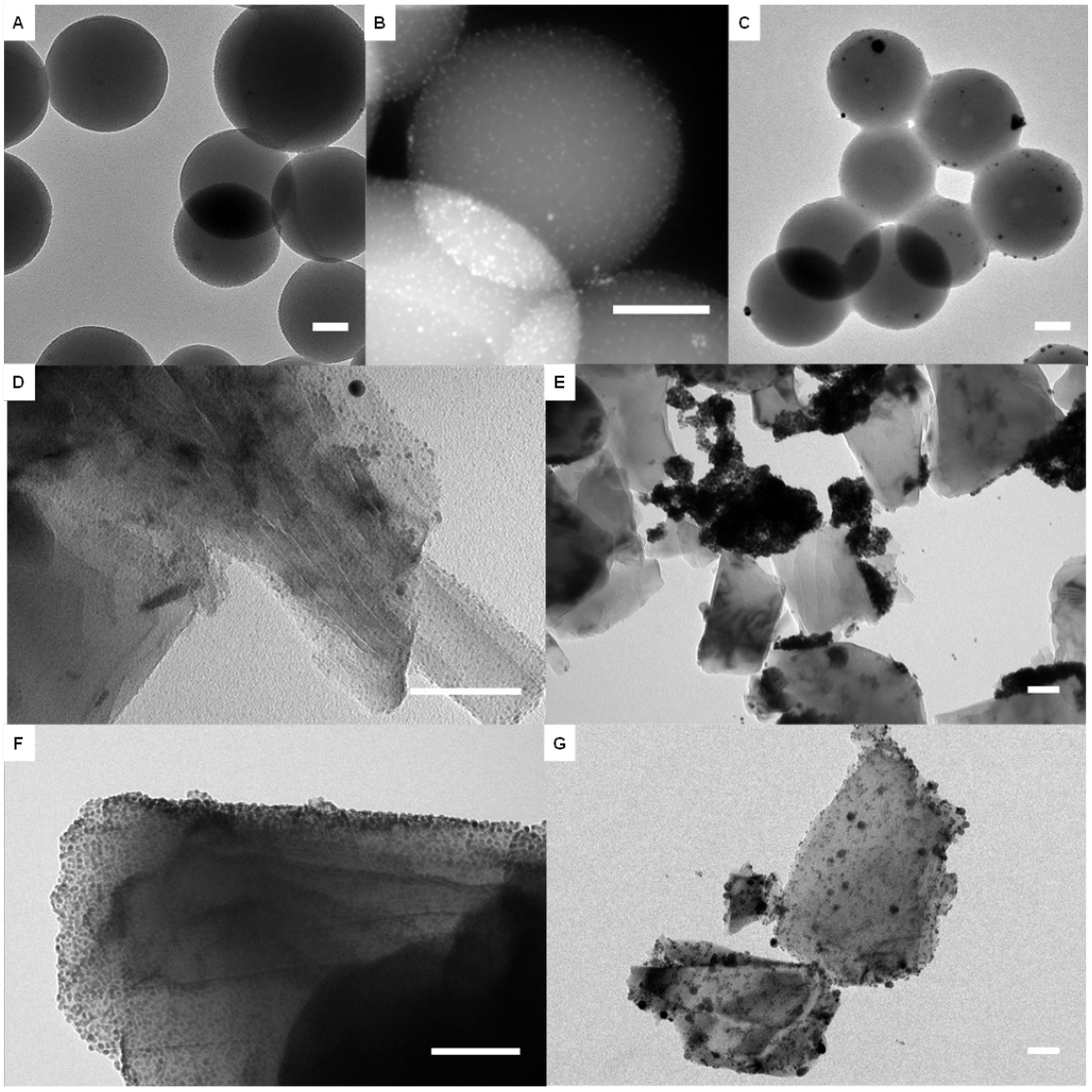

Figure 4.9 TEM images of silica- and diamond-supported AuNPs.

Note. (A) TEM image of AuNP decorated silica spheres with (B) a higher magnification HAADF-S/TEM image. (C) TEM image of the same silica spheres after one day of storage in solution saturated with PNP and $NaBH_4$ (pH of ~14). TEM images of bare ND decorated with AuNPs before (D) and after (E) one week of storage the saturated solution of PNP and $NaBH_4$. TEM images of AuNP/polymer/NDs before (F) and after (G) one week of storage in the saturated solution of PNP and $NaBH_4$. All scale bars are 50 nm.

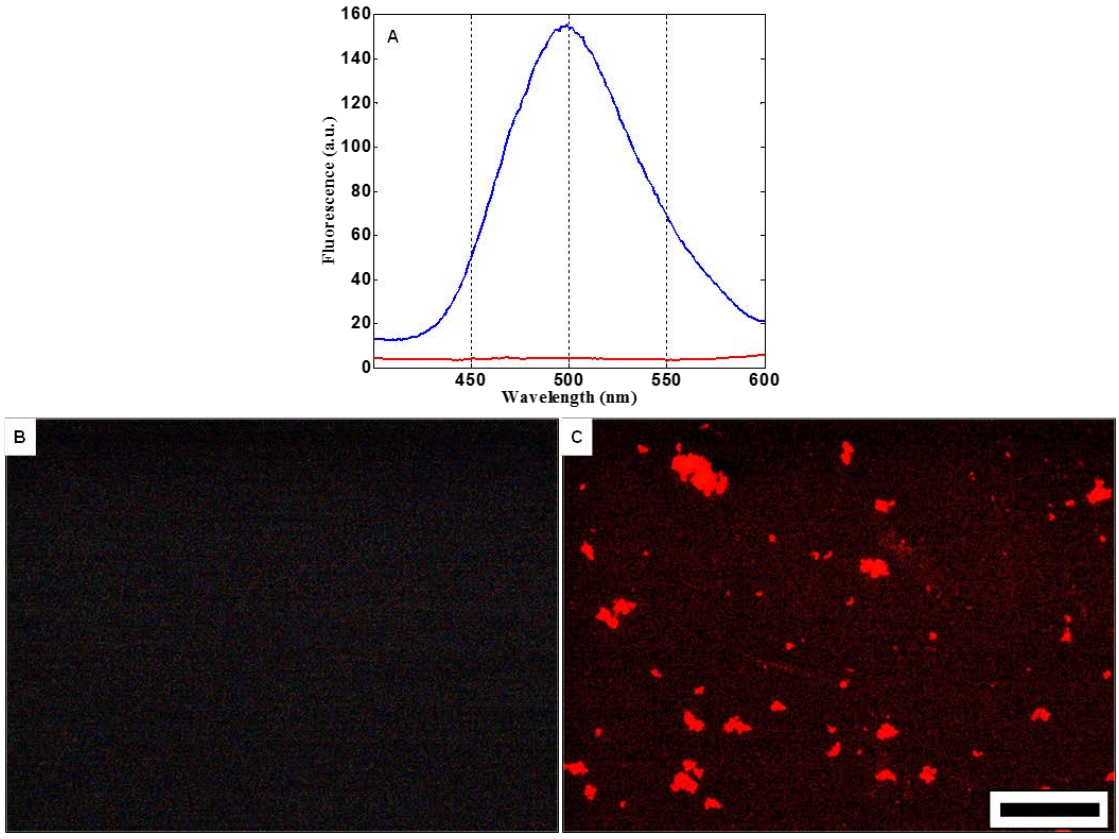

Figure 4.10 Fluorescence spectrum and epifluorescence microscopy images.

Note. (A) Fluorescence of bare ND (red) and after the treatment with dansyl chloride (blue). Epifluorescence microscopy images of (B) 1.0 µm bare diamond treated with rhodamine B and (C) polymer/ND composites treated with rhodamine B. Scale bar is 10 µm.

Table 4.1

Comparison of Catalytic Efficiencies of Current Work and Other Materials Prepared by Others

Metal NP/ Support	Rate Constant (s^{-1})[a]	STYs (s^{-1})[b]	T (K)	NP Size (mm)	PNP/$NaBH_4$/ metal NP (mol/mol/mol)	Reference
Polymer/ND	-	-	298	-	1/1000/-	This work
Au/polymer/ND	-	3.0 (± 1.0)x10^{-3}	298	4.5 ± 0.8	0.076/76/1	This work
Au/SiO_2[c]	3.24x10^{-1}	8	298	10	10/1000/1	El-Sheikh, 2013[62]
Au/TiO_2[d]	3.01x10^{-11}	4.0x10^{-2}	298	19	8/2814/1	Jin, 2012[63]
Pt/polymer/ND	-	2.1 (± 0.3)x10^{-2}	298	1.2 ± 0.3	1.49/1490/1	This work
Pt/SiO_2	1.40x10^{-1}	3	298	8	10/1000/1	El-Sheikh, 2013[62]
Pt/TiO_2[d]	1.79x10^{-11}	6.4x10^{-3}	298	5	8/2787/1	Jin, 2012[63]
Pd/polymer/ND	-	1.8 (± 0.4)x10^{-2}	298	1.5 ± 0.2	1.25/1250/1	This work
Pd/SiO_2	7.15x10^{-1}	37	298	20	10/1000/1	El-Sheikh, 2013[62]
Pd/TiO_2[d]	3.29x10^{-11}	6.4x10^{-3}	298	5	5/1520/1	Jin, 2012[63]

[a] Observed rate constant
[b] STY normalized using Equations 4.2 and 4.3
[c] SBA-15 mesoporous silica
[d] Reported TOF values used to calculate rate constant and STY

4.5 References

1. Cortie, M.; Van der Lingen, E. In *Catalytic Gold Nanoparticles*, *Mater. Forum*, 2002; pp 1-14.

2. Haruta, M.; Kobayashi, T.; Sano, H.; Yamada, N. Novel Gold Catalysts for the Oxidation of Carbon Monoxide at a Temperature Far Below 0 ^{o}C. *Chem. Lett.* **1987,** *16* (2), 405-408.

3. Corma, A.; Garcia, H. Supported Gold Nanoparticles as Catalysts for Organic Reactions. *Chem. Soc. Rev.* **2008,** *37* (9), 2096-2126.

4. Mikami, Y.; Dhakshinamoorthy, A.; Alvaro, M.; Garcia, H. Catalytic Activity of Unsupported Gold Nanoparticles. *Catal. Sci. Tech.* **2013,** *3* (1), 58-69.

5. Zhang, Y.; Cui, X.; Shi, F.; Deng, Y. Nano-Gold Catalysis in Fine Chemical Synthesis. *Chem. Rev.* **2011,** *112* (4), 2467-2505.

6. Thayer, A. M. The Catalysis Chronicles. *C&EN* **2013,** *91* (36), 64-68.

7. Vines, F.; Gomes, J. R. B.; Illas, F. Understanding the Reactivity of Metallic Nanoparticles: Beyond the Extended Surface Model for Catalysis. *Chem. Soc. Rev.* **2014,** *43* (14), 4922-4939.

8. Herves, P.; Perez-Lorenzo, M.; Liz-Marzan, L. M.; Dzubiella, J.; Lu, Y.; Ballauff, M. Catalysis by Metallic Nanoparticles in Aqueous Solution: Model Reactions. *Chem. Soc. Rev.* **2012,** *41* (17), 5577-5587.

9. Li, M.; Chen, G. Revisiting Catalytic Model Reaction *p*-Nitrophenol/$NaBH_4$ Using Metallic Nanoparticles Coated on Polymeric Spheres. *Nanoscale* **2013,** *5* (23), 11919-11927.

10. Gao, F.; Goodman, D. W. Model Catalysts: Simulating the Complexities of Heterogeneous Catalysts. *Annu. Rev. Phys. Chem.* **2012,** *63* (1), 265-286.

11. Wunder, S.; Polzer, F.; Lu, Y.; Mei, Y.; Ballauff, M. Kinetic Analysis of Catalytic Reduction of 4-Nitrophenol by Metallic Nanoparticles Immobilized in Spherical Polyelectrolyte Brushes. *J. Phys. Chem. C* **2010,** *114* (19), 8814-8820.

12. Wang, W.; Meng, Z.; Zhang, Q.; Jia, X.; Xi, K. Synthesis of Stable Au–SiO_2 Composite Nanospheres with Good Catalytic Activity and SERS Effect. *J. Colloid Interface Sci.* **2014,** *418* (0), 1-7.

13. Chen, J.; Xue, Z.; Feng, S.; Tu, B.; Zhao, D. Synthesis of Mesoporous Silica Hollow Nanospheres with Multiple Gold Cores and Catalytic Activity. *J. Colloid. Interface Sci.* **2014,** *429* (0), 62-67.

14. Zhou, J.; Ren, F.; Wu, W.; Zhang, S.; Xiao, X.; Xu, J.; Jiang, C. Controllable

Synthesis and Catalysis Application of Hierarchical PS/Au Core–Shell Nanocomposites. *J. Colloid. Interface Sci.* **2012,** *387* (1), 47-55.

15. Layek, K.; Kantam, M. L.; Shirai, M.; Nishio-Hamane, D.; Sasaki, T.; Maheswaran, H. Gold Nanoparticles Stabilized on Nanocrystalline Magnesium Oxide as an Active Catalyst for Reduction of Nitroarenes in Aqueous Medium at Room Temperature. *Green Chem.* **2012,** *14* (11), 3164-3174.

16. La-Torre-Riveros, L.; Guzman-Blas, R.; Méndez-Torres, A. E.; Prelas, M.; Tryk, D. A.; Cabrera, C. R. Diamond Nanoparticles as a Support for Pt and PtRu Catalysts for Direct Methanol Fuel Cells. *ACS Appl. Mater. Interfaces* **2012,** *4* (2), 1134-1147.

17. Antonels, N. C.; Meijboom, R. Preparation of Well-Defined Dendrimer Encapsulated Ruthenium Nanoparticles and their Evaluation in the Reduction of 4-Nitrophenol According to the Langmuir–Hinshelwood Approach. *Langmuir* **2013,** *29* (44), 13433-13442.

18. Biondi, I.; Laurenczy, G. B.; Dyson, P. J. Synthesis of Gold Nanoparticle Catalysts Based on a New Water-Soluble Ionic Polymer. *Inorg. Chem.* **2011,** *50* (17), 8038-8045.

19. Chen, J.; Xiao, P.; Gu, J.; Han, D.; Zhang, J.; Sun, A.; Wang, W.; Chen, T. A Smart Hybrid System of Au Nanoparticle Immobilized Pdmaema Brushes for Thermally Adjustable Catalysis. *Chem. Commun.* **2014,** *50* (10), 1212-1214.

20. Esumi, K.; Isono, R.; Yoshimura, T. Preparation of PAMAM− and PPI−Metal (Silver, Platinum, and Palladium) Nanocomposites and their Catalytic Activities for Reduction of 4-Nitrophenol. *Langmuir* **2003,** *20* (1), 237-243.

21. Huang, H.; Wang, X. Recent Progress on Carbon-Based Support Materials for Electrocatalysts of Direct Methanol Fuel Cells. *J. Mater. Chem. A* **2014,** *2* (18), 6266-6291.

22. Kim, J. H.; Boote, B. W.; Pham, J. A.; Hu, J.; Byun, H. Thermally Tunable Catalytic and Optical Properties of Gold-Hydrogel Nanocomposites. *Nanotechnology* **2012,** *23* (27), 275606.

23. Liu, Y.; Li, M.; Chen, G. A New Type of Raspberry-Like Polymer Composite Sub-Microspheres with Tunable Gold Nanoparticles Coverage and their Enhanced Catalytic Properties. *J. Mater. Chem. A* **2013,** *1* (3), 930-937.

24. Sainsbury, T.; Ikuno, T.; Okawa, D.; Pacilé, D.; Fréchet, J. M. J.; Zettl, A. Self-Assembly of Gold Nanoparticles at the Surface of Amine- and Thiol-Functionalized Boron Nitride Nanotubes. *J. Phys. Chem. C* **2007,** *111* (35), 12992-12999.

25. Shi, S.; Wang, Q.; Wang, T.; Ren, S.; Gao, Y.; Wang, N. Thermo-, pH-, and Light-Responsive Poly(*N*-isopropylacrylamide-co-methacrylic acid)–Au Hybrid Microgels Prepared by the *in Situ* Reduction Method Based on Au-Thiol Chemistry. *J. Phys.*

Chem. B **2014,** *118* (25), 7177-7186.

26. Stratakis, M.; Garcia, H. Catalysis by Supported Gold Nanoparticles: Beyond Aerobic Oxidative Processes. *Chem. Rev.* **2012,** *112* (8), 4469-4506.

27. Xie, W.; Walkenfort, B.; Schlücker, S. Label-Free SERS Monitoring of Chemical Reactions Catalyzed by Small Gold Nanoparticles Using 3D Plasmonic Superstructures. *J. Am. Chem. Soc.* **2012,** *135* (5), 1657-1660.

28. Saini, G.; Jensen, D. S.; Wiest, L. A.; Vail, M. A.; Dadson, A.; Lee, M. L.; Shutthanandan, V.; Linford, M. R. Core−Shell Diamond as a Support for Solid-Phase Extraction and High-Performance Liquid Chromatography. *Anal. Chem.* **2010,** *82* (11), 4448-4456.

29. Plettinck, S. C., L.; Wollast, R. Kinetics and Mechanisms of Dissolution of Silica at Room Temperature and Pressure. *Mineral Mag.* **1994,** *58A* (2), 728-729.

30. Stöber, W.; Fink, A.; Bohn, E. Controlled Growth of Monodisperse Silica Spheres in the Micron Size Range. *J. Colloid Interface Sci.* **1968,** *26* (1), 62-69.

31. Shem, P. M.; Sardar, R.; Shumaker-Parry, J. S. One-Step Synthesis of Phosphine-Stabilized Gold Nanoparticles Using the Mild Reducing Agent 9-BBN. *Langmuir* **2009,** *25* (23), 13279-13283.

32. Khabibullin, A.; Fullwood, E.; Kolbay, P.; Zharov, I. Reversible Assembly of Tunable Nanoporous Materials from “Hairy” Silica Nanoparticles. *ACS Appl. Mater. Interfaces* **2014,** *6* (19), 17306-17312.

33. Sardar, R.; Heap, T. B.; Shumaker-Parry, J. S. Versatile Solid Phase Synthesis of Gold Nanoparticle Dimers Using an Asymmetric Functionalization Approach. *J. Am. Chem. Soc.* **2007,** *129* (17), 5356-5357.

34. Bohaty, A. K.; Smith, J. J.; Zharov, I. Free-Standing Silica Colloidal Nanoporous Membranes. *Langmuir* **2009,** *25* (5), 3096-3101.

35. Mochalin, V. N.; Shenderova, O.; Ho, D.; Gogotsi, Y. The Properties and Applications of Nanodiamonds. *Na.t Nano.* **2012,** *7* (1), 11-23.

36. Szunerits, S.; Nebel, C. E.; Hamers, R. J. Surface Functionalization and Biological Applications of CVD Diamond. *MRS Bull.* **2014,** *39*.

37. Meziane, D.; Barras, A.; Kromka, A.; Houdkova, J.; Boukherroub, R.; Szunerits, S. Thiol-yne Reaction on Boron-Doped Diamond Electrodes: Application for the Electrochemical Detection of DNA–DNA Hybridization Events. *Anal. Chem.* **2012,** *84* (1), 194-200.

38. Mays, R. L.; Pourhossein, P.; Savithri, D.; Genzer, J.; Chiechi, R. C.; Dickey, M. D. Thiol-Containing Polymeric Embedding Materials for Nanoskiving. *J. Mater. Chem.*

C **2013,** *1* (1), 121-130.

39. Campos, M. A. C.; Paulusse, J. M. J.; Zuilhof, H. Functional Monolayers on Oxide-Free Silicon Surfaces *via* Thiol-ene Click Chemistry. *Chem. Commun.* **2010,** *46* (30), 5512-5514.

40. Wang, C.; Ren, P.-F.; Huang, X.-J.; Wu, J.; Xu, Z.-K. Surface Glycosylation of Polymer Membrane by Thiol-yne Click Chemistry for Affinity Adsorption of Lectin. *Chem. Commun.* **2011,** *47* (13), 3930-3932.

41. Lowe, A. B.; Hoyle, C. E.; Bowman, C. N. Thiol-yne Click Chemistry: A Powerful and Versatile Methodology for Materials Synthesis. *J. Mater. Chem.* **2010,** *20* (23), 4745-4750.

42. Hensarling, R. M.; Doughty, V. A.; Chan, J. W.; Patton, D. L. "Clicking" Polymer Brushes with Thiol-yne Chemistry: Indoors and Out. *J. Am. Chem. Soc.* **2009,** *131* (41), 14673-14675.

43. Silverstein, R. M.; Webster, F. X.; Kiemle, D.; Bryce, D. L. *Spectrometric Identification of Organic Compounds*. John Wiley & Sons: 2014; pp 118-125.

44. Pretsch, E.; Bühlmann, P.; Affolter, C.; Pretsch, E.; Bhuhlmann, P.; Affolter, C. *Structure Determination of Organic Compounds*. Springer: 2009; Vol. 13, pp 269-335.

45. Ton-That, C.; Shard, A. G.; Bradley, R. H. Thickness of Spin-Cast Polymer Thin Films Determined by Angle-Resolved XPS and AFM Tip-Scratch Methods. *Langmuir* **2000,** *16* (5), 2281-2284.

46. Gombac, V.; Montini, T.; Falqui, A.; Loche, D.; Prato, M.; Genovese, A.; Mercuri, M. L.; Serpe, A.; Fornasiero, P.; Deplano, P. From Trash to Resource: Recovered-Pd from Spent Three-Way Catalysts as a Precursor of an Effective Photo-Catalyst for H 2 Production. *Green Chem*. **2016**, *18* (9), 2745-2752..

47. Pennycook, S. J. Structure Determination through Z-Contrast Microscopy. In *Advances in Imaging and Electron Physics*. Peter W. Hawkes, P. G. M. G. C.; Marco, V.-A., Eds. Elsevier: 2002; Vol. Volume 123, pp 173-206.

48. Williams, D.; Carter, C. B. The Transmission Electron Microscope. In *Transmission Electron Microscopy*, Springer US: 2009; pp 3-22.

49. Pradhan, N.; Pal, A.; Pal, T. Silver Nanoparticle Catalyzed Reduction of Aromatic Nitro Compounds. *Colloids Surf. A* **2002,** *196* (2–3), 247-257.

50. Dathu Reddy, Y.; Venkata Ramana Reddy, C.; Dubey, P. K. Green Approach for Drug Design and Discovery of Paracetamol Analogues as Potential Analgesic and Antipyretic Agents. *Green Chem. Lett. Rev.* **2014,** *7* (1), 24-31.

51. Keith, L.; Telliard, W. ES&T Special Report: Priority Pollutants: Ia Perspective View. *Environ. Sci. Technol.* **1979,** *13* (4), 416-423.

52. Keith, L. H. The Source of U.S. EPA's Sixteen PAH Priority Pollutants. *Polycyclic Aromat. Compd.* **2015,** *35* (2-4), 147-160.

53. Boudart, M. Turnover Rates in Heterogeneous Catalysis. *Chem. Rev.* **1995,** *95* (3), 661-666.

54. Zhu, Q.-L.; Zhong, D.-C.; Demirci, U. B.; Xu, Q. Controlled Synthesis of Ultrafine Surfactant-Free NiPt Nanocatalysts toward Efficient and Complete Hydrogen Generation from Hydrazine Borane at Room Temperature. *ACS Catal.* **2014,** *4* (12), 4261-4268.

55. Laoufi, I.; Saint-Lager, M. C.; Lazzari, R.; Jupille, J.; Robach, O.; Garaudée, S.; Cabailh, G.; Dolle, P.; Cruguel, H.; Bailly, A. Size and Catalytic Activity of Supported Gold Nanoparticles: An in Operando Study during CO Oxidation. *J. Phys. Chem. C* **2011,** *115* (11), 4673-4679.

56. Zhou, X.; Xu, W.; Liu, G.; Panda, D.; Chen, P. Size-Dependent Catalytic Activity and Dynamics of Gold Nanoparticles at the Single-Molecule Level. *J. Am. Chem. Soc.* **2010,** *132* (1), 138-146.

57. Kuroda, K.; Ishida, T.; Haruta, M. Reduction of 4-Nitrophenol to 4-Aminophenol Over Au Nanoparticles Deposited on PMMA. *J. Mol. Catal. A: Chem.* **2009,** *298* (1–2), 7-11.

58. Gu, X.; Qi, W.; Xu, X.; Sun, Z.; Zhang, L.; Liu, W.; Pan, X.; Su, D. Covalently Functionalized Carbon Nanotube Supported Pd Nanoparticles for Catalytic Reduction of 4-Nitrophenol. *Nanoscale* **2014,** *6* (12), 6609-6616.

59. Pozun, Z. D.; Rodenbusch, S. E.; Keller, E.; Tran, K.; Tang, W.; Stevenson, K. J.; Henkelman, G. A Systematic Investigation of *p*-Nitrophenol Reduction by Bimetallic Dendrimer Encapsulated Nanoparticles. *J. Phys. Chem. C* **2013,** *117* (15), 7598-7604.

60. Damato, T. C.; de Oliveira, C. C. S.; Ando, R. A.; Camargo, P. H. C. A Facile Approach to TiO2 Colloidal Spheres Decorated with Au Nanoparticles Displaying Well-Defined Sizes and Uniform Dispersion. *Langmuir* **2013,** *29* (5), 1642-1649.

61. Fenger, R.; Fertitta, E.; Kirmse, H.; Thunemann, A. F.; Rademann, K. Size Dependent Catalysis with CTAB-Stabilized Gold Nanoparticles. *PCCP* **2012,** *14* (26), 9343-9349.

62. Que, Y.; Feng, C.; Zhang, S.; Huang, X. Stability and Catalytic Activity of PEG-b-PS-Capped Gold Nanoparticles: A Matter of PS Chain Length. *J. Phys. Chem. C* **2015,** *119* (4), 1960-1970.

63. El-Sheikh, S. M.; Ismail, A. A.; Al-Sharab, J. F. Catalytic Reduction of p-Nitrophenol

Over Precious Metals/Highly Ordered Mesoporous Silica. *New J. Chem.* **2013,** *37* (8), 2399-2407.

64. Jin, Z.; Xiao, M.; Bao, Z.; Wang, P.; Wang, J. A General Approach to Mesoporous Metal Oxide Microspheres Loaded with Noble Metal Nanoparticles. *Angew. Chem. Int. Ed.* **2012,** *51* (26), 6406-6410.

65. Gao, F.; Yang, N.; Smirnov, W.; Obloh, H.; Nebel, C. E. Size-Controllable and Homogeneous Platinum Nanoparticles on Diamond Using Wet Chemically Assisted Electrodeposition. *Electrochim. Acta* **2013,** *90* (0), 445-451.

66. Shang, K.; Geng, Y.; Xu, X.; Wang, C.; Lee, Y.-I.; Hao, J.; Liu, H.-G. Unique Self-Assembly Behavior of a Triblock Copolymer and Fabrication of Catalytically Active Gold Nanoparticle/Polymer Thin Films at the Liquid/Liquid Interface. *Mater. Chem. Phys.* **2014,** *146* (1–2), 88-98.

CHAPTER 5

CONCLUSIONS AND FUTURE WORK

5.1 Conclusions

Diamond-based support materials for catalysis have been developed, allowing for an alternative to silane/silica-based systems in heterogeneous catalysis. Synthetic diamond is resistant to acidic and caustic aqueous environments, as well as polar and nonpolar solvents, whereas other materials may exhibit significant degradation. While silane/silica-based materials were shown to be negatively impacted when used as the support material for AuNP catalysts, under the same conditions, diamond supports are unaffected. The stability of the C-C bonding in adhesion layers for diamond-supported systems is a key advantage over more labile bonds.

While synthetic diamond has many favorable properties as a catalyst support material, there are several different varieties: natural, CVD, DND, and HPHT. HPHT diamond was chosen for this work primarily because of its low cost, consistent surface properties, high surface area, and ease of particle separation. Initial work with HPHT diamond has revealed that metal impurities exist as inclusions throughout the crystalline matrix of these synthetic diamonds. Even with rigorous cleaning efforts in acid baths, these metal impurities persist as low-level contaminants at the HPHT diamond surface. These metal impurities have been exploited as heterogeneous catalysts for the reduction

of 4-NP by $NaBH_4$. Even at ppt concentrations, the surface metal impurities acted as catalysts, with HPHT ND materials exhibiting higher catalytic activity with higher ND surface areas.

Literature precedents for CVD and detonation diamond surface modifications offer a variety of surface chemistries for stable functionalization of sp^3 carbon atoms at the diamond surface. The success of many of these same functionalization routes has been evaluated for HPHT diamond, with encouraging results. Covalent attachment of hydrogen, nitrile, primary amine, and polymer brush groups has been demonstrated using several surface analysis techniques, including DRIFTS, XPS, TGA, zeta potential, and S/TEM.

Noble metal NP decoration of thiol-ene polymer layers on HPHT ND by photo-initiated radical polymerization has been shown to be an ideal platform for noble metal nanoparticle catalysts. The resulting material exhibits excellent adhesion for Au, Pt, and Pd NPs while still retaining catalytic activity and structural integrity in corrosive aqueous conditions. When compared with other materials discussed in the literature, these polymer/ND composites were observed to have higher substrate and adhesion-layer stability, leading to improved NP aggregation resistance.

5.2 Future Work

The work presented here was aimed at demonstrating a novel supported-catalyst system. Synthetic diamond, a crystalline lattice of sp^3 carbon, is shown to be a robust platform for investigating supported-catalytic systems. The next steps toward this goal are to expand upon diamond surface functionalization routes to allow anchoring of catalysts to these chemically stable systems and simultaneously use these surface

modifications to better understand the relationship between catalyst activity and the surrounding ligand/local environment. Other work might also include higher surface area materials such as detonation nanodiamond (DND) combining facile surface functionalization with a porous scaffold for attachment of catalytically active AuNPs.

5.2.1 Functionalization Routes

While the introduction of polymer/ND support systems for ultra-small AuNP catalysts is an important first step toward improved catalyst design, future modifications should allow more novel functionalization strategies to be developed. Figure 5.1 illustrates one example of a proposed reaction scheme for future development. Commonly, 2-2'Azobis(2-methylpropionitrile) (AIBN) is used as a free-radical initiator offering a source of tertiary carbon radicals with associated nitrile moieties. Bis(thiobenzoyl) disulfide can be homolytically cleaved through radical process involving AIBN.[1] These two reagents are commonly used in reversible addition fragmentation chain transfer (RAFT) polymerization, with thiobenzoate groups attaching as terminating groups. If a similar radical attachment process involving AIBN fragmentation to form N_2 and a tertiary nitrile radical propogation with the bis(thiobenzoyl) disulfide were possible, then ND termination with both nitriles and thiobenzoate groups might be a likely result. The ND powder could then be treated with the strong reducing agent, $LiAlH_4$, resulting in an ND surface decorated with primary amines and fully reduced thiol groups, conveying excellent properties to the ND surfaces of AuNP adhesion and primary amine functionality for further modification.

The nitrobenzene radical attachment to H-ND using a thermally initiated 4-nitrophenyldiazonium tetrafluoroborate salt has already been proven to be a successful

surface-modification route.[2-5] One currently unexplored approach with this material would be the catalytic reduction of these nitrobenzene groups by a mild reducing agent, $NaBH_4$, and AuNPs.[6] Figure 5.2 illustrates a proposed reaction scheme that would be an ideal application. Combining a nitroarene terminated surface with a known nitroarene reduction catalyst eliminates the need for other, more dangerous reduction routes of nitroarene groups involving $LiAlH_4$. If the catalytic reduction fails to reduce surface nitrile groups, then the use of AuNPs for the selective reduction of nitroarenes in the presence of nitrile groups would be an impactful discovery. If both nitroarenes and nitriles are catalytically reduced by AuNPs, the resulting aminated ND surface would still be highly useful as a potential substrate for applications demanding primary amines covalently bound to ND surfaces. One application for such an aminated surface would be for the growth of polymer brushes on ND powders: a material that could have uses as a chromatographic stationary phase or as a support material for embedded ultra-small catalysts.

5.2.2 Nanodiamond Supports and Polymer Brush Growth for Understanding Catalytic AuNP Microenvironments

Aminated ND has been shown to be a suitable material for ATRP polymer brush growth and, separately, it has been demonstrated that ND can be decorated with catalytically active AuNPs. The combination of polymer brush-coated ND with embedded catalytically active AuNPs would be a useful model system to study the influence of local environments on the catalytic efficiency of AuNPs. One might imagine that polymer brushes could be used to investigate how changing the hydrophobicity, aryl group density, the ionic environment, or another property surrounding catalysts might

also change substrate access to active sites, thereby influencing catalyst activity. Polymer brushes offer this potential because of the wide variety of methacrylate monomers available for radical mediated polymer brush coatings of surfaces. Figure 5.3 shows a few of these monomers that have been successfully used by Matyjaszewski and others to produce polymer brush coatings on aminosilane-modified silica surfaces; aminated ND surfaces are expected to allow similar surface modifications.[7-10]

5.2.3 Using Detonation Nanodiamond as a High-Porosity Scaffold

Detonation nanodiamond (DND) would also be an attractive synthetic diamond support because of the tendency of these ~5 nm primary particles to flocculate to larger 100s of nm agglomerates. TEM images of hydroxylated (unmodified) DND can be seen in Figure 5.4, revealing their high porosity. The surface of DND is readily modified with a number of functional groups such as amines and thiols, providing an ideal adhesion layer for the attachment of catalytically active ~5 nm AuNPs. Perhaps the similarity of pore and particle sizes between DND and ultra-small AuNPs would limit AuNP aggregation, prolonging catalyst lifetimes.

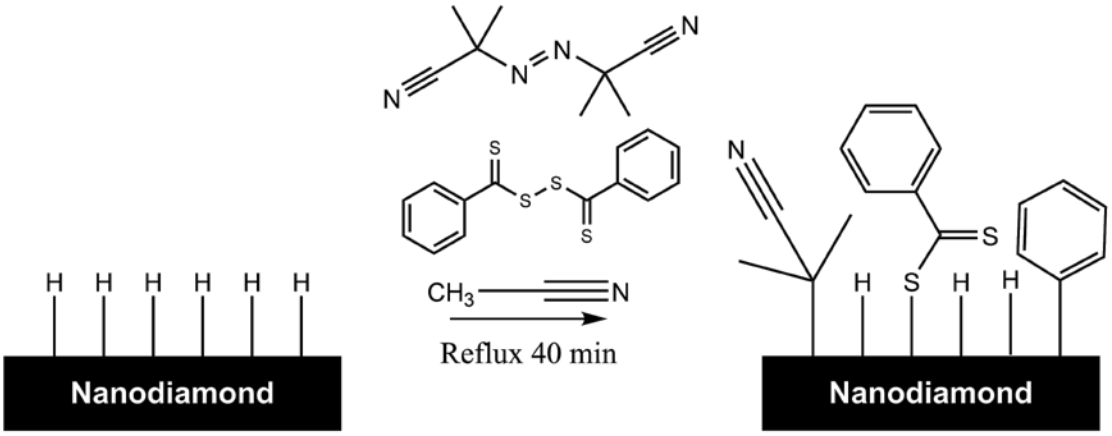

Figure 5.1 Proposed reaction scheme for the AIBN radical initiated attachment of tertiary nitriles and thiobenzoate groups to hydrogenated ND surfaces.

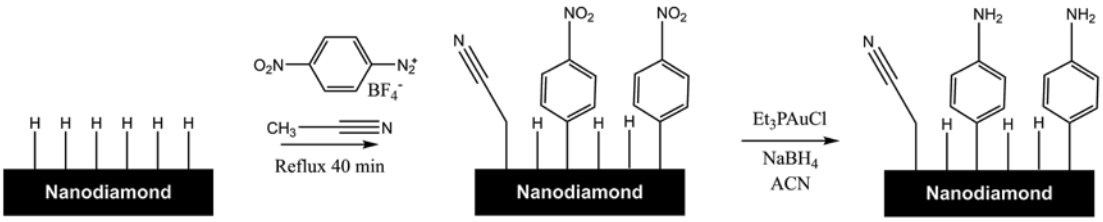

Figure 5.2 Proposed reaction scheme for nitroarene and nitrile attachment onto H-ND, followed by catalytic reduction of the nitroarene group using a gold salt and the mild reductant $NaBH_4$.

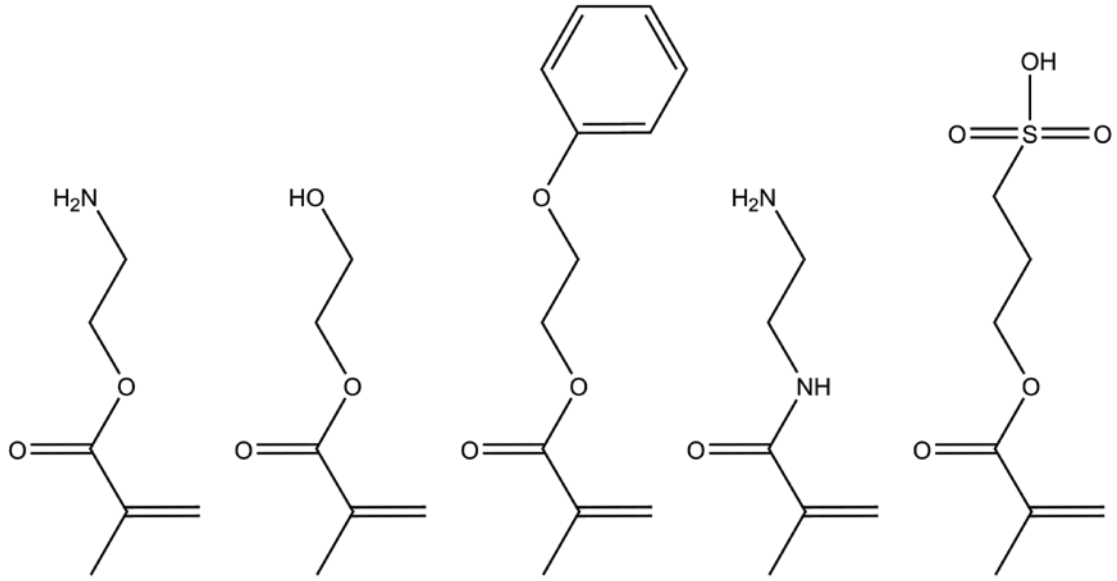

Figure 5.3 Example methacrylate monomer molecules used in polymer brush synthesis with various chemical moieties exhibiting differences in polarity, hydrophobicity, and ionic properties.

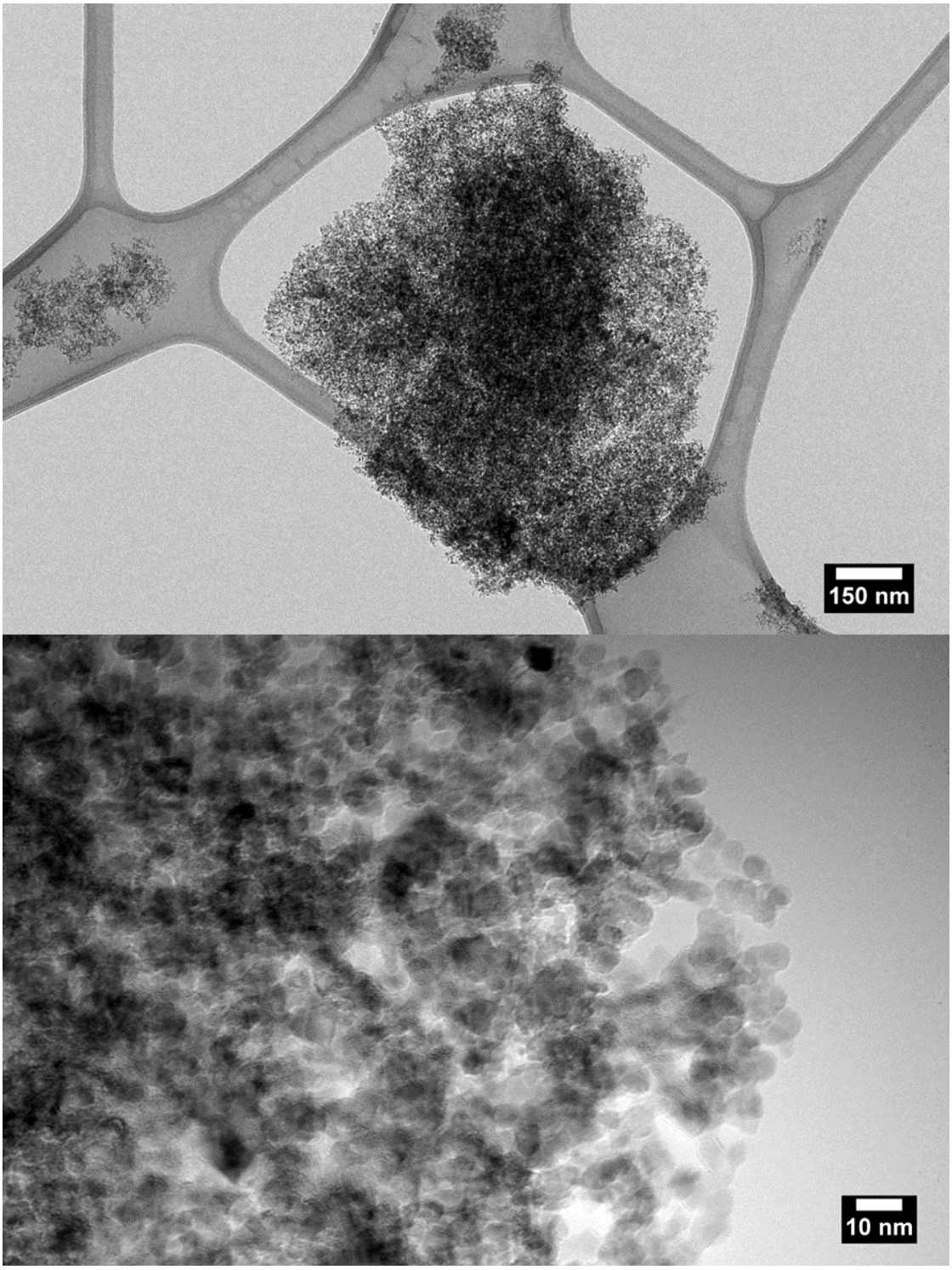

Figure 5.4 TEM images of hydroxylated DND agglomerates forming a highly porous network of ND particulates that could be used as a scaffold for ultra-small nanoparticles.

5.3 References

1. Wei, C.; Chen, M.; Tao, J.; Wu, X.; Khan, M.; Liu, D.; Huang, N.; Li, L. CdS Nanorods Assisted Thermal Oxidation of Polythiol Segments of PS-b-Polythiols to Produce Core Cross-Linking Micellar Clusters. *Polym. Chem.* **2014,** *5* (24), 7034-7041.

2. Corma, A.; Garcia, H. Supported Gold Nanoparticles as Catalysts for Organic Reactions. *Chem. Soc. Rev.* **2008,** *37* (9), 2096-2126.

3. Girard, H. A.; Petit, T.; Perruchas, S.; Gacoin, T.; Gesset, C.; Arnault, J. C.; Bergonzo, P. Surface Properties of Hydrogenated Nanodiamonds: A Chemical Investigation. *PCCP* **2011,** *13* (24), 11517-11523.

4. Girard, H. A.; Arnault, J. C.; Perruchas, S.; Saada, S.; Gacoin, T.; Boilot, J. P.; Bergonzo, P. Hydrogenation of Nanodiamonds Using MPCVD: A New Route Toward Organic Functionalization. *Diamond Relat. Mater.* **2010,** *19* (7–9), 1117-1123.

5. Corma, A.; Serna, P. Chemoselective Hydrogenation of Nitro Compounds with Supported Gold Catalysts. *Science* **2006,** *313* (5785), 332-334.

6. Zhang, Y.; Cui, X.; Shi, F.; Deng, Y. Nano-Gold Catalysis in Fine Chemical Synthesis. *Chem. Rev.* **2011,** *112* (4), 2467-2505.

7. Khabibullin, A.; Fullwood, E.; Kolbay, P.; Zharov, I. Reversible Assembly of Tunable Nanoporous Materials from “Hairy” Silica Nanoparticles. *ACS Appl. Mater. Interfaces* **2014,** *6* (19), 17306-17312.

8. Ji, W.; Panus, D.; Palumbo, R. N.; Tang, R.; Wang, C. Poly(2-Aminoethyl Methacrylate) with Well-Defined Chain Length for DNA Vaccine Delivery to Dendritic Cells. *Biomacromolecules* **2011,** *12* (12), 4373-4385.

9. Liu, G.; Shi, H.; Cui, Y.; Tong, J.; Zhao, Y.; Wang, D.; Cai, Y. Toward Rapid Aqueous RAFT Polymerization of Primary Amine Functional Monomer Under Visible Light Irradiation at 25 C. *Polym. Chem.* **2013,** *4* (4), 1176-1182.

10. Forster, D. J.; Heuts, J. P. A.; Davis, T. P. Conventional and Catalytic Chain Transfer in the Free-Radical Polymerization of 2-Phenoxyethyl Methacrylate. *Polymer* **2000,** *41* (4), 1385-1390.